

Tangential load and trim behaviour

Analysis of the Maeslant Barrier under seaward flow

J. van der Weijden



Mystery force and trim behaviour

Analysis of the Maeslant Barrier under seaward flow

by

J. van der Weijden

to obtain the degree of Master of Science
at the Delft University of Technology,
to be defended publicly on December 15, 2022.

Student number: 4696328
Project duration: March 1, 2022 – December 15, 2022
Thesis committee: Prof. dr. ir. S. N. Jonkman, TU Delft, supervisor
Dr. ir. P. van der Male, TU Delft
Dr. ir. A. M. R. Bakker, TU Delft/Rijkswaterstaat
Dr. ir. M. P. C. de Jong, Deltares
Ir. H. Nederend, Rijkswaterstaat

An electronic version of this thesis is available at <http://repository.tudelft.nl/>.
Front page image from Rijkswaterstaat, n.d.-d

Preface

This report contains the results of an investigation over the last eight months, which gave me the possibility to take a dive into a peculiar set of hydraulic phenomena. This possibility is in a large part thanks to Rijkswaterstaat, who facilitated this investigation. This investigation gave me a totally new insight in phenomena specific to the Maeslant barrier, which I hope to convey in this report.

I want to especially thank the members of my thesis committee, without whose experience and detailed feedback I could not have obtained the result presented here. For example, I especially believe that discussions in our meetings were integral to the structure of the final report. Furthermore, I want to thank everyone with, whom I have discussed parts of my thesis, for providing me with further feedback.

Lastly, I want to thank my family, without whose support over the last years, I would not have been able to get to this point.

*J. van der Weijden
Katwijk, December 2022*

Rapport samenvatting

De Maeslantkering is een stormvloedkering in de Nieuwe Waterweg die de omgeving van Rotterdam beschermt door middel van twee sectordeuren (Figure 1A). De Nieuwe Waterweg wordt in twee hoofdstappen afgesloten, eerst worden de drijvende sectordeuren de Nieuwe Waterweg ingedreven. Vervolgens, worden de twee deuren op de drempel van de kering afgezonken door de deuren met ballast water te vullen. Dit rapport beschouwt het gedrag van de kerende wanden van de twee sectordeuren (Retaining wall in Figure 1A) al drijvend in de Nieuwe Waterweg onder een stroom in de richting van zee. Al drijvend na een hoogwater piek zorgt het terugtrekkende getij doorgaans voor een zeewaartse stroming. Het gedrag beschouwd in dit rapport bestaat uit drie verschillende effecten:

- Een drukkracht in de verbinding tussen de sectordeur en geleide toren (in rood in Figure 1A), die de sectordeur richting het parkeerdok duwt, geduid als **mystery force**.
- Een quasi-constante verandering van de trimhoek (Figure 1B) van de kerende wanden, de relatieve verticale positie van de uiteinden van de kerende wand, geduid als **trimhoek effect**.
- Een periodische oscillatie van de trimhoek van de kerende wanden, in de literatuur van de kering bekend als het **mode 3 effect**. Dit effect gaat samen met een staande golf in de Nieuwe Waterweg die door de beweging van de kerende wanden opgeslingerd wordt.

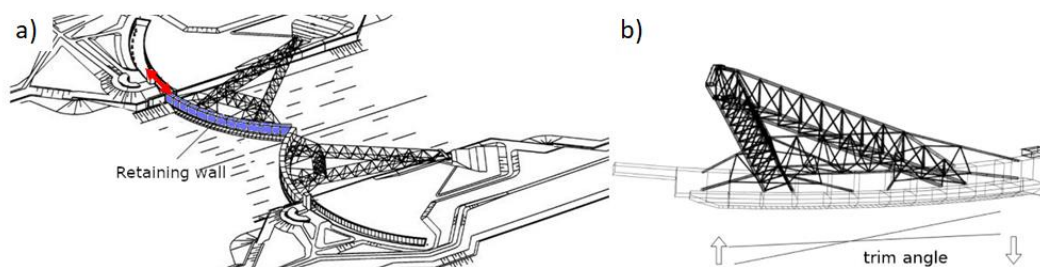


Figure 1: a) overzicht Maeslantkering met een van de kerende wanden (retaining wall) en de locatie van de mystery force gemarkeerd b) illustratie trimhoek (trim angle) vrijheidsgraad, afbeeldingen van Rijkswaterstaat, n.d.-a

De beschouwde effecten zijn geconstateerd tijdens functioneringssluitingen, echter zijn deze effecten nog onvoldoende fysisch verklaard, hierdoor kan ook de magnitude van deze effecten niet goed verklaard worden. De grootte van deze effecten in extreme situaties is onzeker. Het doel van dit rapport is om een inschatting te maken van deze effecten in een extreme situatie, en om hiermee vast te stellen of kritische grenzen van de kering overschreden worden.

Dit rapport toont aan dat er correlatie is tussen de drie beschouwde effecten, en dat de effecten in magnitude toenemen voor een toenemend zeewaartse afvoer bij de kering. De mystery force is passend gemodelleerd met een impulsbalans, en er zijn relevante statistische relaties gevonden. Extrapolaties voor een extreme lokale afvoer (kans in de orde 10^{-6} per jaar), leidt tot een verwachting van 2,300-5,400 kN (inclusief 90% onzekerheidsinterval). Dit is lager dan de sterkte van de verbinding die deze kracht overbrengt (6,000 kN).

Voor het trimhoek en mode 3 effect verklaren de conceptuele modellen niet de waarnemingen, echter zijn wel relevante statistische relaties gevonden. Het geëxtrapolerde trimhoek effect (7.5-13 milliradianen) is niet direct vergeleken met kritische grenzen ten aanzien van deze verplaatsing, omdat het effect gecompenseerd kan worden. Voor het mode 3 effect lijkt een statische model op een maximale waarde voor het effect te duiden, met een vergelijkbare amplitude als waargenomen tijdens functioneringssluitingen, dit geeft geen reden om overschrijden van kritische grenzen te verwachten. Deze maximale waarde is gebaseerd op beperkte data met een beperkte lokale afvoer, wanneer vergeleken met extreme situaties. Dit laatste maakt de geldigheid van het statistische model onzeker.

Dit rapport is gebaseerd op data verzameld tijdens functioneringssluitingen in de periode van 2007 tot 2021. De drie effecten en hydraulische condities zijn op basis van deze data gekwantificeerd. Op basis van deze kwantificatie zijn statistische modellen afgeleid. Ook, zijn conceptuele modellen beschreven, die de effecten fysisch trachten te verklaren. De hydraulische condities zijn gebruikt als input voor deze modellen en de uitkomsten vergeleken met de gekwantificeerde effecten. Als laatste, zijn de relevantste statistische en conceptuele modellen naar extreme condities geëxtrapoleerd, op basis van schattingen voor de extreme lokale afvoer.

Het trimhoek effect is gemodelleerd als functie van de mystery force, die als moment op de kerende wand werkt. Dit moment wordt gecompenseerd door hydrostatische drukken die ontstaan door een verandering van de trimhoek van de kerende wand. Dit model leidt tot een significante onderschatting van dit effect. Een ongelijk verdeelde zuigkracht onder de kerende wand is mogelijk een extra belasting die voor verandering van de trimhoek zorgt. De stijfheid van de kerende wand is afhankelijk van het waterdoorsnijdende breedte van de kerende wand, bij een groot lokaal verval kan deze breedte afnemen (zie Figure 2). Het kan onderzocht worden of dit al bij de situatie als waargenomen bij de functioneringssluitingen een rol speelt, of dat dit bij extreme situaties van belang is.

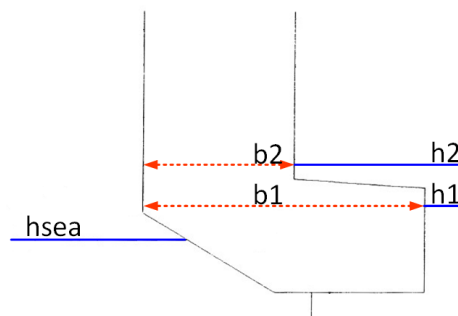


Figure 2: Illustratie van de verandering van breedte b door een verandering van de bovenstroomse waterstand, kopie van Figure 7.3

Het mode 3 effect is gemodelleerd als een systeem met de kerende wand als trimmend schip en met de benedenstroomse waterstand die hierdoor beïnvloedt wordt. Dit mode 3 model geeft een grenswaarde voor het verval over de kering waarboven de mode 3 trilling verwacht wordt. In werkelijkheid lijkt het mode 3 effect voor een veel kleiner verval op te treden dan verwacht aan de hand van dit model. Verder geeft dit model alleen een voorwaarde waarvoor het optreden van het effect verwacht wordt, factoren die de grootte van dit effect beperken zijn niet gemodelleerd, waardoor het model oneindige groei verwacht, dit strookt niet met waarnemingen en verwachtingen. Voor een verder verbeterd model voor het mode 3 effect, kunnen de traagheid van de stroom onder de kerende wand en het effect van de golf die wegloopt van de kering beschouwd worden.

In dit rapport wordt gesuggereerd om het verval dicht bij de kering te meten, op dit moment worden waarnemingen op een relatief grote afstand gedaan. Dit kan inzicht verschaffen op het kritische verval waarboven het mode 3 gedrag zich voordoet, maar ook in de validiteit van de schematisering die gebruikt is voor het mystery force model. Wat betreft het trimhoek effect, kan worden bepaald onder welke omstandigheden het nodig is dit effect te compenseren. Als laatste, kunnen de uitkomsten van het mystery force model gecombineerd worden met overige belastingen (korte golven, windbelasting) om de invloed van deze belasting op de faalkans van de kering te bepalen.

Report summary

The Maeslant barrier is a storm surge barrier that protects the Rotterdam area from extreme storm surges using two sector gates which close off the Nieuwe Waterweg. The Nieuwe Waterweg is one of the main waterways of the Rotterdam port area (Figure 3A). The waterway is closed in two main steps, first by moving the floating sector gates into the waterway. Second, the sector gates are filled with ballast water, such that they sink onto the sill of the barrier, closing off the waterway. This report considers behaviour of the retaining walls (marked in Figure 3A) while floating and while flow in the waterway is in seaward direction. Such a situation occurs after a high water peak, and is induced by the receding tide. The behaviour considered in this report consists of three separate effects:

- A compressive force in the connection between the gate and the guiding tower (indicated in red in Figure 3A), which pushes the retaining wall towards the parking docks, referred to as the **mystery force**.
- A quasi-constant change of the trim angle, which indicates a difference in vertical position between the two ends of the retaining wall (indicated in Figure 3B), referred to as the **trim angle effect**.
- A periodic oscillation of the retaining wall trim angle, in existing literature referred to as the **mode 3 effect**. This oscillation is associated with a standing wave in the waterway, which is amplified by the retaining wall movement.

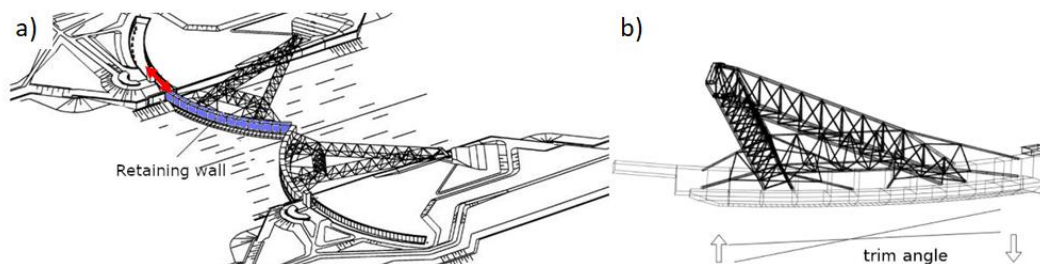


Figure 3: a) overview of the Maeslant barrier with one of the retaining walls and location of the mystery force highlighted b) illustration of the trim angle degree of freedom, image from Rijkswaterstaat, n.d.-a

The considered effects have been observed during test closures, however a satisfactory physical interpretation of the effects and the corresponding magnitude is missing. Because of this, the magnitude of the effects in extreme situations is unclear. The goal of this report is to assess whether, in extreme situations, the magnitude of the considered effects may exceed the design limits of the barrier.

This study establishes that the three effects correlate, and that the three effects increase in magnitude for an increasing seaward discharge at the barrier. The mystery is appropriately modelled with a momentum balance, and relevant statistical relations are found. Extrapolation to an extreme local discharge (probability in the order of 10^{-6} per year) leads to values of 2,300-5,400 kN (including 90% confidence interval). This is below the design strength of the connection that transfers this load (6,000 kN).

For the trim angle effect and the mode 3 behaviour the conceptual models do not explain the observations, relevant statistical relations have however been found. The extrapolated trim effect, 7.5-13 milliradians, is not directly related to design limits of the barrier, as it may be compensated for during operation. For the mode 3 effect a statistical model suggests that the amplitude under high discharges plateaus to values similar as observed during test closures, consequently this effect is not expected to exceed design limits. The statistical relation for the mode 3 effect is based on a set of data, with entries with only a limited local discharge compared to extreme situations. This makes the validity of the statistical model with such a plateau uncertain.

This report is based on data of test closures that took place in the period from 2007 to 2021. The three effects and hydraulic conditions are quantified based on these data. From these quantified numbers, statistical models are derived. Furthermore, conceptual models which attempt to give a physical description of the observed effects are derived, these models are combined with the observed hydraulic conditions, and results are compared against the observed effects. Lastly, the statistical and conceptual models that appear to be the most relevant are extrapolated to extreme conditions, based on estimations of the extreme seaward discharge at the barrier.

The trim effect is modelled as a function of the mystery force, which acts as a moment on the retaining wall, this moment is balanced by hydrostatic pressures that follow from the changed trim angle. This model significantly underestimates the observed magnitude. Loading due to a varying suction force along the bottom of the retaining wall may play a role, as another load changing the retaining wall trim angle. Furthermore, the stiffness of the retaining wall depends on the effective width of the retaining wall, which may be reduced under a high head difference (see Figure 4). It may be explored whether this plays a role for the observed effect during test closures, or whether it plays a role in more extreme conditions.

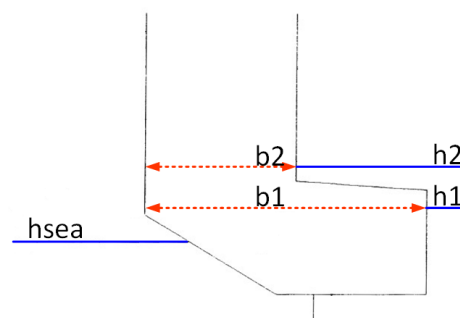


Figure 4: Illustration of change of width b due to a change of the upstream water level, copy of Figure 7.3

The mode 3 conceptual model consists of an analogy of the retaining wall with a pitching ship and a description of changes of the water level downstream of the barrier due to the pitching retaining wall. The conceptual model provides a threshold for the local head difference, above which the mode 3 effect occurs. In observations, however, the mode 3 effect occurs for a much smaller head difference than follows from the conceptual model. Furthermore, the mode 3 model describes the effect as an infinitely growing phenomenon, effects that limit the effect are not modelled. For an improved mode 3 model, the inertia of the flow under the retaining wall and the translatory effect of the wave in the waterway may be considered.

In this report it is suggested to observe the head difference over the barrier more locally, at present observations are done relatively far away. This may give further insight in the onset of the mode 3 effect, and applicability of the schematization used in the mystery force model. Regarding the trim effect, it may be assessed when it may need to be compensated with ballast water. Lastly, the model outcomes for the mystery force may be combined with other loads (short period waves, wind loads) to assess the impact of the combined load on the barrier failure probability.

Contents

Preface	i
Rapport samenvatting	ii
Report summary	iv
1 Introduction	1
1.1 Context	1
1.2 Objective	2
1.3 Report structure	3
2 Maeslant barrier behaviour	4
2.1 Maeslant barrier description	4
2.2 Retaining wall modes.	6
2.3 Mystery force	10
2.4 Trim angle effect	11
2.5 Mode 3 effect	11
2.6 Summary	12
3 Data acquisition	13
3.1 Data selection	13
3.2 Data collection	15
3.3 Data processing	17
3.4 Data description	18
3.5 Quantification of effects	20
3.6 Data visualisation.	22
3.7 Data quantification	24
3.8 Summary	25
4 Data analysis	27
4.1 Correlation between effects	27
4.2 Load correlation	30
4.3 Correlation matrix.	32
4.4 River level change regression	33
4.5 Empirical models	36
4.6 Summary	38
5 Conceptual models	40
5.1 Behaviour description	40
5.2 Mystery force	42
5.3 Trim angle effect	45
5.4 Mode 3 effect	46
6 Results and predictions	56
6.1 Conceptual models	56
6.2 Statistical models.	69
6.3 Extreme conditions	70
6.4 Summary	75
7 Discussion	77
7.1 Data	77
7.2 Models	78

8	Conclusions and recommendations	84
8.1	Conclusions	84
8.2	Recommendations	85
	Bibliography	88
	List of Figures	89
	List of Tables	93
	List of Symbols	94
A	Trim angle data description	96
B	Power spectrum analysis	97
B.1	The Wavelet transform	97
B.2	2D wavelet power spectrum	97
B.3	Scale-averaged wavelet power	98
C	Effects quantified characteristics	99
D	Dynamic effect and hydraulic conditions overviews	102
E	Correlation Matrix	116
F	Empirical model parameters	117
F.1	Mystery Force	117
F.2	Trim effect.	117
F.3	Mode 3 effect	118
G	Mystery force inertia effects	119
H	Mystery force model definitions	121
H.1	Local head difference	121
H.2	(B1) Hydrostatic approach	121
H.3	(B2) Momentum balance approach	123
H.4	(C1) Cross-sectional water level variation.	127
H.5	(C2) Suction force tangential contribution	127
I	Constant trim response model	129
I.1	Equation form.	129
I.2	Spring stiffness	129
I.3	Tangential force induced moment	130
J	Mode 3 model	132
J.1	Retaining wall inertia	132
J.2	Retaining wall added mass	132
J.3	Retaining wall damping	133
K	Mode 3 model solution	134
L	Jackknife resample	136

Introduction

1.1. Context

The Maeslant barrier is a storm surge barrier near Rotterdam that employs two sector gates. During extreme storm surges these gates close-off the waterway to protect low-lying parts of the Netherlands against flooding (see Figure 1.1a). The barrier works in tandem with the Hartel barrier, the locations of the two barriers in relation to Rotterdam are shown in Figure 1.1b.



(a) Closed Maeslant barrier, image from Rijkswaterstaat, 2007



(b) Maeslant barrier location, background image from Google Earth, 2022

Figure 1.1: Maeslant barrier introduction

When not in operation, the gates reside in the parking docks on the river banks. During operation, the floating gates are moved horizontally into the waterway. Next, the gates are ballasted with water to sink the gates onto the sill. At this point, the barrier protects the hinterland from high water. After the high tide passes the ballast water is removed, consequently the gates float up. Last, the floating gates are returned to the parking docks.

From this description, it can be seen that the gates are able to rotate horizontally and vertically. The vertical movement is controlled using ballast water. A tangential connection is present to control and restrict the horizontal movement of the gates. Furthermore, a third degree of freedom exists, the gates can rotate such that they are closer to the bottom of the waterway in the middle of the canal than at the banks. This degree of freedom is referred to as the *trim* or *pitch angle* (Figure 1.2B).

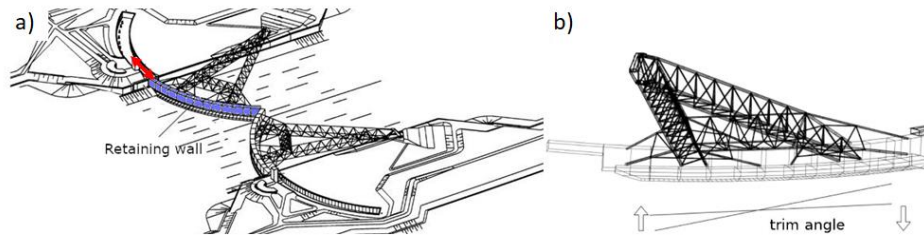


Figure 1.2: a) overview of the Maeslant barrier with one of the retaining walls and location of the mystery force highlighted b) illustration of the trim angle degree of freedom

This report considers the behaviour that the gates exhibit when floating in the waterway under a situation with flow in seaward direction. This situation occurs when the gates are emptied from ballast water and floating after retaining a high water peak, at this point the tide is typically receding, leading to seaward flow. The behaviour under seaward flow considers three different effects that occur during the same period:

- A compressive force in the connection between the gate and the guiding tower (indicated in red in Figure 3A), which pushes the retaining wall towards the parking docks, referred to as the **mystery force**.
- A quasi-constant change of the trim angle, which indicates a difference in vertical position between the two ends of the retaining wall (indicated in Figure 3B), referred to as the **trim angle effect**.
- A periodic oscillation of the retaining wall trim angle, in existing literature referred to as the **mode 3 effect**. This oscillation is associated with a standing wave in the waterway, which is amplified by the retaining wall movement.

In this report, this behaviour is referred to as the *seaward flow effects*, or more colloquially as just *the effects*.

For the mystery force no extensive information from the design phase is available, however from observations during operation a positive relation with the discharge is found. A relation with the river discharge squared has been suggested (Lamers, 2010), and even the discharge cubed (Duvivier & Nederend, 2013). These relations have not been found to be conclusive.

The trim effect has not been part of extensive investigation either during the design or operation phase, therefore it is not known upfront whether its magnitude has a relation with the flow.

The occurrence of the mode 3 effect was an important part of the investigation into the dynamic stability. During the design phase different types of physical tests and mathematical model calculations were performed, from which it was concluded that the effect only occurred for a big head difference over the barrier, and thus at a high flow rate (BMK, 1992c; WL|Delft Hydraulics, 1990b). The suggestion that follows from this is that if the mode 3 is already present at a relatively weak flow, the effect will increase in amplitude for higher flow rates.

The seaward flow effects may thus increase in magnitude for more extreme discharges, furthermore unexpectedly big loads due to these effects may impact the failure probability of the structure. For these reasons, the three effects are relevant to consider for further investigation.

1.2. Objective

The main objective of this study is summarized in the main research question:

Can the seaward flow effects exceed their respective tolerance limits in extreme situations?

In the main research question, extreme situations refer to situations with an extreme seaward discharge at the barrier. Tolerance limits refer to the different limits of the barrier that may be exceeded as a consequence of the considered effects, such as loads on specific elements of the barrier or maximum permissible displacements of the retaining wall.

To answer the main research question, a statistical analysis and a theoretical analysis using conceptual models are considered. To facilitate these two analyses, a literature review is considered to further describe the effect and identify possible influence factors. In a data acquisition step the effects themselves, and identified influence factors, are quantified based on data obtained from test closures from 2007 till 2021. From the conceptual models, supplemented by the established statistical relations, an extrapolation of the different effects is performed, based on which an answer to the main research question is formulated. From this description, the following collection of underlying research questions is formulated:

1. *Can a relation between the effects be identified?*
2. *Is the magnitude of the effects a function of hydraulic loading?*
3. *Can conceptual models physically model the effects?*
4. *What is the magnitude of the effects under extreme conditions, and how do they relate to the tolerance limits?*

1.3. Report structure

The structure of this report is summarized below, also indicating the relation with the research questions. It can be seen as reading guide to this report:

- Chapter 2: literature review, description of the Maeslant barrier and of the considered effects, including possible causal factors.
- Chapter 3: data acquisition, including an analysis of the magnitude of the three effects, and a visualization of the most important variables (sub-questions 1,2).
- Chapter 4: statistical analysis, used to describe relations regarding the magnitude of the effects (sub-question 2,3).
- Chapter 5: description and definition of considered conceptual models of the effects (sub-question 4).
- Chapter 6: interpretation of the conceptual models using the collected data. Extrapolations of the most relevant conceptual and statistical models to give an assessment of the effects under extreme conditions (sub-question 4,5).
- Chapter 7: discussion of the considered data, statistical analyses and conceptual models.
- Chapter 8: conclusions regarding the main research question. Suggestions for further refinement of the considered models and use of the models.

Maeslant barrier behaviour

For further understanding of the seaward flow effects this chapter describes the main characteristics of the barrier, the known dynamic modes of the sector gates (of which the mode 3 effect, considered in this report, is the only mode that occurs under a strong seaward flow), and the existing information on the considered seaward flow effects in more detail.

2.1. Maeslant barrier description

An overview of the barrier in a closed state is given in Figure 2.1, the names of the main elements as used in Dutch literature and an English translation as used in this report is given. It can be seen the gates consist of two main parts, the retaining walls and the arms which connect these to the ball joint. This report focuses on these retaining walls. When not in operation, the two retaining walls are positioned in the parking docks that are protected from the canal using a set of dock doors, making undisturbed passage of ships possible. The barrier closes only when an extreme storm surge is expected, the barrier closes when the predicted water level at Rotterdam exceeds +3.0 meters NAP (Rijkswaterstaat, n.d.-a). Yearly test closures take place in September.

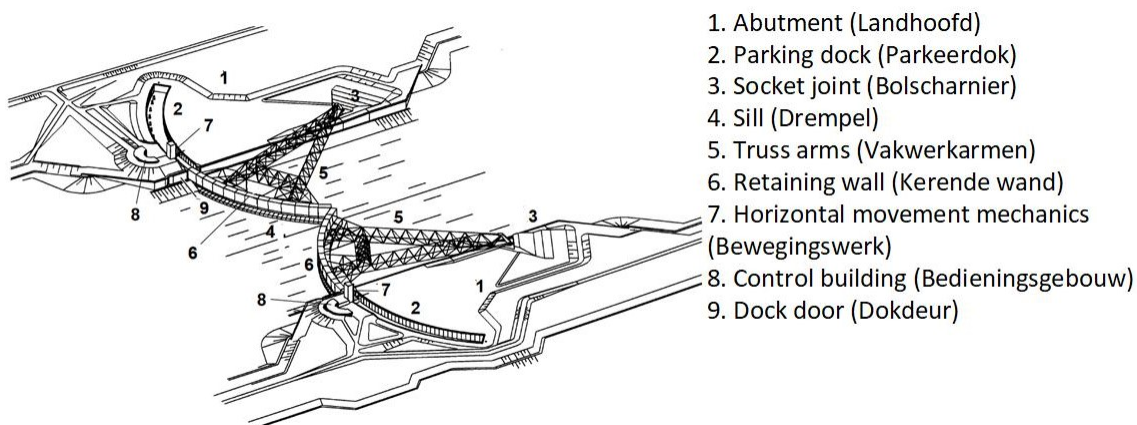


Figure 2.1: Maeslant barrier overview, image from Rijkswaterstaat, n.d.-a

The barrier follows a set operation procedure, for both storm and test closures. This operation procedure of the barrier can be summarized in 6 steps (Rijkswaterstaat, n.d.-a):

1. The parking dock water level is levelled with the river water level.
2. The dock doors open and the retaining walls are moved in the waterway using the horizontal movement mechanics.
3. The doors are sunk onto the sill by filling the ballast compartments of the retaining wall.
4. After the high water peak is passed, the doors are floated up by emptying the ballast components using pumps.
5. The retaining walls float in the waterway until conditions allow them to be floated back to the parking docks.
6. The retaining walls are moved in to the parking docks and the parking docks are subsequently emptied.

Step 5 is the phase when the effects, considered in this report, have been observed, this phase is also referred to as the *high floating phase*. Especially during test closures, this step can take multiple hours. The reason for this, is that a high enough water level is needed for the retaining walls to safely enter the parking docks. During test closures, no extreme water levels are present, and thus often a waiting period occurs before the incoming high tide increases the water level enough for the retaining walls to safely enter the parking docks.

2.1.1. Retaining walls degrees of freedom

To further understand the behaviour of the retaining wall, it is important to note the directions in which the retaining wall is free to move. These degrees of freedom are facilitated by the ball joint found in Figure 2.1. In total there are three degrees of freedom, these are shown in Figure 2.2 (Rijkswaterstaat, n.d.-b). A summary of these is given below:

1. turn angle: used to move the retaining wall in and out of the waterway, controlled with horizontal movement mechanics, see Figure 2.1.
2. sink angle: used to move the retaining wall onto the sill, controlled with ballast water in the retaining wall.
3. trim angle: plays no specific role during the operation, however needs to be kept within acceptable limits. It is controlled with the ballast tanks near the edges of the retaining wall.

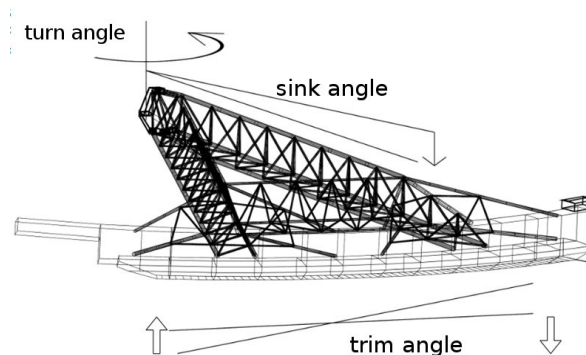


Figure 2.2: Retaining wall degrees of freedom, positive directions are as indicated in the figure, image from Rijkswaterstaat, n.d.-b

As can be seen from the given description, the degrees of freedom are needed for the barrier to fulfil its function. However, as a consequence of this, undesired effects may exhibit itself through movements in these degrees of freedom.

2.1.2. Load transfer

Transfer of the loads on the retaining walls to the foundations happens through two paths, as indicated in Figure 2.3a. Indicated with the green arrow is the radial part of the load that is transferred through the truss arms and ball joint to the foundation. A tangential part of the load may also be present, this is transferred through the horizontal movement mechanism and the guiding tower, as indicated with the red arrow in Figure 2.3a. Without this connection, the retaining wall would be free to move horizontally.

The force transfer between the retaining wall and guiding tower is facilitated with a connection referred to as the pull/push rod (trek-/duwstang in Dutch). A detail of this connection is shown in Figure 2.3b, in which this pull/push rod is highlighted. At this location the vertical movement is not restricted, thus no vertical force can be transferred to the guiding tower. The strength of the pull/push rod is estimated at 6,000 kN (Rijkswaterstaat, 2022b).

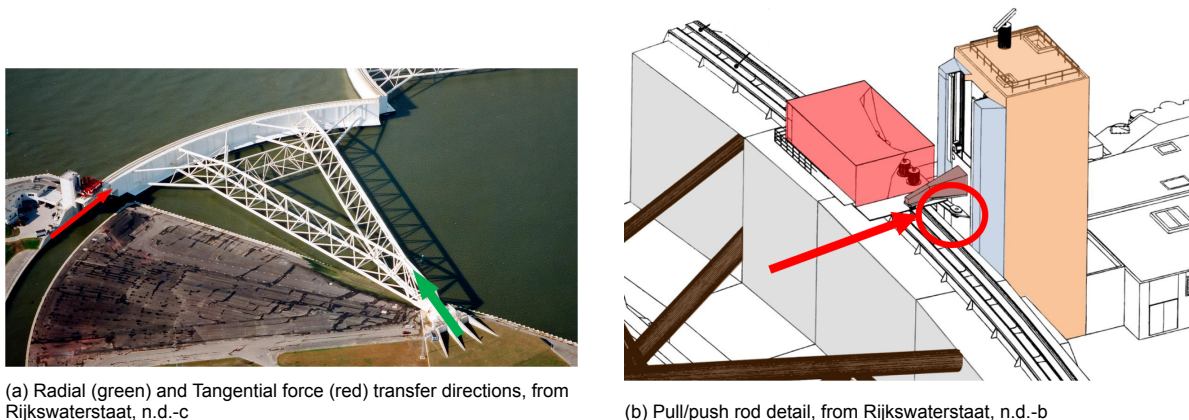


Figure 2.3: Maeslant barrier radial and tangential load transfer

2.2. Retaining wall modes

The two retaining walls float during different stages of operation, the retaining walls can exhibit a number of dynamic modes when floating. The different dynamic modes that may theoretically exist at the barrier are given below as defined in BMK, 1992c. These items were extensively researched during the design of the retaining wall:

- Mode 1: in phase vertical movement of the retaining walls: suction force* under the retaining wall can cause the retaining walls to lower faster than expected.
- Mode 2: out of phase vertical movement of the retaining walls: flow under the retaining wall may cause a 1st order standing wave over the channel cross-section, which can excite vertical movement of the retaining walls with a period of ± 60 seconds. Both retaining walls move out of phase with respect to each other.
- Mode 3: out of phase rotation of the retaining walls in the vertical plane, flow under the retaining wall may cause a 2nd order standing wave over the channel cross-section, which can excite a rotating movement of the retaining walls with a period of ± 30 seconds.
- Mode 4: In phase rotation of the retaining walls in the vertical plane, a theoretical mode of which the existence is not supported by models and scale tests.
- Mode 5: Independent vertical movement of the two retaining walls in an eigenperiod in the order of 10 seconds.
- Mode 6: Independent rotational movement of the two retaining walls in an eigenperiod in the order of 10 seconds.

An illustration of gate movement corresponding to the different modes is given in Figure 2.4.

*Suction force can be summarized as a loss of pressure head due to an increased velocity head, due to contracting flow under the barrier.

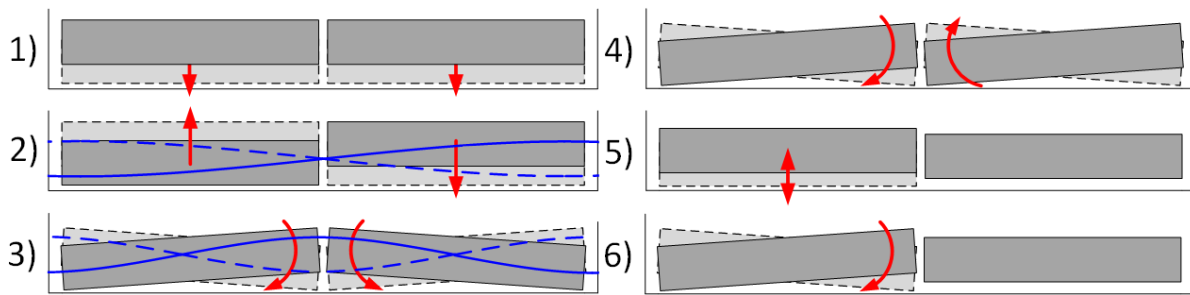


Figure 2.4: Cross-sectional view of waterway and movement of the gates with the corresponding standing wave where applicable (in blue)

2.2.1. Dynamic stability research

The study of the dynamic modes was an important part of the research during the design of the barrier, the main points of this study are given in this section.

Initially the retaining wall were designed with openings that facilitate flow, these would limit the head difference over the barrier during the closing and opening of the barrier. These openings were removed early in the design phase, this had a negative effect on the dynamic stability of the gates for modes 2 and 3 (WL|Delft Hydraulics, 1990a). This design choice lead to an extensive testing procedure, of which the goal was to find a shape for the retaining wall that keeps the occurrence of undesired dynamic behaviour within acceptable limits (BMK, 1992c; WL|Delft Hydraulics, 1990b). The mode 2 and 3 behaviour was not to occur during expected operational conditions. Study of these effects was considered important, since in some tests amplitudes of up to 8 meters were found (WL|Delft Hydraulics, 1990b).

The dynamic stability was assessed for situations where the sea level is higher than the river level and for situations where the sea level is lower than the river level (the seaward flow state as considered in this report). In the literature, these situations are referred to as a positive and negative head difference respectively. In both cases, the design had to be stable for gate opening/head difference combinations that were expected to have a probability of occurrence of 10^{-6} /year (BMK, 1992c). To do this, the extreme gate opening/head difference combinations were evaluated, see Figure 2.5 (Jongeling & A.D., 1995).

The dynamic stability of the gate was studied using various physical and mathematical models (BMK, 1992c).

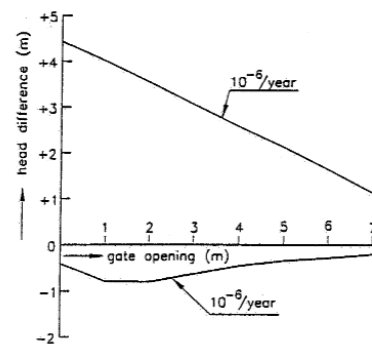


Figure 2.5: Considered stability lines, image from Jongeling and A.D., 1995

Physical models

Both 2D and 3D models were used to assess the dynamics of the design. The 3D scale model was a model of the barrier on a 1:60 scale. It is in this model that the impact of the dynamic modes has been first found (BMK, 1992c). For the final design, a sensitivity analysis was done in this 3D model to determine the influence of several factors on the gate stability (BMK, 1992c).

In the 3D-model, the displacements were measured as well as forces. Relevant displacements are the vertical displacements at the bank and river side of each of the two doors. Forces that are measured in this model are the forces in the ball joint and the tangential force acting in the push/pull rod (WL|Delft Hydraulics, 1990b).

To further examine and optimize the door design, a 2D-model was used. In this model a short section of the door design can be evaluated for its response to the flow, a schematic of this model can be seen in Figure 2.6. Pressure and displacement measurements in this model were used as a basis for the calibration of mathematical models (WL|Delft Hydraulics, 1991).

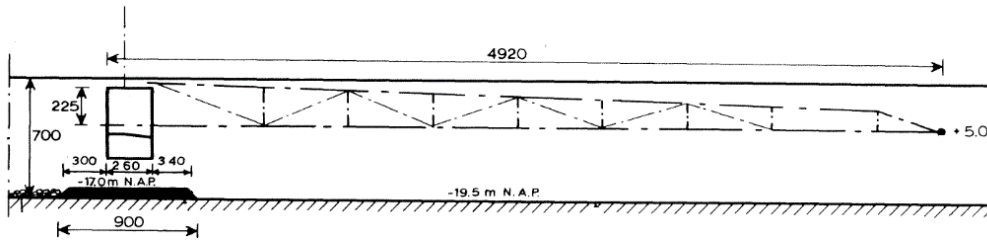


Figure 2.6: Overview of the 2D scale model (1:40 scale), longitudinal and top view, image from WL|Delft Hydraulics, 1990a

Mathematical models

Multiple mathematical models were developed to predict the behaviour of the retaining walls. These mathematical models of the retaining walls were developed with three goals in mind (BMK, 1992c):

1. Gaining insight in relevant excitation mechanisms.
2. Guiding the labour and time intensive physical experiments.
3. Extrapolating results for situations not evaluated in the physical models.

Regarding the dynamics of the final retaining wall design, the mathematical models were principally used to assess the effect of perforations that are present in this final design. These perforations, not present in the physical model (BMK, 1992b), are unrelated to the discharge openings in the original design. The perforations are relatively small holes in the retaining walls that are connected to passive compartments. These compartments follow the water level with a delay due to the small openings. The goal of these perforations and compartments is to increase the stability of the retaining wall while keeping the amount of water used as ballast limited. This design choice reduces the required pumping capacity.

To determine the dynamic stability of the retaining wall for mode 3 two mathematical models were made with a different theoretical basis:

- Model based on discharge variations induced by gate movement and water level changes (BMK, 1992c).
- Model based on a mass spring system analogy where the door is connected with springs to the water levels and solid ground (BMK, 1992b).

Using two different mathematical models increased confidence in the obtained results. Both these models relate to quantities measured in the 2D model (BMK, 1992b). An overview of the main characteristics of the two models is given below.

Discharge variation model

This model describes how a change in downstream water level (h_s) relates to a change in discharge per unit width under the gate (Δq). To understand how an initial change of water level influences the discharge under the gate, this discharge is described using Torricelli's law:

$$q = \mu d \sqrt{2g(d_r - d_s)} \quad (2.1)$$

With (see Figure 2.7):

- q (m^2/s): discharge per unit width
- μ (-): discharge coefficient
- d (m): vertical flow gap
- $g = 9.81 \text{ m/s}^2$: gravitational constant
- d_r (m): riverside water depth
- d_s (m): seaside water depth

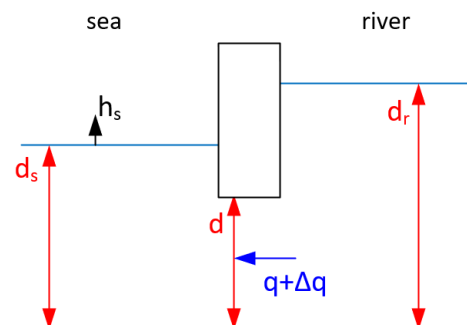


Figure 2.7: Discharge variation model definitions

A seaside water level change, h_s , on the seaside, see Figure 2.7, influences terms given in Equation 2.1:

- By definition, a change of h_s for the water depth on the seaside: d_s
- The gate moves vertically with the water level change, influencing the vertical flow gap: d
- The change in gate opening may influence the discharge coefficient: μ

The basis for the model is the relation between a change in the down stream water level and a resulting change of the discharge under the gate (WL|Delft Hydraulics, 1991). If an increase in the downstream water level causes an increase of the discharge, the initial raise in water level is amplified, and the system is unstable. This relation is described using a factor α_{stab} :

$$\alpha_{\text{stab}} = \frac{\partial q}{\partial h_s} \quad (2.2)$$

This factor was determined from measurements in the 2D scale model, by measuring the change in gate position due to a varying discharge. This factor changes when the vertical gate opening changes. An analytical solution of the value of α_{stab} can be inferred by assuming that the discharge coefficient only varies slightly with the opening, and assuming that the discharges are small (Bakker et al., 1991):

$$\alpha = \mu \sqrt{2g(d_r - d_s)} \frac{\partial d}{\partial h_s} - \frac{1}{2} \mu d \sqrt{\frac{2g}{(d_r - d_s)}} \quad (2.3)$$

With:

- $\frac{\partial d}{\partial h_s}$ (-): relation between water level change and retaining wall movement
- other terms are as defined in Equation 2.1.

The relation between the water level change and door movement has to be determined from results from the 2D scale model, the result is therefore not a fully analytical expression.

Spring model

This model considers a system that can be described as a gate connected with springs to the two water levels and to the bed, this system is described in BMK, 1992b. In this document, the derivation of the governing equations is also given. An overview of this system is given in Figure 2.8.

This system is described with a second order differential equation for the vertical movement u , which in simplified form reads (the terms relating to the perforations and a change of ballast are for simplicity not shown) (BMK, 1992b):

$$m\ddot{u} + c\dot{u} + k_t u = k_z h_z + k_r h_r \quad (2.4)$$

With mass and damping terms m and c , and terms as defined in Figure 2.8. k_t in this model is the sum of the three different spring stiffnesses. To solve this equation the system is supplemented with equations relating to the discharge under the gate, this discharge in turn relates to the water levels and the position of the retaining wall, similar to the discharge variation model.

In this system the spring stiffnesses are not constant but vary with the head difference and the opening under the gate. The spring stiffnesses are, among other factors, modelled as dependent on the suction force under the gate, a magnitude that has been determined from the scale model tests (BMK, 1992b).

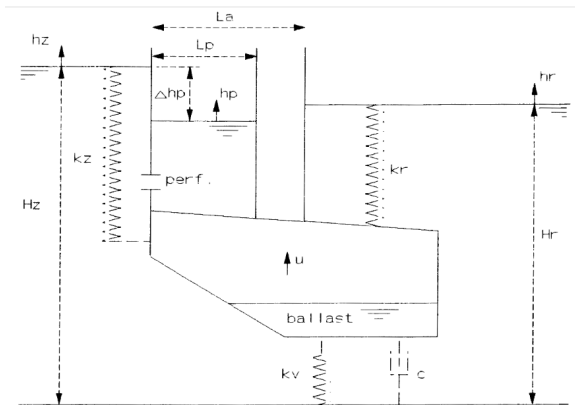


Figure 2.8: schematization of the mass spring model from, image from BMK, 1992b

Findings overview

Using a combination described models, many distinctive designs for the retaining walls were assessed to arrive at a design that is sufficiently stable during all expected conditions. These different door designs were evaluated and tweaked to arrive at the final door design.

During the design studies the main modes that are of influence are modes 1, 2, 3 and 5 from Figure 2.4, of which only the mode 3 effect is considered in this report (BMK, 1992c).

The final design has two skirts on the bottom of the retaining wall, as shown Figure 2.9. The skirts are instrumental to the stability of the wall and function by impacting the pressure distribution on the bottom of the retaining wall.

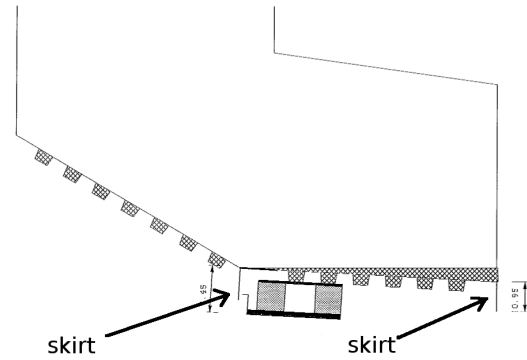


Figure 2.9: Final retaining wall cross-section sketch, image from BMK, 1992c

2.3. Mystery force

The mystery force has not been explicitly identified in the design phase, it is an effect that has mainly been noticed during test closures. The mystery force is a force that has been measured while the gate is floating in the waterway, the high floating phase from the operation description in section 2.1. It is an unexpectedly high compressive force that is present in the pull/push rod that connects the gates horizontally to the guiding tower, as shown in Figure 2.3b.

This force is measured by strain gauges on the pull/push rod and derived from pressure measurements in the horizontal movement mechanism. The mystery force, considered in this report, is the part load on the pull/push rod that fluctuates slowly through time. Other contributions, such as due to the mode 3 effect and irregular wave loads are responsible for low period fluctuations, and are not considered to be part of the mystery force.

The time history of this mystery force during the high floating phase has been noted to have a shape similar to the time history of the discharge (Lamers, 2010). The forces observed are significantly lower than the characteristic strength of the pull/push rod, the observed mystery force has never been higher than 750 kN (Duvivier & Nederend, 2013), while the characteristic strength of the connection is 6,000 kN (Rijkswaterstaat, 2022b).

The mechanism behind this component of the observed force is not well understood, and does not appear to be thoroughly researched. However, some observations on the force in pull/push rod are available from both the 3D scale model tests and limited research during the operation phase.

2.3.1. Model research

As mentioned in subsection 2.2.1 the force in the pull/push rod, the tangential force, was measured in the 3D physical model. From this, a load has been found that increases with an increasing head difference over the barrier and a decreasing vertical flow gap under the retaining wall (WL|Delft Hydraulics, 1990b). The force measured in these 3D tests has been noted to be smaller than the observed effect in the prototype (Bakker, 2008). Furthermore, the 3D model tests paid no extensive attention to the tangential force during the high floating phase, since it was not considered to be a governing situation.

2.3.2. Empirical relations

A correlation between a peak in the local discharge and this component of the force has been researched based on the measured force and numerically calculated discharge (Duvivier & Nederend, 2013; Lamers, 2010). Based on this, relations between the computed local discharge and the mystery force have been proposed, where the force scales with the square or cube of the calculated local discharge. The fit of these relations is limited, and the results vary between the different years (Duvivier & Nederend, 2016), it therefore is uncertain whether these are the most appropriate relations.

2.4. Trim angle effect

The trim angle effect is an increase of the trim angle (Figure 2.2) under strong seaward flow. This effect has not been seen to directly relate to additional loading on the structure, if necessary it can be controlled, and no extensive research into this effect has been done.

This effect occurs during the same period as the mode 3 and mystery force effects, during the high floating phase. During this period, a quasi-steady increase of the trim angle is present. An increasing trim angle entails that the retaining wall is submerged deeper in the middle of the waterway compared to near the bank.

2.4.1. Model research

In the reports on the 3D-model tests, some attention is paid to the gate position under high seaward discharges.

In the 3D model tests, the gate position is described for a zero discharge and a discharge of 16,000 m³/s (WL|Delft Hydraulics, 1990b). The trim angle is not explicitly given, instead the vertical movement of the retaining walls is given at both ends of the retaining wall. Using the difference in displacement between the two ends and the approximate distance between the two ends of the retaining wall, 200 m (WL|Delft Hydraulics, 1990b), the trim angle effect may be approximated (in milliradians):

$$\theta = \frac{(\delta_{\text{river}} - \delta_{\text{bank}})}{L} = \frac{(3.82 - 2.37)}{180} = 8.1 \text{ mrad} \quad (2.5)$$

with:

- $\delta_{\text{river}} = 3.82$ m: retaining wall vertical displacement in middle of the waterway
- $\delta_{\text{bank}} = 2.37$ m: retaining wall vertical displacement at the bank of the waterway
- $L = 180$ m: half the waterway width

Only information on the trim effect under an extreme discharge is available, no information regarding the exact relation between the trim angle and discharge can be obtained from the physical model tests. It also has to be noted these test were performed to assess the behaviour during the moving in and out of the waterway. For this reason, these test were performed with the gates partially opened, the horizontal opening was 10 meters (WL|Delft Hydraulics, 1990b).

2.5. Mode 3 effect

From the six dynamic modes described in section 2.2, this thesis considers only the mode 3 effect. This is the effect that may occur under a seaward flow (BMK, 1992c). This mode 3 effect represents an oscillatory movement of the two retaining walls together, as shown in Figure 2.4.

2.5.1. Model research

The existence of this movement in combination with a standing wave is briefly explained according to the theory developed during the design phase (BMK, 1992c). First, it is important to note that between the banks of the waterway standing waves may exist. This standing wave causes the retaining wall, which floats on the water, to move along with this wave. This movement causes a change of the flow rate under the gate that under certain conditions can amplify the standing wave.

For the mode 3 effect to occur, the conditions do need to be such that the discharge fluctuations that occur under the retaining wall amplify the standing wave. This was extensively researched during the design phase, using mathematical and physical models as described (subsection 2.2.1). From the 3D model tests during the design phase, it was found the mode 3 effect could exist when the following conditions were met (WL|Delft Hydraulics, 1990b):

- The vertical opening was bigger than 3 meters.
- The head difference was bigger than 1.5 meters.

Furthermore, the time span required for mode 3 to build up is found to be 15-50 minutes (BMK, 1992c).

The effect of some possible influence factors on the mode 3 effect is described based on research in the 3D model (BMK, 1992c):

1. Low river levels have a negative impact on the stability
2. Impact of the trim angle on the stability is limited
3. Wind waves have no impact on the stability

A summary of the findings on this type of behaviour can be found in Kolkman and Jongeling, 2007, p. 107-110 and p. 189-191.

2.5.2. Empirical findings

An oscillation of the retaining walls that seems to correspond with the mode 3 effect has been registered during a number of the yearly test closures (Duvivier & Nederend, 2013). The magnitude observed is limited with a maximum amplitude with an order of magnitude of 10 centimetres. This is unexpected, because of the limited discharge at the barrier during the test closures no occurrence of this effect is expected based. Such a limited discharge leads to a limited head difference, which, based on the criteria formulated from the physical model results, should not lead to occurrence of the mode 3 effect.

2.6. Summary

The barrier consists of two sector gates whose vertical position is controlled with ballast water, after retaining a storm surge the ballast water is removed and the retaining walls return to a floating state. During this period, the receding tide induces flow in seaward direction.

The retaining walls have three degrees of freedom, of which the trim angle is the most relevant for this report. The load on the retaining wall is transferred through in two ways, the radial part of the load is transferred through the ball joint, the tangential part to the guiding tower.

During the design phase, the dynamic behaviour of the retaining wall has been excessively considered with both physical and mathematical models. It was found that an in-phase rotational movement of the retaining walls could occur when a strong flow was present in seaward direction is present, based on the list of the 6 theoretical dynamic modes this effect is known as mode 3. The mode 3 behaviour is the result of interaction with a standing wave in the waterway.

The mystery force is a force that appears related to tangential loading on the retaining wall. This force has been measured in physical models, but has been noted to be smaller than observed in reality. Forces up to 750 kN have been observed, The most critical element appears to be the pull/push rod that transfer the tangential load to the guiding tower which has a strength of 6,000 kN.

The trim angle effect does not directly relate to additional loading on the structure it has not been studied extensively, during the design phase or during operation. Some limited data is available on the displacement under a discharge at the barrier of 16,000 m³/s.

The mode 3 effect has been observed for situations where it was not expected to occur, the amplitude is limited for the observations. The design phase research pointed to occurrence of the effect for relatively extreme head differences (1.5 m), while the local discharge, and as consequence the head difference are limited.

3

Data acquisition

A dataset is compiled to analyse the magnitude of the different seaward flow effects, as introduced in chapter 1 and described in chapter 2. Furthermore, this dataset quantifies factors that may influence the seaward flow effects. The taken data acquisition steps are (each step corresponds to one subsection):

1. **Selection** of the relevant data types.
2. **Collection** from various sources
3. **Processing** the data for further analysis
4. **Description** of the obtained dataset
5. **Quantification** of the seaward flow effects
6. **Visualization** of data during the considered time period
7. **Summary** of the obtained dataset

3.1. Data selection

3.1.1. Considered data types

Data on the mode 3 and trim angle effect follows from the trim angle measurements of the retaining wall. Data on the mystery force effect has been collected using strain gauges on the pull/push rod and derived from pressure measurements.

To gain insight in the influence factors on the seaward flow effects, information on the hydraulic conditions is required. The different effects researched are presumed to relate to the hydraulic conditions, since they only occur under a seaward flow. The different considered data types regarding hydraulic conditions are given below:

- Discharge as calculated from numerical model
- Sea side water level
- River side water level
- Parking dock water level
- Vertical flow gap

To gain further insight on possible influence factors, additional data types are identified which may be linked to a role in the observed effects:

- Wind characteristics
- Lobith discharge

The link between these data types and the observed effect may be direct, such as a wind load impacting the retaining wall response. However, the relation be indirect, the hydraulic conditions may be influenced by the wind characteristics or the discharge of the Rhine river.

3.1.2. Considered closures and time period

For this study, the data collected at the barrier is available for a limited set of closures. The data is available for test closures from 2007 to 2021, in this report these closures are referred to using the letters 'FS' and the relevant year (this naming format is adopted from existing documentation). One closure under storm conditions took place in 2018 for which data is also available. This leads to a total of 16 closures for which data is available. Two closures do not have the relevant period of time, where the considered effects can occur (the 2016 test closure and 2018 storm closure), this decreases the amount of closures with relevant data to 14. Data for the 2007 closure is limited, no information on the mystery force is available, consequently there are 13 closures with data for the mystery force.

The data is in principle available for the full closure. However, the phase identified as the high floating phase is considered the most relevant for this report (defined in section 2.1), since this is the period where the different considered effects occur. For this reason, the duration of this period for the different considered closures is further treated.

To further specify, the high floating stage starts when the barrier is fully raised after the high tide, by removing the ballast water. The vertical flow gap under the barrier reaches a local maximum before it decreases due to the receding tide. This peak in the opening indicates the start of the high floating phase. The high floating phase ends when the retaining walls are moved back into the parking docks. As mentioned in section 2.1, a minimum water level is needed for the retaining walls to safely return to the parking docks. If this level is not present at the start of the high floating phase, this phase only ends when the next incoming high tide increases the water level sufficiently.

The time span of the high floating phase per closure are given in a bar chart in Figure 3.1. During most test closures, at least 6 hours are spent in the high floating phase. For the 2018 storm closure, the retaining walls were almost immediately returned to the parking docks. For this reason, the 2018 storm closure is disregarded when analysing the high floating behaviour. This is intuitive, for storm closures the high wind set-up decreases the likelihood of a long waiting period before returning to the parking docks. The 2016 test closure is disregarded because during this closure the barrier was not fully closed leading to only small head differences over the barrier during the high floating phase, because of which it is unsuitable to compare to the other closures.

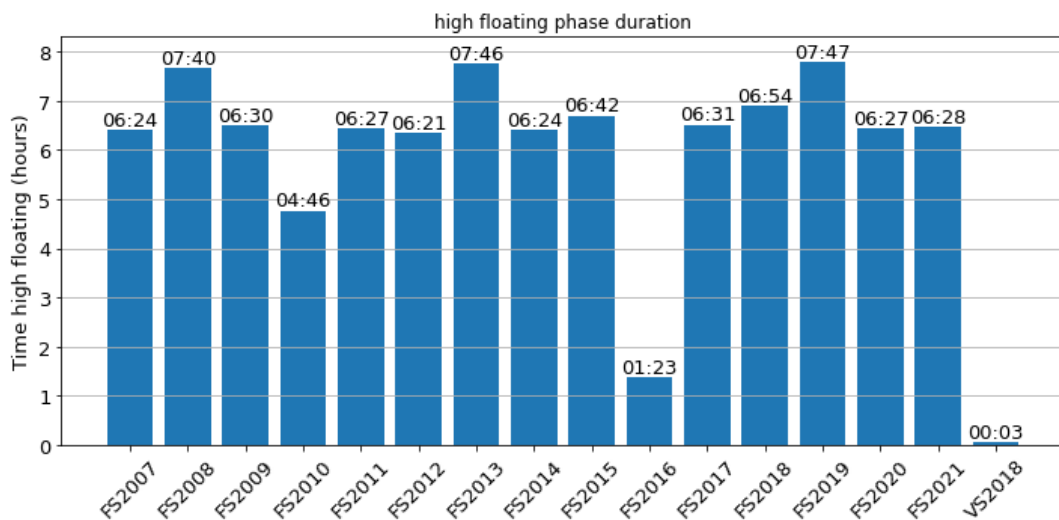


Figure 3.1: Time between end of de-ballasting and returning to docks per closure, time given in HH:MM format. 'FS' indicates the different test closures, 'VS' indicates the closure under storm conditions

3.2. Data collection

3.2.1. Barrier data collection system

During operation, data is collected at the barrier. In general, the data from this system is not equidistant, that is to say the time step between the different data points shows variation.

Gate position data

Position data is obtained from inclinometers placed inside the retaining wall and gate arms, as shown in Figure 3.2. At each of the marked locations, 3 individual inclinometers are present for redundancy and to increase precision of the results (CROON elektrotechniek, 1998; Rijkswaterstaat, n.d.-a). In this report, only the measurements from the trim sensors are directly considered (the sink angle sensors are indirectly relevant for the vertical flow gap).

The structure of the trim angle data can be briefly described in the following manner. The mode of the non-equidistant temporal resolution is one second. For both retaining walls separate data is available. For the closures from 2007 to 2012 one data stream is available for each retaining wall. For the closures since 2012 separate data streams are available for the inclinometer locations marked in Figure 3.2. The different data streams are indicated by their location, one is on the *river side* the other on the *bank side* of the retaining wall. The spatial resolution of the data is estimated at 0.01 mrad. Details on the analysis of the data resolution of the trim data is given in Appendix A.

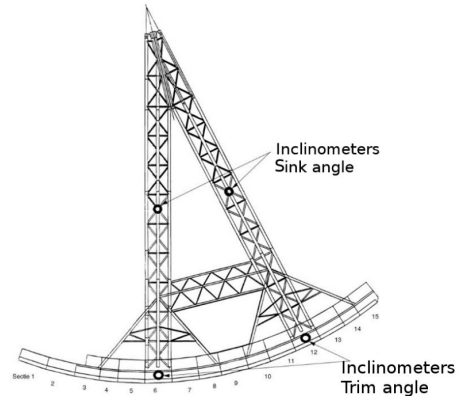


Figure 3.2: Locations of sink and trim angle inclinometers, image from Rijkswaterstaat, n.d.-b

From the measured sink angle, the vertical flow gap is derived. The structure of this data is similar to that of the sink angles, with as difference that the temporal resolution is lower, the mode of the non-equidistant temporal resolution is four seconds. The spatial resolution is estimated at 1 cm (a sink angle resolution of 0.01 mrad would lead to a resolution even lower than 1 cm).

Water level data

Water level data is collected from measurement stations at both the sea and river side of the barrier. These measurement stations are present on both the north and south river banks, as marked in Figure 3.3. Not shown are the measurement locations present in the parking docks. The data is collected using multiple pressure sensors at each location (CROON elektrotechniek, 1998).

Separate data streams are available for the sea and river side of the barrier, but not for the north and south locations separately. The mode of the non-equidistant temporal resolution is one minute, the spatial resolution of the raw data is 1 centimetre.

For both the north and south parking docks, separate data is available. The mode of the temporal resolution for these data streams is higher at one second.



Figure 3.3: Approximate location of water level measurement stations, inferred from satellite pictures. Background image from Google Earth, 2022

3.2.2. Pull/push rod data

The data on the load in the pull/push rod is collected separately from the other data at the barrier. Data For limited closures the full time range is available with a temporal resolution of 0.3-1 seconds. The data consists of data streams for the load based on two pairs of strain gauges that are located on the pull/push rod. Furthermore, the load is derived from the hydraulic pressure in the horizontal movement mechanics (marked in Figure 2.1).

For not all closure operations, the complete data on load in the pull/push rod is available. Another, more indirect, data source is used for these closures. After each closure, a report with its most important characteristics is written. From these reports, a maximum value for mystery force can be obtained.

It is unclear if for every closure this reported value is obtained in the same manner, the use of absolute peaks of the mystery force or an average value over a longer period of time can have an impact on the data. This uncertainty should be considered in further use of this data. Furthermore, for 2007 data on the mystery force is missing, reducing the number of closures with mystery force data to 13. From 2015 on data was collected at both the north and south pull/push rod, before 2015 data was only collected at the south pull/push rod.

3.2.3. KNMI data

At one of the towers of the barrier, data on the wind conditions is available. However, wind data collected at the barrier is not available for all closures, therefore the KNMI weather station at Hoek van Holland is used as a fallback (KNMI, 2022). It is located 4.9 kilometres from the barrier, as illustrated in Figure 3.4.

The data is collected at a data interval of 10 minutes. The different variables selected from the dataset used to describe the wind conditions in this report are:

- mean wind speed
- maximum wind speed
- mean wind direction



Figure 3.4: Location KNMI weather station relative to barrier. Background image from Google Earth, 2022

3.2.4. Numerical discharge model

The time history of the local discharge is calculated based on a one-dimensional numerical model modelled by Deltares (Deltares, 2019). This model uses information on the gate position to determine the water levels around the gate and the discharge at the barrier (Deltares, 2019). The computed discharge at the barrier is given in a 10-minute time step.

The numerical model is only one-dimensional, this raises the question whether this model is sufficiently accurate to model the barrier with a three-dimensional shape. The discharge model has been compared against one set of flow measurements during the 2011 test closure. The difference in peak discharge was noted to be 4% (Hessels, 2011), the model appears to be sufficiently accurate. It has to be noted that the discharge during the 2011 test closure was limited, and as such cannot give full verification of the model predictions for strong seaward flows.

For not all closure operations, the full data on the computed discharge is available. The written reports after a closure are used as an indirect data source. From these reports, the peak value for the discharge during the high floating phase is obtained.

3.2.5. Lobith discharge

The influence of the river discharge is judged by the discharge of the Rhine river at Lobith (obtained from Rijkswaterstaat, 2022a). The daily average of this discharge is used. Because there is a delay between the discharge at Lobith and the discharge at the barrier due to the physical discharge, the seven days before the closure are considered.

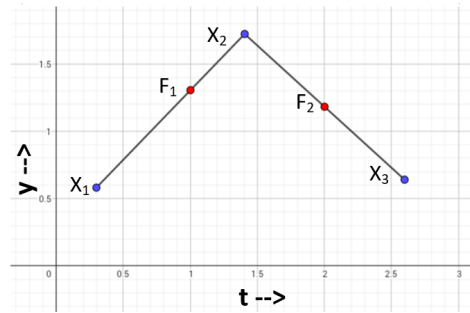
It has to be noted that the Rhine is not the only upstream contribution of the discharge, and that tidal effects are expected to have a bigger effect on the discharge at the barrier.

3.3. Data processing

3.3.1. Data time series processing

From the non-equidistant data obtained at the barrier, an equidistant data is constructed. This is done by transforming the original trim data to a time interval equal to the mode of the non-equidistant data. For the vertical opening the mode of 4 seconds is not used, since this data will only be used to give a general indication of the gate position, not to resolve the low period mode 3 behaviour. 1 minute was chosen as time step. The value at each data point is found by performing a linear interpolation between the two enfolding data points from the original data, using a linear interpolation function (Scipy Community, 2022a).

The method is illustrated in Figure 3.5 using a small fictitious set of irregularly spaced points $[X_1, X_2, X_3]$. It can be seen that between these points linear interpolations are done to find the values at regular time intervals leading to the equidistant dataset F . It can also be seen that this method has a peak shaving effect on data, the peak value has been reduced by this resampling. When applied to the data this leads to a transformed signal as shown in Figure 3.6, it can be seen that for periods higher than the resampling frequency this peak shaving effect is a lot less pronounced.



For comparison, a second method is shown in Figure 3.6, using a standard resampling function to obtain equidistant data (Pandas, 2022a). It can be seen that the resampled signal shows a shift of the registered values, since for each equidistant point the value is determined by the original data that falls within a bin around the equidistant point. Often this is only one data entry, leading to a shift of this data entry in time. With this method, there may be points for which no original entries are present in the created bins. For these points, an interpolation is performed between the equidistant points that can be determined.

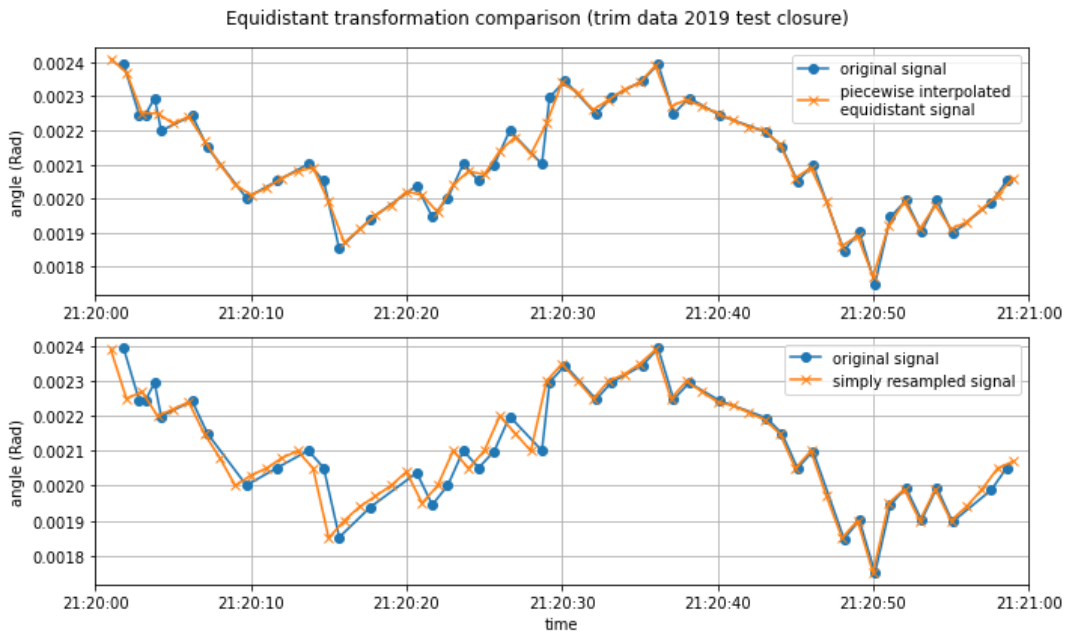


Figure 3.6: Transformation to equidistant signal method comparison

From Figure 3.6 the overall difference between the two methods appears minor, especially when only the high period variations (30+ seconds) are considered. The second method has less of an effect on the peaks but may impact the periods found when analysing the signal and is therefore not used in this report.

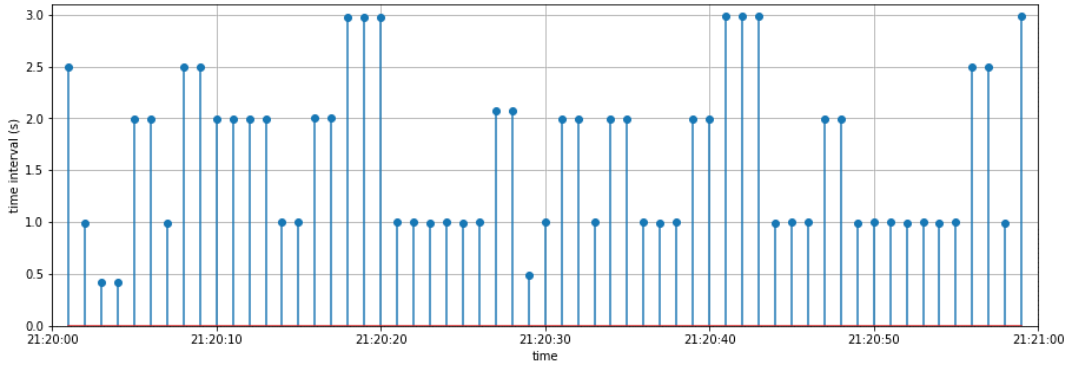


Figure 3.7: Equidistant signal interpolation interval of the signal in Figure 3.6

By transforming to equidistant data, some information is lost regarding the collected time intervals. This information may be relevant when judging if the original signal is able to resolve a certain frequency. For each interpolated point it is determined over which time interval the interpolation was done as a measure of the original collection frequency, a sample of the data from Figure 3.6 is shown in Figure 3.7. This time interval is stored as a separate entry in each relevant data file.

Pull/push rod resampling

The data collected regarding the load in the pull/push rod is collected with a 0.3-1 s temporal resolution. However, for the mystery force, only the time averaged force over a longer period is of importance. To obtain the load component belonging to the mystery force, the 5-minute moving average is taken from the original signal (Pandas, 2022b).

3.3.2. Data combination

From the observed sea and river side water levels, the head difference over the barrier can be determined. This head difference is obtained by subtracting the observed river water level, d_r from the observed seaside water level, d_s :

$$\Delta h_g = d_s - d_r \quad (3.1)$$

This quantity is in this report referred to as the *global* head difference over the barrier, since it relates to the measurement location positioned relatively far away, as marked in Figure 3.3. Because of this distance, it may deviate from the unknown *local* head difference over the retaining walls.

3.3.3. Data formatting

Some of the data collected at the barrier is delivered in an unrealistically high number of decimal places. To make the final dataset more transparent, the resolution is changed such that it matches the predicted precision of the sensors. This is done in a straightforward manner by rounding the data to the expected resolution for the different data streams, given in section 3.2.

3.4. Data description

Table 3.1 gives a summary of the different data types used in this report.

Data type	Description	Time step	Main limitations	Data Resolution
Trim angle	The angle the retaining wall in longitudinal direction makes compared to the horizontal.	1 second	The retaining wall is not entirely rigid, so the trim angle is not constant over the wall.	0.01 mrad
Sea and River side water level	Water level data collected at the sea and river side of the barrier.	1 minute	The frequency is too low to resolve dynamic retaining wall behaviour.	1 cm
Parking dock water level	The water level in the parking docks.	1 second	The parking dock water level is partly shielded from the waterway.	1 cm
Vertical opening	The opening between the sill of the barrier and the bottom of the retaining wall	1 minute	Lower temporal resolution compared to the sink angle.	1 cm
Pull/push load	Load in the pull/push rod measured from strain gauges and determined from the hydraulic pressure in the movement mechanics	5 minute	Strain gauge measurements are up to 2015 only done on the south retaining wall. For the north retaining wall data is not available, or based on pressure which has limited value.	1 kN
Wind data	Mean/max wind speed and direction as measured at KNMI station Hoek van Holland	10 minutes	Located five kilometres from the barrier, spatial variation in the wind will play a role.	0.01 m/s, 1 degree
Numerically computed local discharge	Local discharge at the barrier calculated with a numerical model after the closure event	10 minutes	Limited time resolution and based on a rough schematization of the barrier, does not take into account 3D effects of the barrier.	1 m ³ /s
Lobith discharge	Daily average of the Rhine River discharge at Lobith.	Daily average	A delay compared to the river discharge at the barrier can be expected, as well as variations due to contributions other than the Rhine from Germany.	1 m ³ /s
Global head difference	Difference between Sea and river side water level	1 minute	The local head difference at the barrier may deviate due to the distance between the stations.	1 cm

Table 3.1: Final dataset items directly derived from raw data

3.5. Quantification of effects

3.5.1. Mystery force

The mystery force (the unexpectedly large load on the pull/push rod) follows from the 5-minute moving average, that is obtained through the processing step in subsection 3.3.1. This avoids contributions of lower period effects that are not part of the mystery force. For each of the three different data streams (the sets of strain gauges, and the relation with hydraulic pressure) the maximum mystery force magnitude is determined based on this moving average. From this, it follows that the mystery force based on the hydraulic pressure differs significantly from the results of the strain gauges (as can be seen in section 3.6).

For most closures, 9 in total, the raw data is not available. As described previously, data for those years is taken from reports written after every closure. The exact method for determining the maximum mystery force reported is unclear, reducing reliability of the mystery force data. For uniformity only one measure for the mystery force is desired, when distinctive values for the two retaining walls are given (the closures since 2015) the mean of the two values is used.

3.5.2. Trim effect

The magnitude of the trim effect (the quasi-constant trim increase under an increase of the seaward discharge) is in this thesis defined as the difference between the maximum trim angle found during the high floating phase and the minimum trim angle during this phase. The minimum trim angle is included because other effects, such as remaining ballast water, may have a constant influence on the retaining wall pitch during the whole high floating phase, that should not be considered for the trim effect. The 5-minute moving average of the trim angle data is analysed, this to avoid contributions of low period effects that are not part of the quasi-constant trim angle effect.

For closures before 2013 the analysis is simply done for the one available signal per retaining wall. For closures since 2013 two trim angle signals per retaining wall are given. To get one measure for the trim effect, the average magnitude over the results per signal are used.

For multiple closures this analysis method did not immediately yield appropriate results, at the beginning of the high floating phase effects of the ballast water removal of the walls were still visible as relatively fast changes of the trim angle. For closures where this was the case, the first 30 minutes of the signal were disregarded, which removed the effects of the de-ballasting phase. As reference, the results for the different closures are given in Figure C.1.

3.5.3. Mode 3 analysis

For the mode 3 effect (the oscillation of the retaining walls in trim), that is only present for a limited period of time, power spectra are constructed from the trim angle signals. This spectrum is constructed with a wavelet transform, which can be seen as breaking up the trim angle signal in a set of small parts of a sinusoid, referred to wavelets. Further explanation on this method is given in Appendix B (based on Torrence and Compo, 1998, with scripts for the analysis obtained from Torrence and Compo, 2018). This method is better suited for this use case than a regular Fourier transform. The mode 3 effect does not have a constant magnitude over time, which can be seen from the resulting two-dimensional power spectrum that the wavelet analysis gives. In this section, the mode 3 effect is quantified based on the spectra obtained from the wavelet transform.

Mode 3 band identification

From the constructed power spectra, the period band in which the mode 3 effect exhibits itself is identified. It has been already noted the period as observed for the mode 3 effect is about 35 seconds (Duvivier & Nederend, 2013). To illustrate the band in which the mode 3 can be seen, the slice of each power spectrum with the highest variance at 35 seconds is selected for every closure. The results are shown in Figure 3.8, where for clarity only the closures with a clear mode 3 effect are given.

This analysis is done is for the signal collected at the north retaining wall. The result for the south retaining wall can however be expected to be similar, since mode 3 requires an oscillation of both retaining walls through the shared standing wave (see section 2.5).

From Figure 3.8 it is concluded that the mode 3 effect is found in a band with periods from 27-47 seconds, indicated with vertical lines. The 2007 test closure deviates slightly from this trend. A significant change in water levels may change the frequency of the system, causing a shift of the peak in the frequency domain (due to a change of the wave velocity). However, the 2007 closure shows no significantly different water levels (Appendix D). The reason for this deviation remains unknown.

In further analysis of the mode 3 behaviour, the scale averaged wavelet power (see Appendix B) for the mode 3 effect is determined for the found 27-47 second band. To reduce the noisiness of the power spectrum, the 5-minute moving average of the scale averaged wavelet power is considered to analyse the mode 3 effect, analogous to the method for the mystery force and trim effect.

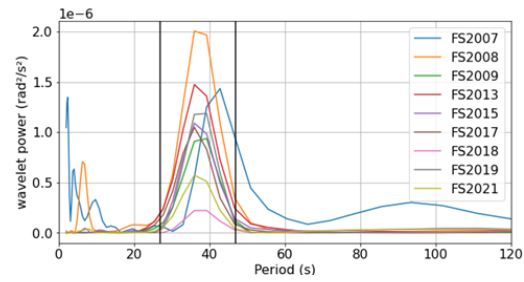


Figure 3.8: wavelet power spectrum at moment of mode 3 peak (only closures with an identified mode 3 effect)

Wavelet analysis qualitative result

Based on the above identification of the relevant period band, an illustration of the wavelet analysis can be given, see Figure 3.9. Two trim angle signals from the 2019 test closure are considered for the high floating phase. This plot contains three elements, Figure 3.9a gives the trim angle signals, Figure 3.9b the 2-dimensional wavelet power spectrum for the signal of the north retaining wall, and Figure 3.9c the wavelet power as determined for the mode 3 period band (note the logarithmic scale). The wavelet power in Figure 3.9c is determined from Figure 3.9b as described in Appendix B.

From Figure 3.9 it can be seen that for part of the signal a clear mode 3 effect can be seen. The effect is the strongest between 21.00 and 22.00. This appears to be typical for the mode 3 effect, and based on this the effect itself is further quantified. Outside this clear peak, noise can be seen that cannot be ascribed to a clear mode 3 effect.

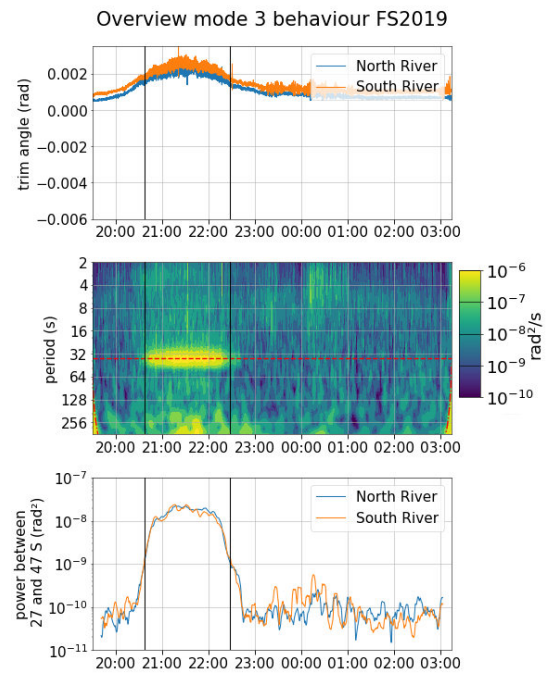


Figure 3.9: Wavelet analysis of the 2019 trim signals

Trim angle mode 3 quantification

To compare the mode 3 effect of different closures, the duration of the mode 3 effect and the peak variance of the mode 3 effect is considered for each of the available trim angle signals.

To determine the duration of the mode 3 effect, the time span that a chosen threshold is exceeded is determined for each of the signals. From interpreting the results such as in figure 1 this threshold is chosen as $1 \cdot 10^{-9}$ radians². The found time span is indicated in Figure 3.9 with the black vertical lines. Since the mechanism takes time to build up, only areas where the threshold is exceeded for 30 minutes or longer are considered. The considered peak variance is the maximum value of the 5-minute moving average of the scale-averaged wavelet power. If the given threshold value is not exceeded for 30 minutes or more, the duration and peak variance are both defined to be 0.

For the data prior to 2013 one signal per retaining wall is available. For data from 2013 on, the signals for bank and river side sensors of the retaining are both analysed and the mean of the duration and peak value is used to determine the mode 3 characteristics for each retaining wall.

Dock water level mode 3 quantification

As verification step to the results of the trim signal mode 3 analysis, the same type of analysis is performed on the water level measurements in the parking docks. The mode 3 effect has already been noted to be visible in these measurements (Duvivier & Nederend, 2013). This measurement is however not a direct measurement of the system, the water level oscillation in the parking docks are a side effect of the standing wave in the canal. Two main reasons for doing this additional analysis are identified:

- The water level measurements are possibly more sensitive to small mode 3 oscillations
- The data acquisition has gone through changes over the years, the dock water level gives a second measure of the mode 3 movement that can verify the consistency in the observations.

The analysis is done analogous to that of the trim angle, the appropriate threshold determined for this analysis is $1 \cdot 10^{-4} \text{ m}^2$. The results of the trim angle and dock water level analysis are compared in subsection 4.1.1.

3.6. Data visualisation

The three effects that occur during the high floating phase are non-stationary in time, this variation through time has been linked to changes in the hydraulic conditions in the waterway (section 2.2). To get an overview of the time dependent characteristics, a set of overview figures is created in which the time history of the seaward flow behaviour of the retaining walls and the hydraulic conditions are summarised per closure.

3.6.1. Overview of contents

In the figures, the various effects for different closures can be seen on the same vertical scale, to enable a comparison between different closure. The overviews can be split in a left and a right side, on the left side of each figure characteristics of the researched gate behaviour are given:

- **Trim angle** of the north and south retaining wall
- **Trim angle 2D power spectrum** of the north retaining wall
- **Mode 3 band variance** from the trim data (5-minute moving average)
- **Mystery force** as measured at the pull/push rod (5-minute moving average, for a limited subset of closures)

On the right side of the figures, variables regarding the hydraulic conditions are given:

- **Water level** on sea and river side of the barrier, and in the parking dock
- **Head difference** (5-minute moving average):
 - Sea minus river side water level (global head difference)
 - Dock minus river side water level
- **Vertical flow gap** under retaining wall
- **Discharge**:
 - 1D Numerical discharge calculation (for a limited subset of closures)
 - Discharge inferred from measured head difference

For part of the considered closures, the time history of the force in the pull/push rod and the computed discharge from the one-dimensional numerical model is not available for this study and is therefore not given in the overviews. To supplement the lack of information on the discharge, an estimation is made based on the vertical opening of the retaining wall and the observed global head difference with an adaption of Equation 2.1:

$$Q_{\Delta h} = B \cdot d \cdot \mu \cdot \sqrt{2g \cdot \Delta h_g} \quad (3.2)$$

In which:

- $B = 360$ m: waterway width (BMK, 1992c)
- d (m): retaining wall vertical flow gap, as measured at the north retaining wall
- μ (-): discharge coefficient related to the global head difference, assumed to be 1, roughly in line with model testing (WL|Delft Hydraulics, 1990b)
- $g = 9.81$ m/s²: gravitational constant
- Δh_g (m): global head difference, difference between measured sea and river side water level

Furthermore, the start and end of the observed mode 3 effect, based on the criteria found in section 3.3, is indicated using vertical black lines.

3.6.2. Resulting figures

The full set of figures is given in Appendix D. An example of a closure which shows the different seaward flow effects is the 2008 test closure, shown in Figure 3.10.

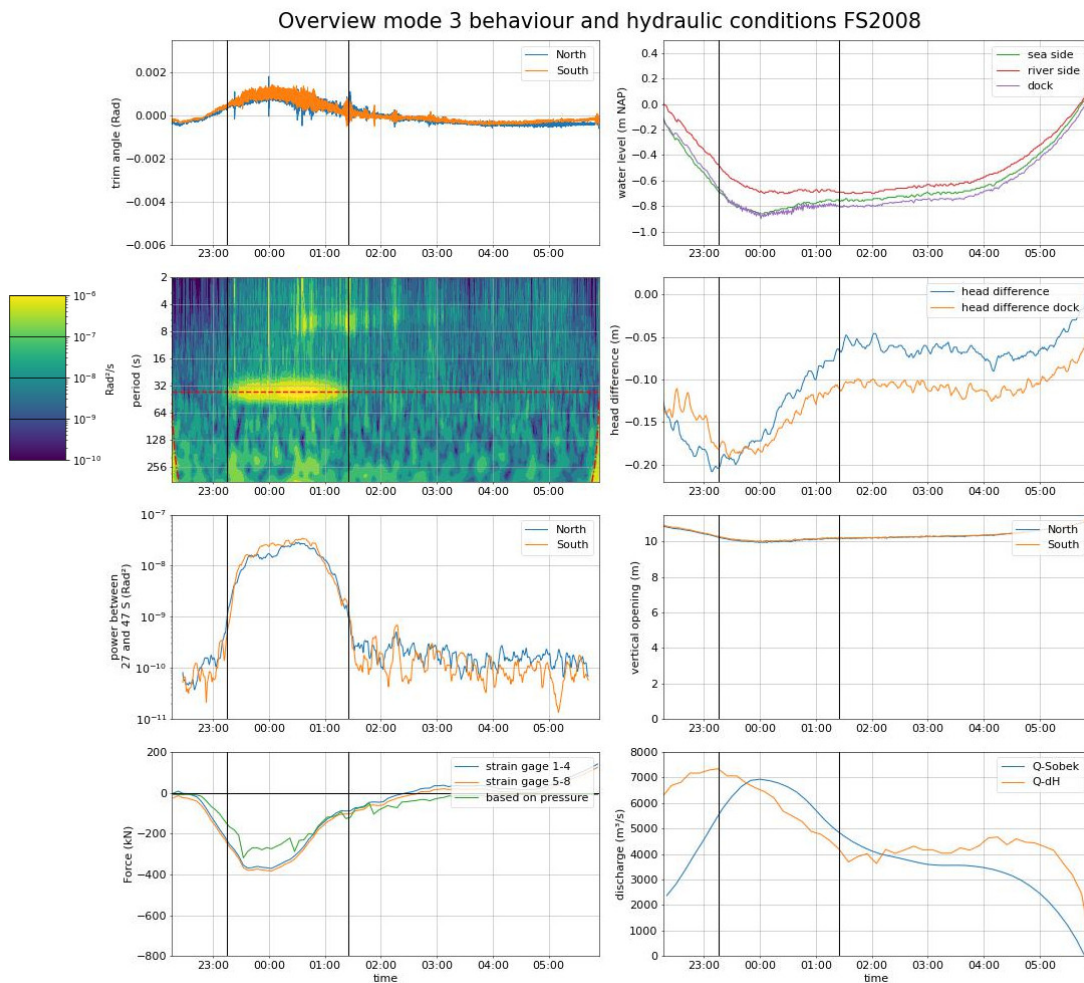


Figure 3.10: Overview of barrier behaviour and flow conditions during the 2008 test closure

An interpretation of interrelation between the effects and their relation with flow conditions is given in section 3.8, below two points regarding the data are given based on the visualization.

The overviews give further insight in the data quality of the different measures for the mystery force. It can be seen that the load calculated based on the observed pressure is lower than measured from the strain gauges. However, no constant relation between the two measures can be found, for the 2008 test closure the difference is relatively small, but for the 2009 test closure there is approximately a factor two difference (see Appendix D).

Regarding the discharge computed based on the observed head difference, two remarks may be made, based on a comparison of the closures for which also the discharge data from the numerical model is available. In terms of peak discharge, the simplified model seems to be a decent approximation. However, when the timing of this peak is considered a bigger deviation from the numerical model occurs, the cause of this could be sought in the fact the global head difference is observed at a considerable distance from the barrier (1.2 km between the sea and river side measurement locations, see Figure 3.3). Furthermore, the flow is not stationary, as can be seen from both the simplified and numerical model, considerable variations of the discharge occur during the first few hours of the high floating period.

3.7. Data quantification

From the data on possible influence factors a selection of quantities is made that represent the most important characteristics, these are mean and peak quantities as well as ranges. Choices are made based on the visualization in section 3.6. The Rhine discharge and wind speed are not considered in section 3.6, for these simply the mean value is considered. An overview is given in Table 3.2.

Data type:	Representative quantities:	Explanation:
Sea/river side water level	Level at start of gate de-ballasting	-
	Level at low water after gate de-ballasting	-
	Tidal range	Difference between observed high and low water. as found for the period between sinking of the retaining walls and 4 hours after de-ballasting.
	Water level change	Comparable to the tidal range, but with the high water level defined as the maximum water level during the de-ballasting phase of the retaining wall.
Global head difference (Seaside – River side water level)	Maximum value	Maximum head difference, occurs while the barrier is fully closed.
	Minimum value	Minimum head difference, occurs after the start of de-ballasting when the flow is in seaward direction.
Lobith discharge	Mean value	Mean of the discharge at Lobith over the 7 days before closure of the barrier.
Hoek van Holland wind conditions	Mean value	Mean wind speed as observed for the duration of the high floating phase.
Local discharge	Maximum value	Peak value of local discharge as computed by the numerical model

Table 3.2: quantities related to high floating phase conditions

The difference between the given tidal range and the water level change appears small, it could therefore be argued to only consider the tidal range. However, as will follow in later analysis, the two measures do not show a perfect correlation. More importantly, the water level change shows a better correlation with the seaward flow effects than the tidal range.

A reason for this could be that, since the water level change only considered the situation after the start of de-ballasting, it gives a better indication of the strength of flow during the high floating phase. This may relate to the observation that the start of the de-ballasting coincides with the change of sign of the head difference, and thus presumably with the change of flow direction (Figure 3.11). Furthermore, for some closures, a characteristic hump in the riverside water level can be seen at the start of the de-ballasting phase (see left figure in Figure 3.11). The given method takes this hump into account, which may be more relevant than the high water level during the closed phase.

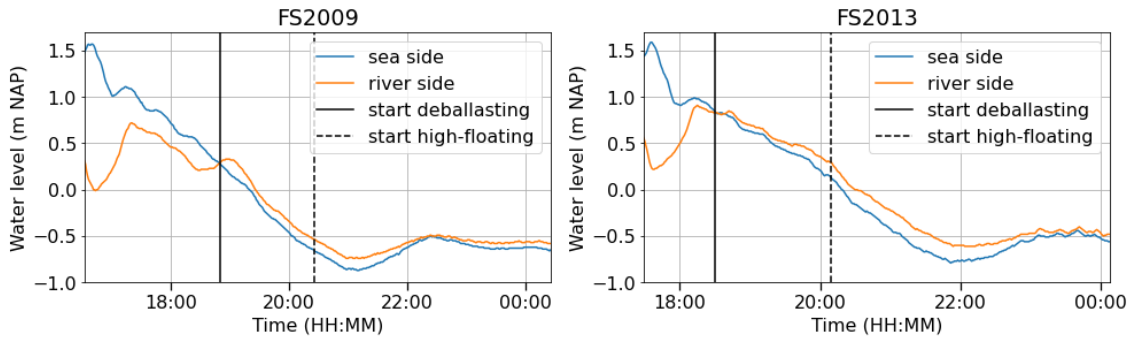


Figure 3.11: Sea and river side water level for the 2009 and 2013 test closure, time span from moment of full closure until 4 hours after fully de-ballasted

3.8. Summary

An overview of the seaward flow effects is given in Figure 3.12, based on the quantified effects during each closure. For the mode 3 effect the average over the different trim and parking dock signals is considered. The full results for the different effects are given in Appendix C, where it is also indicated for which closures full data on the mystery force are available, and where the maximum mystery force is obtained from reports.

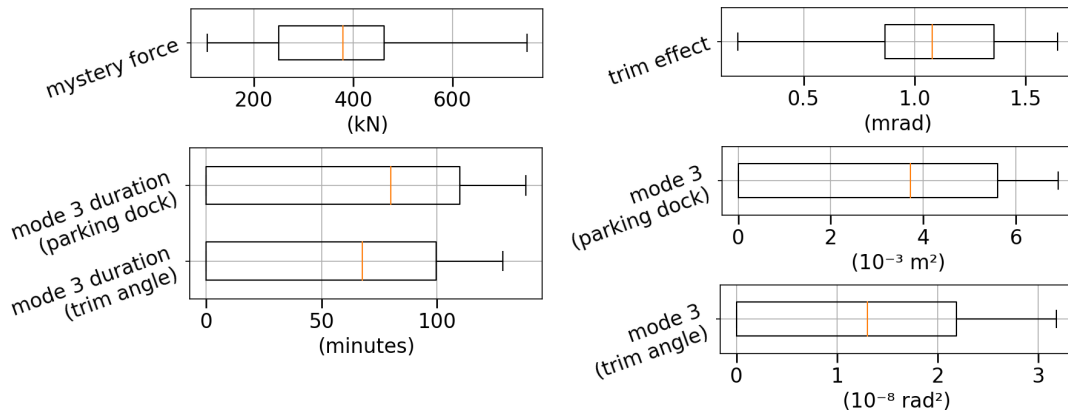


Figure 3.12: Boxplots of the identified seaward flow effects (off all considered closures), with the boxes indicating the range of the upper and lower quartile

Based on the visualized data, the following qualitative remarks on the occurrence of the seaward flow effects can be made:

- The three effects occur during roughly the same time period, during the first half of the high-floating phase when the local discharge is high, the mode 3 effect sometimes appears to reach its peak slightly later.
- The effects increase most significantly in magnitude when the water level and gate vertical opening decrease. Based on limited data, this also appears to be the period in which the discharge at the barrier increases.
- If the mode 3 behaviour occurs, it starts within 2 hours after the retaining walls are fully raised. This is the same period where the discharge at the barrier peaks.
- The mode 3 effect has a clear starting point, the other effects appear to built up more gradually

From the relation with the head difference and the change in water levels, it seems probable that the different types of behaviour are indeed related to flow conditions. Influence from factors not relating directly to the flow on the effects cannot fully be excluded, especially since these may indirectly impact the flow conditions.

An overview of the distribution of the quantities used to describe the conditions during the high floating phase (Table 3.2) is given in Figure 3.13.

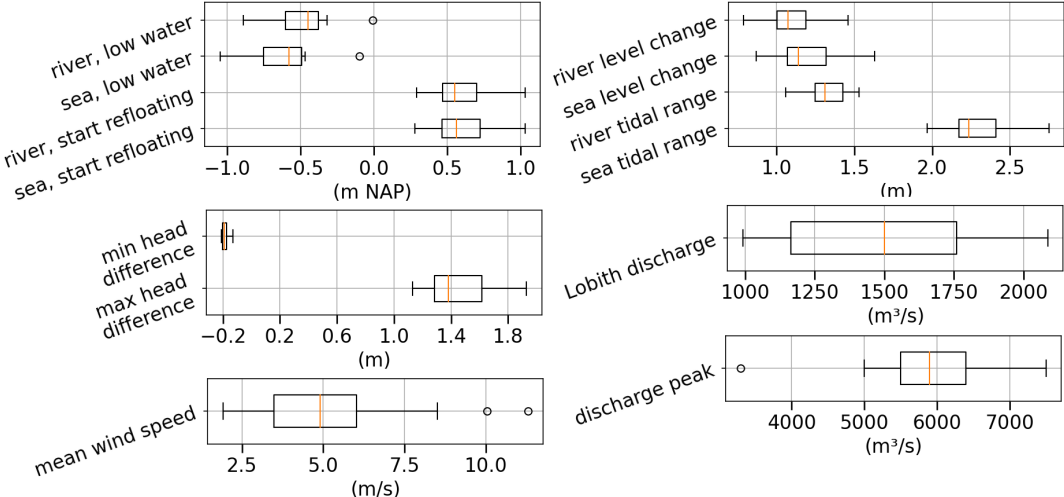
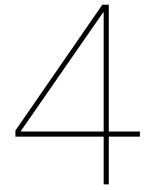


Figure 3.13: Boxplots of the quantities from Table 3.2 (off all considered closures), with the boxes indicating the range of the upper and lower quartile



Data analysis

In preceding chapters, the seaward flow effects considered in this report have been described, based on this relevant data has been collected from which the effects themselves and parameters relating to the hydraulic conditions have been quantified. The correlation between the different measures used for quantifying the seaward flow effects and statistical relations between the effects and parameters relating to hydraulic conditions are considered in this chapter.

4.1. Correlation between effects

4.1.1. Mode 3 regression

The correlation between the different measures for the mode 3 effect, obtained in subsection 3.5.3, is considered in this subsection. By testing the strength of the relations between the different quantities describing the mode 3 effect, it is assessed whether the magnitude is accurately derived. This is especially relevant for the mode 3 effect since a number of different signals are analysed of which the correspondence has not yet been quantified.

Used techniques are least-squares regression, scoring based on the coefficient of determination (R^2), and derivation of the uncertainty interval of the fitted slope parameter, these techniques are described in the textboxes below.

Least-squares regression

The best fit of the linear and non-linear relations in this report are based on the least-squares criterion, where the sum of the squares of the residuals (the observed values minus the predicted values of the fit) is at a minimum. The general criterion for a set of n observations is (Smith & Draper, 1998):

$$\sum_{i=1}^n (y_i - f(\vec{x}_i, \vec{\beta}))^2 \quad (4.1)$$

Where:

- y_i : observed dependent variable from realization i
- \vec{x}_i : set of observed independent variables from realization i
- $\vec{\beta}$: set of model parameters
- $f(\vec{x}_i, \vec{\beta})$: function describing the dependent variable as function of independent variables and model parameters

To perform this regression, different software packages are used for single (Scipy Community, 2022c) and multivariate (Scikit-learn, 2022) linear regression, as well as for non-linear regression (Scipy Community, 2022b). These functions all employ numerical methods to determine the model parameters that minimize the least squares solution.

Coefficient of determination

To compare the quality of the different relations, the *coefficient of determination* is used as a measure. The coefficient of determination or R^2 -score gives a measure of the amount of variance in the set of realizations that can be explained using the assumed statistical relation.

R^2 is determined with (Smith & Draper, 1998):

$$R^2 = 1 - \frac{\sum_{i=1}^n (f(\vec{x}_i, \vec{\beta}) - y_i)^2}{\sum_{i=1}^n (y_i - \bar{y})^2} \quad (4.2)$$

With variables defined as in Equation 4.1, and:

- \bar{y} : the mean of the set of dependent variables

From this definition, it follows that R^2 is negative in the case that:

$$\sum_{i=1}^n (f(\vec{x}_i, \vec{\beta}) - y_i)^2 > \sum_{i=1}^n (y_i - \bar{y})^2 \quad (4.3)$$

This distinguishes the coefficient of determination from the correlation coefficient squared, which never yields a negative value.

Fitted parameter uncertainty

For the estimated slope parameter, a confidence interval can be constructed based on the standard error of the estimated slope and an assumed t -distribution of the estimated slope parameter (Scipy Community, 2022c; Smith & Draper, 1998).

For single linear regression, with both an estimated slope and intercept, the appropriate t -distribution has $n - 2$ degrees of freedom, where n is the number of samples (Smith & Draper, 1998). The confidence interval for the estimated slope is:

$$\hat{\beta} - s_{\hat{\beta}} \cdot t_{\text{dof},5\%} > \beta < \hat{\beta} + s_{\hat{\beta}} \cdot t_{\text{dof},95\%} \quad (4.4)$$

With $s_{\hat{\beta}}$ indicating the standard error of the estimated slope, which is an output of the used regression functions, and $t_{\text{dof},\alpha}$ indicating the critical values of the appropriate t -distribution. In this report, the 90% confidence interval is considered for the slope parameter.

North and south retaining wall mode 3

First, the correspondence between the mode 3 effect at the north and south retaining wall is considered. Since the mode 3 mechanism requires both retaining walls to participate (section 2.5) a high correlation between the results for the north and south retaining wall is expected. Since both retaining walls are required to participate, the intercept for this analysis is fixed at 0.

In Figure 4.1 the relation between the north and south retaining wall is shown for the peak variance and duration of the mode 3 effect during the considered closures.

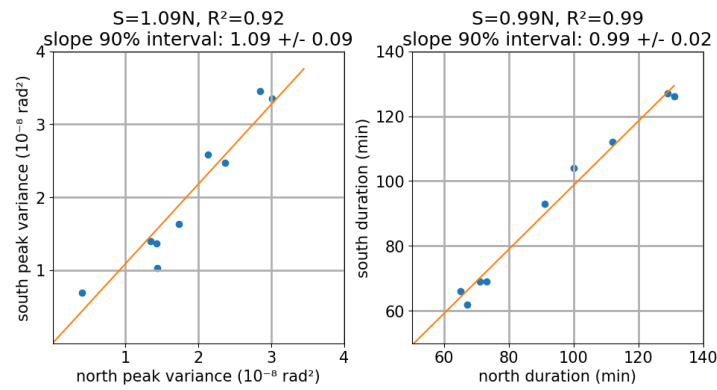


Figure 4.1: Correlation between mode 3 results for the north and south retaining wall

From Figure 4.1 it follows that the north and south retaining wall results show high correlation for the mode 3 effect. The correlation for the peak variance is slightly lower than for the duration. The south retaining wall appears to exhibit a slightly bigger mode 3 effect compared to the north retaining wall, shown by a slope of 1.09, with a lower bound of the confidence interval of 1.00.

Based on the correspondence found for the mode 3 effect between the north and south wall, further analyses will use the mean of the peak variance and duration over the north and south retaining walls.

Parking dock water level mode 3

In Figure 4.2 the results from the trim angle mode 3 and dock water level mode 3 are compared. There is strong correlation between the trim and dock water level results, with R^2 values of 0.95 and 0.98.

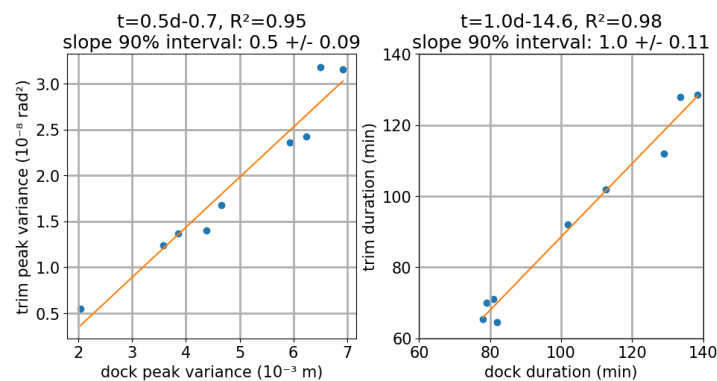


Figure 4.2: Correlation between trim mode 3 compared to dock water level mode 3

It seems intuitive to expect a one-on-one relation between the amplitude of the effect in the dock water level and the retaining wall trim angle. This largely matches the observations in Figure 4.2. However, the dock water level, as mentioned, provides an indirect observation of the effect. A lower gate position, induced by low water levels, may, for example, shield the parking dock significantly more from the main waterway. This may reduce the effect as observed in the parking dock, this aspect is not considered further in this study, as the high correlation between the trim and parking dock results suggest no big influence of such effects.

4.1.2. Effects regression

Linear regression between the different effects is considered in Figure 4.3. For the mystery force, the data is given in different colours to indicate the different data sources (as treated in section 3.2). The reason for this is that the differences in reporting may play a role in the found magnitude of the mystery force.

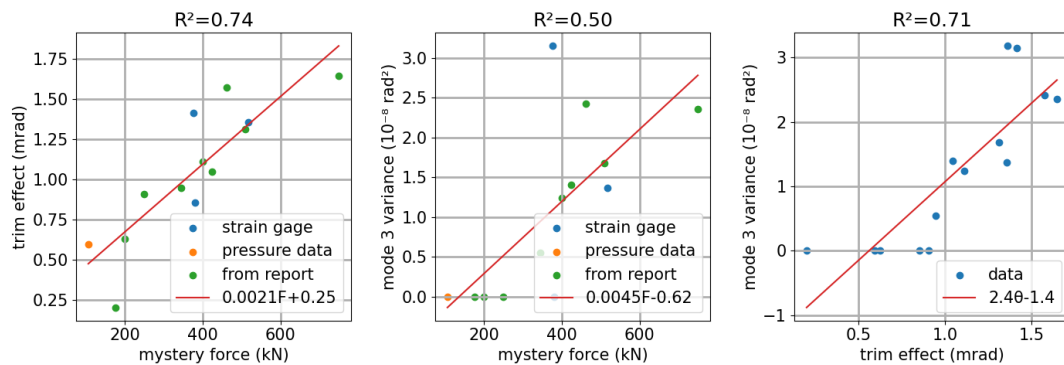


Figure 4.3: Linear correlation between the considered effects (mode 3 variance as observed in the trim signals)

In Figure 4.3 the correlation between the magnitude of the effect becomes apparent, with R^2 -scores in the range 0.50-0.74. The figure shows that for some closures, a mystery force and trim effect are observed without a mode 3 effect. This may indicate that the mode 3 effect requires conditions to exceed a certain threshold, while this does not appear to be the case for the other two effects.

4.2. Load correlation

A first step towards quantifying relevant influence factors for the seaward flow behaviour is given by considering three variables that can directly or indirectly impact the load on the retaining wall:

1. **Global head difference:** The head difference over the barrier is a measure of the hydrostatic load on the barrier, it has also been identified in the design phase as a factor that determines the retaining wall's dynamic stability.
2. **Lobith discharge:** The discharge locally at the barrier is influenced by the tide, but also by the river discharge. As a first estimate for the influence from the river discharge, the Rhine discharge at Lobith may be considered.
3. **Wind conditions:** In the floating state, the retaining wall is loaded by wind. Wind conditions also impact the hydraulic conditions, for example by causing a set-up at the seaside of the waterway.

Head difference

The head difference is the global head difference determined from the sea and river side water level stations (subsection 3.3.2). During the high floating phase, a peak negative the head difference occurs, as noted in Table 3.2. This peak is used as measure for the hydrostatic load due to the head difference. In Figure 4.4 linear regression between the head difference peak and the three seaward flow effects is investigated.

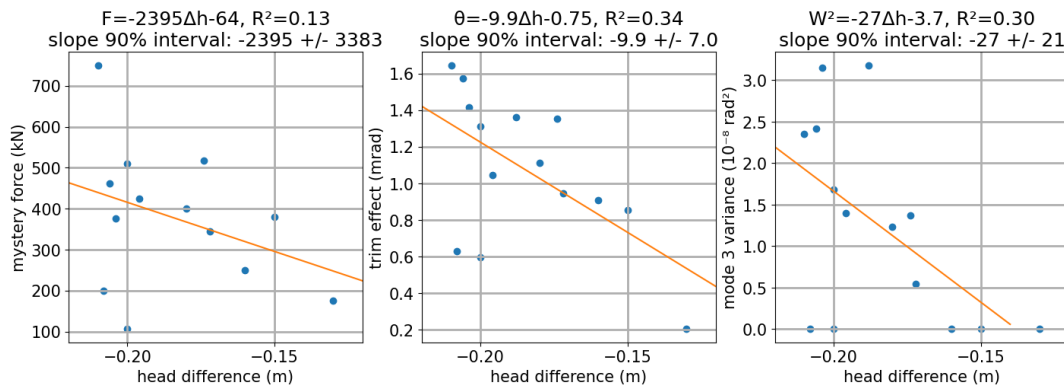


Figure 4.4: Linear correlation of negative head difference and the seaward flow effects

From Figure 4.4 it can be seen that the correlation for all effects is weak, especially for the mystery force. This can be seen from the low R^2 -scores and big intervals for the estimated slope parameters. This may be because only a narrow range of head differences (-0.21 m to -0.13 m) is present in the data.

Lobith discharge

As a preliminary estimate for the influence from the river discharge, the Rhine discharge at Lobith may be considered. The discharge used in this for this analysis is the mean of the discharge at Lobith for the week leading up to the closure (Table 3.2). During all considered closures, the discharge at Lobith was limited, 2,200 m^3/s or lower, while at peaks the discharge at Lobith may reach values in excess of 8,000 m^3/s . Figure 4.5 gives the linear relation between the Lobith discharge and the seaward flow effects.

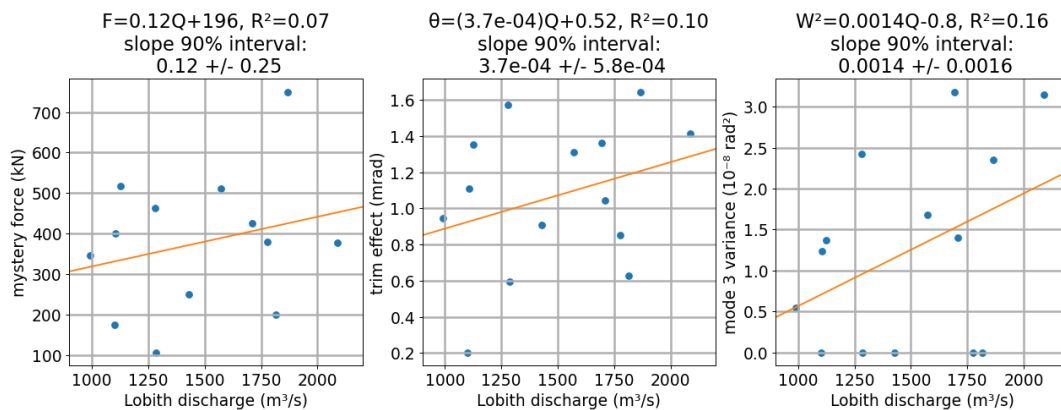


Figure 4.5: Linear correlation of Lobith discharge and the seaward flow effects

The relations in Figure 4.5 are very weak, the discharge at Lobith seems to have no predictive value for the different effects. A reason for this could be that the local discharge at the barrier is dominated by tidal effects. This may also be connected to the limited discharge range considered, it seems probable that for a more extreme Rhine discharge the influence of the Rhine discharge on the hydraulic conditions at the barrier increases.

Wind conditions

To consider the relation with the wind conditions, the mean of the different wind related variables during the high floating phase are considered. This results in three different quantities per closure:

- Mean wind speed
- Mean of the maximum wind gust measured per 10 minute interval
- Mean wind direction (taking into account that the wind direction is a cyclic quantity)

A linear correlation analysis of each of these variables is performed. For neither variables strong relations are found, for this reason only the relation with the mean wind speed is given in Figure 4.6. The lack of relation is shown by the R^2 -scores that are close to 0 and the confidence intervals for the slope parameters.

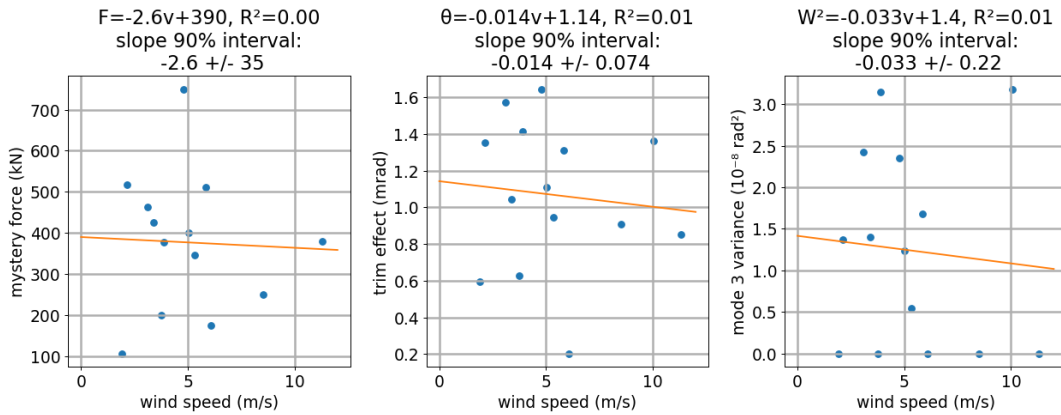


Figure 4.6: Linear correlation of Hoek van Holland mean wind speed and the seaward flow effects

4.3. Correlation matrix

To get a more thorough overview of the correlations that are present in the available data, a correlation matrix is created based on the quantified effects and hydraulic conditions. The textbox below gives a short description of the theory behind the correlation matrix.

correlation matrix

A correlation matrix is a square matrix in which every cell gives information on the correlation between the two variables on the vertical and horizontal axis.

To assess the correlation in this thesis, an approach based on Spearman's rank correlation coefficient is used. For the case where all ranks are distinct integers, Spearman's coefficient between two variables (X, Y) is determined using (Gauthier, 2001):

$$r_s = 1 - \frac{6 \sum_{i=1}^n (R(X_i) - R(Y_i))^2}{n(n^2 - 1)} \quad (4.5)$$

With:

- $R(X_i)$ the rank of X_i in the set X .
- $R(Y_i)$ the rank of Y_i in the set Y .
- n : size of the dataset

The reason for using rank correlation is that this not only accounts for linear regression, but for all monotonically increasing or decreasing relations. Furthermore, the rank basis makes Spearman's coefficient less sensitive to outliers in the data (Gauthier, 2001).

The diagonal cells in the correlation matrix must by definition be equal to one, a variable by definition has perfect correlation with itself. For all other cells, the values of the cells are between -1 (perfect negative rank correlation) and 1 (perfect positive rank correlation). In this report, negative correlation is indicated in red tones and positive correlation in blue tones.

In the correlation matrix, the quantities describing the seaward flow behaviour are the quantities collected in section 3.5. Regarding possible influence factors, the extracted quantities described in Table 3.2 are considered. In Figure 4.7 part of the correlation matrix is given, only the part that is needed to assess the correlations that relate to the seaward flow effects is given. The full correlation matrix, with all interrelations, is given in Appendix E.

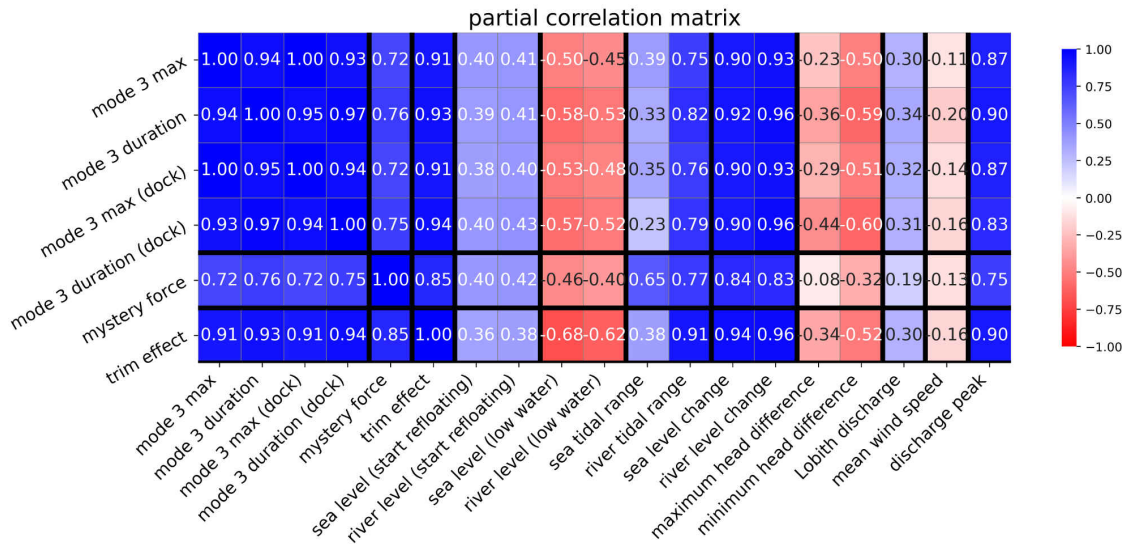


Figure 4.7: Top part of the constructed correlation matrix

From Figure 4.7 it can be seen the different seaward flow effects show a high rank correlation with each other, as expected from the linear regression analyses in subsection 4.1.2. Furthermore, strong relations between these effects and several flow related variables can be seen. The strongest relation is found for the parameter named *river level change*, the water level change on the inland side of the barrier after the barrier is being de-ballasted. Based on this observation, the next section analyses statistical relations based on this parameter.

4.4. River level change regression

The results of a linear regression analysis for the three effects are given in Figure 4.8.

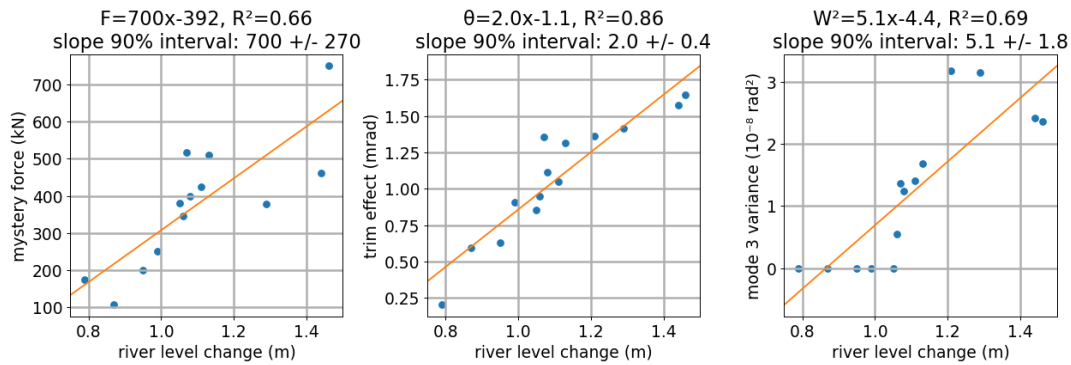


Figure 4.8: Linear correlation of river side water level change and the seaward flow effects

For the relation found for the mystery force the spread is significant, however visually there is no indication for models which give a more appropriate relation. Regarding the trim angle effect, the linear regression models the effect well. For the mode 3 effect, the linear regression model does not appear to be the most appropriate. The mode 3 effect seems to only occur above a threshold value for the river level range. Furthermore, from the limited data, the mode 3 amplitude seem to reach a plateau for increasing values of the river level change.

4.4.1. Mode 3 non-linear regression

Based on the observed relation between the river level change and the mode 3 effect an exponential and a parabolic fit is performed for the selection of the dataset where the mode 3 effect is observed, considered are the magnitude found in the trim angle and parking dock water level. An exponential function of the following form is used:

$$W^2 = \beta_0 \exp(\beta_1 \cdot x) + \beta_2 \quad (4.6)$$

The considered parabolic fit has the form:

$$W^2 = \beta_0 x^2 + \beta_1 x + \beta_2 \quad (4.7)$$

The threshold selection is based on the observations from Figure 4.8, only the data where the river level change parameter exceeds 1 meter are included for the two fits. The results are shown in Figure 4.9.

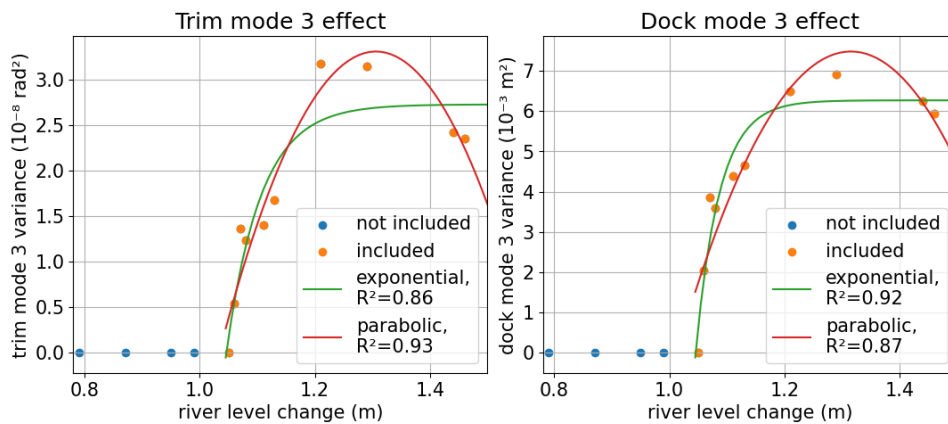


Figure 4.9: Exponential and parabolic fit for the mode 3 effect to the river level change

from the R^2 -scores, it follows that these fits are better than linear regression (Figure 4.8). For the mode 3 variance in the trim angle signal the parabolic fit performs best, for the effect in the dock water level the exponential fit. No decisive conclusions can be drawn from this, the amount of data points for values of the independent parameter is too limited. However, both fits indicate that the mode 3 magnitude is limited in some way. The parabolic fit even suggests that the mode 3 effect decreases after a local maximum of 1.3 meters of water level change, this follows mainly from two data points, conclusions should not be drawn on this. For this reason, the exponential fit is considered the most relevant modelling choice, as long as no data for more extreme situations is available.

For the part of the dataset where the threshold is not exceeded, the expected mode 3 variance is assumed at 0. An alternative to this could be a logistic curve, which has a shape similar to an S-curve, and can, therefore, be used for the full dataset.

4.4.2. Mode 3 multiple regression

To check if any of the variables from the correlation matrix can be added to the exponential model to obtain an even better model, the linear correlation between the residuals of the exponential fits in Figure 4.9 and the correlation matrix variables is considered.

Only for the effect observed in the parking dock, this analysis yielded improvement. Between the water level at the start of the floating phase and the residuals, some correlation seems present (Figure 4.10). It appears the model underestimates the effect for situations with low water levels and overestimates for high water levels.

Based on this, a multiple linear regression analysis is done. The earlier found relation with the water level change is exponential, the linear model takes the effect of the riverside water level change into account using the exponential factor found in the nonlinear model:

$$W^2 = \beta_0 \exp(\hat{\beta}_1 \cdot x_1) + \beta_2 x_2 + \beta_3 \quad (4.8)$$

With:

- x_1 (m): river level change
- x_2 (m NAP): water level at start of de-ballasting relative to NAP
- $\hat{\beta}_1$: regression parameter as estimated in Figure 4.9

By using the factor $\hat{\beta}_1$, from the nonlinear regression in this relation, the system can be solved using methods for multiple linear regression. However, it will not yield the optimal solution, to obtain the optimal solution a nonlinear model must be used that also determines β_1 . In Figure 4.11 the result for the used linear model is shown. Because this model depends on two variables, a new representation is used for this figure, treated in the textbox on the bottom of the page.

The R^2 -score is slightly improved compared to the single regression model. This, however, does not necessarily indicate that the model is significantly better. A model with an added parameter will always score the same or higher R^2 -score compared to the original model, and the improvement is only small. The multiple regression relation was not found for the effect quantified from the trim angle signal, further reducing the value of the multiple regression model.

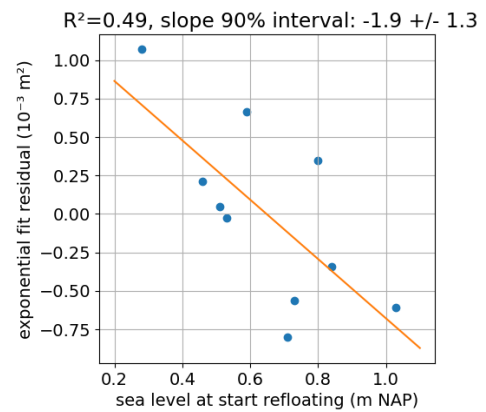


Figure 4.10: Linear correlation of mode 3 exponential fit residuals and the start water level

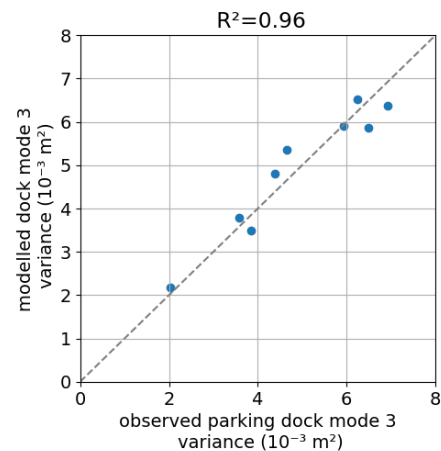


Figure 4.11: Multiple regression fit to mode 3 maximum variance

observed best fit comparison scatter plot

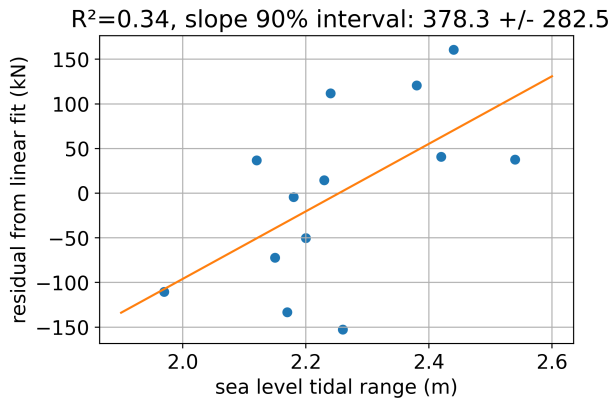
To give a visual representation of models that contain multiple dependent variables, a different type of scatter plot is introduced. In this plot, the observed value of the effect is given on the horizontal axis and the modelled value resulting from the multivariate model on the vertical axis.

In this type of plot a perfect model, one that predicts all observed values correctly, will have all its data points on the diagonal $y = x$. An imperfect model will have its data points deviating from this diagonal. To make these deviations clearer in the given plots, the diagonal $y = x$ is drawn as reference in grey.

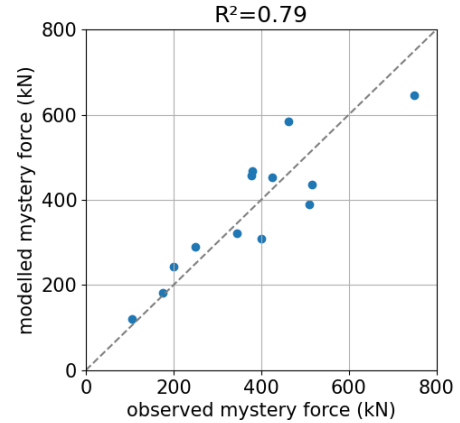
4.4.3. Mystery force multiple regression

For the residual from the linear model for the mystery force, no very strong relations seem present. The tidal range on the seaside shows some linear correlation, but the spread is big, as can be seen in Figure 4.12a.

A multiple linear model is fitted with river side water level change and seaside tidal range as independent variables. The results of this fit are shown in Figure 4.12b. The R^2 -score for this multiple fit is 0.79, this is higher than the R^2 -score of the single-variate fit (0.66).



(a) Linear correlation of mystery force uni-variate fit residuals and the seaside tidal range



(b) Multiple regression fit to mystery force

Figure 4.12: Mystery force multiple regression results

4.4.4. Trim effect multiple regression

For the residual from the linear model for the trim angle effect, no relevant relations seem present. The found relations are very weak, with $R^2=0.05$ for the strongest relations, the tidal range on the seaside of the barrier. Multiple linear regression analysis yields no improvement of the single regression model, and the results are therefore not given.

4.5. Empirical models

Earlier investigation put forward relations relating to the cube or square of the local discharge for the mystery force (Duvivier & Nederend, 2013). For these relations limited physical reasoning is present, the relations are mainly based on the observation that the discharge and mystery force follow a similar profile through time. This notion is combined with the expectation that the hydrostatic load on the retaining walls scales with the local head difference, which is expected to scale with the discharge squared (Equation 2.1). Considered in this section, are the squared and cubed relations with the peak local discharge, as well as a linear relation with the peak local discharge. This analysis is done for all three considered effects.

The effects possibly only occur above a threshold discharge, an empirically derived parameter could be added to the model to compensate for this. Earlier a threshold of 4,200 m^3/s was suggested for the mystery (Duvivier & Nederend, 2013), however during the 2020 test closure a mystery force was present at a peak discharge of 3,300 m^3/s . Limited information on applicable thresholds for the different effects exists, to take this into account the regression models are considered with and without intercept parameter.

4.5.1. Model definition

The different models for the effects are summarized in Table 4.1. With β_1 as slope and β_2 as intercept, describing the modelled magnitude of the effect at a local discharge of 0 m³/s.

Model description	no intercept	including intercept
Linear	$\beta_1 \cdot Q^1$	$\beta_1 \cdot Q^1 + \beta_2$
Squared	$\beta_1 \cdot Q^2$	$\beta_1 \cdot Q^2 + \beta_2$
Cube	$\beta_1 \cdot Q^3$	$\beta_1 \cdot Q^3 + \beta_2$

Table 4.1: Empirical discharge models

4.5.2. Model fit

The models in Table 4.1 are fit using the peak discharge at the barrier, as described in section 3.2. This is the local discharge at the barrier computed with the numerical model. Regarding the observed mystery force, the one closure with mystery force data based only on observed hydraulic pressure in the movement mechanics (see section 3.2) is disregarded since its correspondence to the other measures is uncertain. Fitted parameters and corresponding confidence intervals are given in Appendix F (confidence interval obtained with Equation 4.4).

Mystery force

The results for the mystery force are shown in Figure 4.13. In terms of R²-score, the square and cube models appear better than the linear models. Furthermore, the model for the discharge squared including an intercept is very similar to the model without intercept. This appears to support the scaling with the head difference, as the head difference is 0 if the discharge is 0. It can be expected that the discharge cubed model will give significantly higher forces for high discharges. However, no reason can be seen based on the models to give preference to this model.

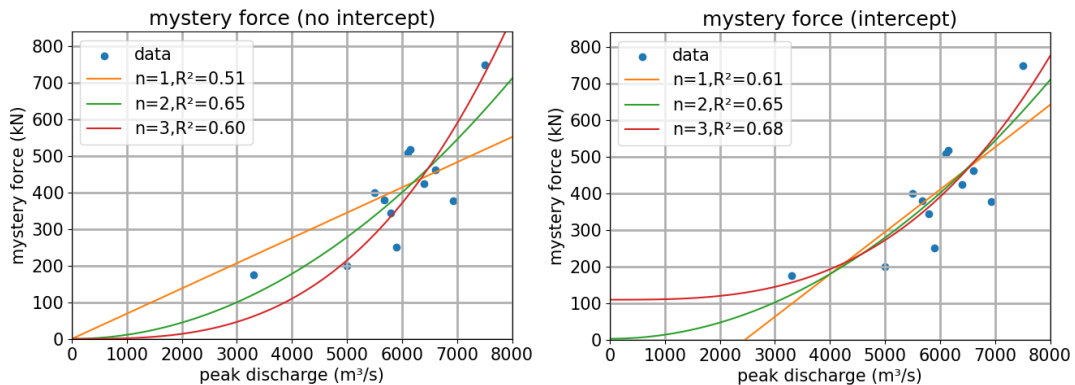


Figure 4.13: Mystery force empirical models

Trim effect

For the trim angle effect, results are given in Figure 4.14. For the models without intercept the squared model gives the strongest relation, for the models with an intercept the differences in R²-score are small. The notion that the intercept for the squared model is relatively small, again leads to the suggestion that the relation with the discharge squared is the most relevant, possibly suggesting a relation with the head difference.

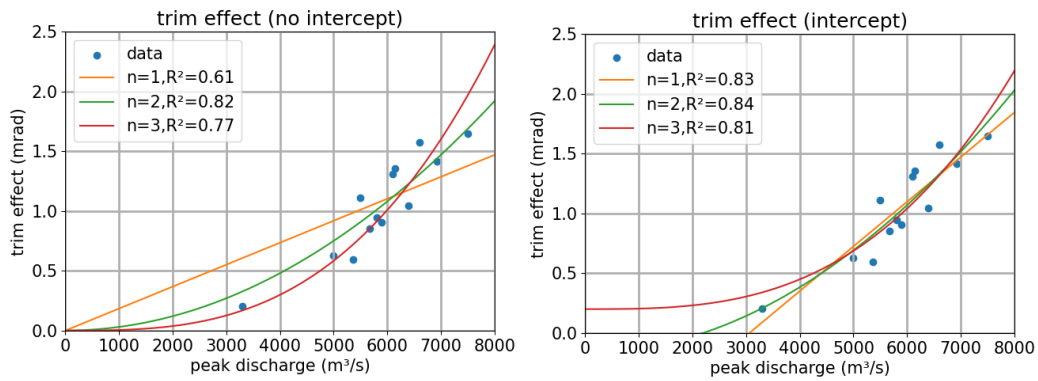


Figure 4.14: Trim angle effect empirical models

Mode 3 effect

For the mode 3 effect, results are given in Figure 4.15. Neither the models with or without intercept model the mode 3 magnitude well. Especially, the observations without the mode 3 effect are not modelled well in Figure 4.15. No conclusive relations with the local discharge are drawn from Figure 4.15.

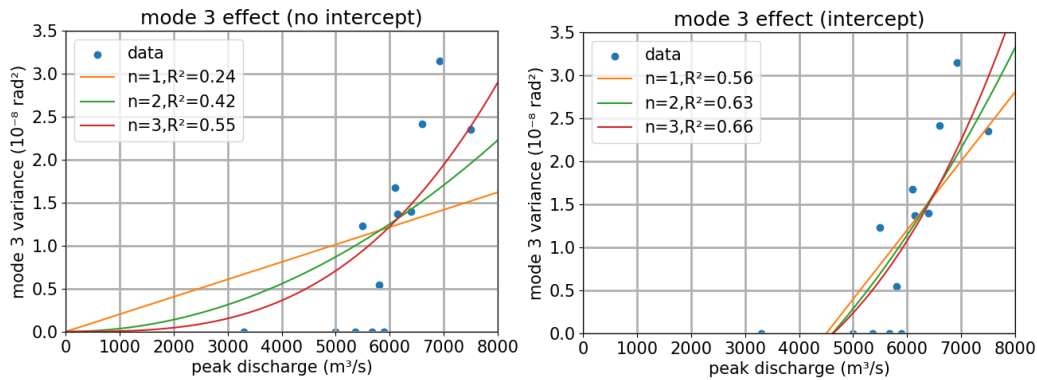


Figure 4.15: Mode 3 effect empirical models

4.6. Summary

In section 4.1 it has been demonstrated that the different measures for the mode 3 effect show strong correlation ($R^2=0.92-0.99$). Between the different seaward flow effects, linear correlation was present as well, but less strong ($R^2=0.50-0.71$). The mode 3 effect not occurring for all closures appears to play a role in the lower linear correlation between the effects.

From section 4.2 some possible parameters, relevant for loading of the retaining wall, are considered (observed head difference, Rhine discharge, wind speed). Only weak relations are found ($R^2=0.00-0.34$). This leads to the adoption of the correlation matrix in section 4.3, which identifies relations between the seaward flow effects and parameters related to hydraulic conditions. This approach uses rank correlation, which identifies both linear and non-linear relations.

In section 4.4 the strongest statistical relations from the correlation matrix are considered, the relations with the *river level change* parameter (parameter described in Table 3.2). This leads to linear relations for the mystery force and trim effect ($R^2=0.66, 0.86$). For the mode 3 effect, non-linear relations with a limited plateau and a threshold value are considered ($R^2=0.86-0.93$).

Multiple regression models are proposed for the different effects, which yield limited improvement, theoretical reasoning supporting these additions lacks. For the single regression model the relation with increasing flow is clear, but for the added parameter it is unclear how it improves the description of the hydraulic conditions.

Empirical relations between the peak local discharge and the seaward flow effects are considered in section 4.5. From this a relation with the discharge squared, which implies a relation with the head difference, see Equation 2.1, follows for the mystery force and the trim effect ($R^2=0.65, 0.82$). In terms of R^2 -score, the cubed and linear model scores similarly, but their relation with the underlying physics is less clear. Furthermore, the squared models for the mystery force and trim effect predict a magnitude close to zero for a zero discharge, as expected for a relation with the head difference. The R^2 -scores are slightly lower than for the statistical relations that follow from the correlation matrix.

Regarding the mode 3 effect the different empirical models with the local discharge appear less relevant, the found R^2 -scores of 0.63 and below are lower than found in the non-linear analysis. However, further analysis of the relations with the discharge may be relevant, as the plateau as found in the non-linear analysis appears less clear in the scatter plot with the local discharge. This may suggest that higher mode 3 amplitudes are in fact not ruled out.

5

Conceptual models

In this chapter conceptual models are developed to support the findings from chapter 4, the established relations with hydraulic conditions, and the correlation between the different seaward flow effects, using conceptual models supported with physical arguments. Distinct conceptual models are given for the three different seaward flow effects from section 1.2:

- Mystery force
- Trim angle effect
- Mode 3 effect

First, the basis for the considered effects and their presumed interrelation are described. From this, conceptual models are detailed and defined for the different effects individually.

5.1. Behaviour description

The conceptual models for the mystery force follow from a moment balance around the ball joint (see Figure 5.1). Tangential loading components can be seen to induce a moment around the ball joint (tangential load 1 and 2 in Figure 5.1). The gate is fixed in its position and this loading is compensated by a force through the pull/push rod (the observed mystery force), which gives a moment of the same magnitude in the opposite direction (see also section 2.1). For both the load on the gate and the reaction from the pull/push rod the arm around the ball joint is approximately the same, this reduces the moment balance to a force balance, the *tangential force balance*:

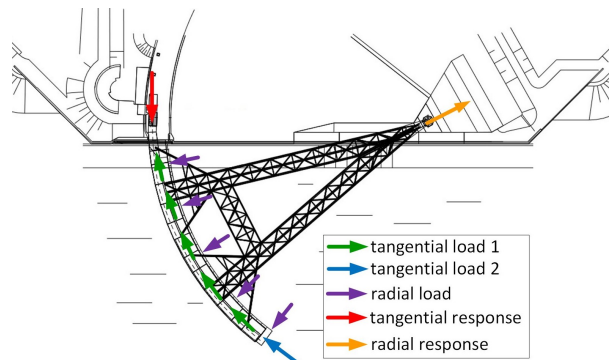


Figure 5.1: Proposed load components that may contribute to the mystery force, image from Koninklijke PBNA, n.d.-c

$$\sum F_{\text{tangential}} = 0 \rightarrow F_{MF} = \sum F_{r,i} \quad (5.1)$$

Where:

- F_{MF} (kN): the response from the pull push rod on the retaining wall, the observed mystery force.
- $F_{r,i}$ (kN): the tangential load components on the retaining wall (as illustrated in Figure 5.1)

As illustrated in Figure 5.1 neither the radial component of the load nor the response from the ball joint plays a role in the moment balance around the ball joint.

From observations (section 2.3), the data visualization (section 3.6), and the statistical relations (section 4.4), it follows that the tangential load is likely induced by effects related to the flow conditions. To explain the observed mystery force, the models consider different tangential load contributions that may follow from seaward flow.

By definition, only limited ballast water is present in the retaining wall during the high floating phase, consequently only the bottom part of the retaining wall is submerged. It is therefore expected that the tangential load, due to flow, on the retaining wall is induced somewhere on the bottom half of the retaining wall. The pull/push rod, however, is connected to the top of the retaining wall (section 2.1). This leads to loading of the retaining wall, as illustrated in Figure 5.2.

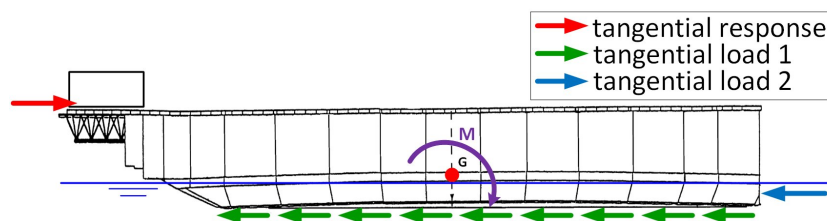


Figure 5.2: Vertical position of loads that may contribute to the mystery force in front view of retaining wall, base image from Koninklijke PBNA, n.d.-a

The connection of the retaining walls to the ball joint can be expected to facilitate rotation around the centre of the front view of the retaining wall (section 2.1). This is also schematized to be the location of the retaining wall's centre of gravity (G in Figure 5.2), since it is expected to be in the centre of the retaining wall front view (assuming even distribution of mass). The location of the centre of gravity in the vertical is unknown, and the vertical position in Figure 5.2 is indicative.

Due to the position of the tangential forces, a moment is generated (Figure 5.2). A change of the trim angle is expected, such that hydrostatic pressures compensates the loading due to the tangential load (Figure 5.3). This establishes a possible link between the mystery force and the trim effect. The trim angle model quantifies the moment induced by the mystery force and the resistance of the retaining wall against this load through the effect of the changed hydrostatic pressure distribution.

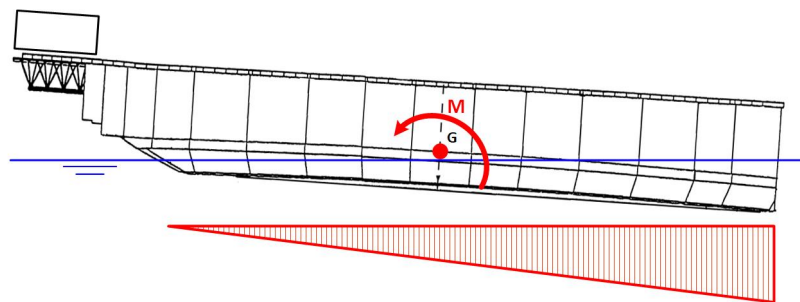


Figure 5.3: Indicative hydrostatic pressure distribution due to trim and resulting moment, base image from Koninklijke PBNA, n.d.-a

Other factors may also contribute to the moment, M , as indicated in Figure 5.3, such as remaining ballast water in the trim tanks. However, since only the relative trim increase during the period with a high seaward discharge is considered for the quantified trim effect (subsection 3.5.2), factors that are expected to be constant are not considered in the conceptual models. Flow related contributions to the moment, M , other than due to the mystery force, may be relevant. These effects may contribute since they are not constant for the considered period, but change with flow conditions.

The mode 3 model considers interaction between the retaining wall trim and the water level downstream of the barrier (BMK, 1992c). The downstream water level is influenced by the discharge from upstream, and through this by the retaining wall trim (BMK, 1992c).

For a change in the vertical flow gap over the channel cross-section (Figure 5.4), the discharge from the retaining wall varies over the cross-section (as follows from Equation 2.1). The water level, which due to the discharge variation varies along the cross-section, in turn influences the trim of the retaining wall through hydrostatic loading.

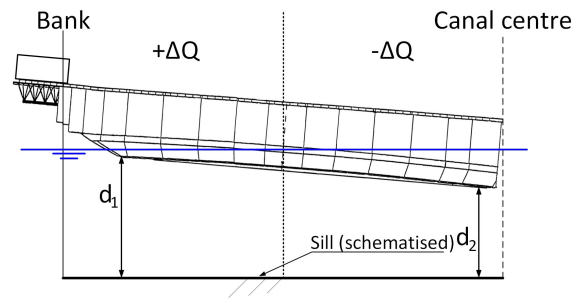


Figure 5.4: Cross-sectional variation of the flow gap along the retaining wall under an exaggerated trim angle, base image from Koninklijke PBNA, n.d.-a

Flows over the canal cross-section (induced by water level variation over the cross-section) play a role in the periodicity of the mode 3 effect, an effect similar to a standing wave is observed between the banks of the waterway (Kolkman & Jongeling, 2007). For the mode 3 effect to be noticeable the wave should be amplified by the discharge variations due to the retaining wall movement, such that a significant wave builds up downstream of the barrier, which in turn further excites the retaining walls. These cross-sectional flows, along with the movement of the retaining wall trim, have not been explicitly modelled in the design-phase models.

The trim effect is associated with similar deviations in the discharge over the channel cross-section, since the doors make a move in the same degree of freedom. An increase of this variation during the build up of the trim effect may suggest a relation between the mode 3 effect and the trim effect.

5.2. Mystery force

5.2.1. Description

The conceptual mystery force models use the tangential force balance as basis (Equation 5.1). In the models, different possible contributions to the tangential load on the retaining wall are considered. Inertia effects related to the mystery force are neglected, since the force appears to build up slowly relative to the eigenperiod of horizontal retaining wall movement (order 1 hour compared to an expected eigenperiod of 30-90 seconds, as estimated in Appendix G).

In this analysis, the effects are split in two components. Two models, indicated with B1 and B2, are considered for the load on the short sides of the retaining wall (load 2 in Figure 5.1):

- (B1) Hydrostatic approach
- (B2) Momentum balance approach

Two possible contributions along the bottom of the retaining wall, indicated with C1 and C2, are considered (load 1 in Figure 5.1):

- (C1) Load due to a water level variation over the cross-section
- (C2) Load due to the trim angle in combination with a suction force

As basis for the mystery force models, it is hypothesized that a tangential load on the short side must be present. Reasoning for this is as follows, a barrier, weir, or any other structure that (partly) blocks flow, is loaded by this flow. This load is distributed over the structure. From the geometry of the Maeslant barrier (Figure 5.1) it can be expected that part of this load acts on the short side of the retaining wall in the middle of the waterway. Based on this reasoning, the B-type models are used as a basis for the predictions on the mystery force. The C-type models are consequently added as additional effects, to test if these additions improve model predictions.

(B1) Hydrostatic approach

This hypothesis has been formulated earlier (Bakker, 2008), and considers a net tangential load caused by the head difference acting over the short sides of the retaining walls.

It is assumed that the head difference over the barrier also is present over the short sides of the retaining wall. In Figure 5.5 this is indicated by assuming a hydrostatic load on the riverside, p_r , due to the water level on the riverside h_r , and a hydrostatic load in the parking dock, p_s , due to the seaside water level h_s . The pressure difference between the two gives rise to the tangential load. The variable in this model is the difference in water level over the sea and river side of the barrier that gives rise to this difference in pressure (the local head difference). The force follows from the area of the retaining wall short side and the local head difference that is the basis for the pressure difference.

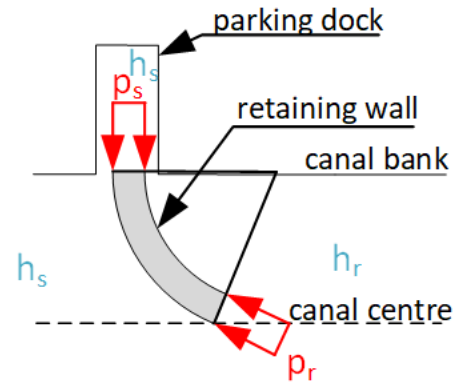


Figure 5.5: Tangential load from hydrostatic schematization

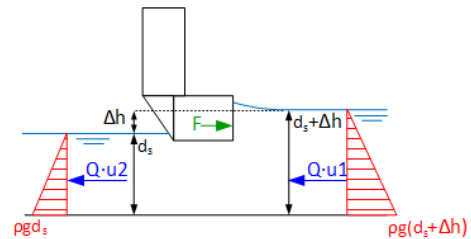


Figure 5.6: Barrier momentum balance schematization, with hydrostatic loads in red, momentum associated with flow in blue and the force from the gate in green

(B2) Momentum balance approach

From the discharge and the local head difference at the barrier a schematized momentum balance may be set up, with as unknown factor the total load on the gates parallel to the flow direction (Elger et al., 2013). The reason for using this approach is that the total loading on the gate can be estimated, which is more than only the hydrostatic load.

A longitudinal sketch of the used schematization is shown in Figure 5.6, with water levels and discharges presumed known in a cross-section upstream and downstream of the barrier (flow from right to left, in line with Figure 5.1). The water levels are given in terms of the seaside water depth and the local head difference. Included in the momentum balance are the hydrostatic loads at the ends of the control volume, the momentum of the water flowing in and out of the volume and the force acting from the retaining wall on the control volume (all loads act parallel to the flow direction).

From the total load on the barrier, which is parallel to the flow direction, the load on the short side of the retaining wall may be estimated. The load on the short side is determined from its size relative to the full canal width. A reduction factor is applied to find the part of the force that acts in a tangential direction relative to the retaining wall.

(C1) Cross-sectional water level variation

A variation in the water level has been suggested to play a reducing role in the mystery force (Bakker, 2008). This cross-sectional water level variation, with a decreased water level in the canal centre, is suggested to be a function of the discharge, and has been noted during model tests (WL|Delft Hydraulics, 1990b).

Due to the water level variation, the retaining walls will want to float to the canal centre (Bakker, 2008). The effect causes the gravitational force on the door to have a horizontal component that is compensated by a force in the pull/push rod (see Figure 5.7).

It must however be noted that a trim angle response is not necessarily caused by a water level variation over the cross-section, for example, in this report eccentric loading due to the mystery force is theorized to play a role in the observed trim angle response (see Figure 5.2).

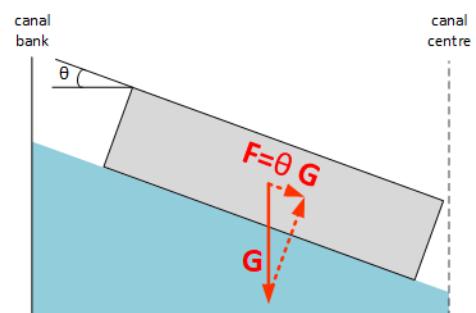
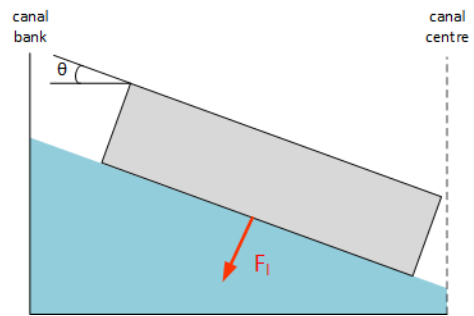


Figure 5.7: Tangential force induced by water level variation

(C2) Suction force tangential contribution

In combination with the inclined retaining walls, a suction force acting on the bottom of the retaining wall may contribute to the observed mystery force (Figure 5.8). This force can be described analogous to a lift force, caused by flow under the wall that acts perpendicular to the bottom of the retaining wall. This force can be linked to an increase of the velocity head under the gate, which through Bernoulli's law must have a reduction of the pressure head under the gate as a consequence.



A similar effect can be seen in ships, where the draft increases with increasing flow velocities, for ships this effect is noted as *squat* (Verheij et al., 2008).

This effect has been researched for the barrier using pressure measurements in the 2D physical model (WL|Delft Hydraulics, 1990a). The main conclusion from the research was that, for big vertical flow gaps, the suction force is equal to the head difference (BMK, 1992a). The head difference in the scale tests was not measured directly at the barrier, and big vertical flow gaps were not the focus of these tests. Therefore, it cannot be said with certainty that these results directly apply to the situation considered in this report. In this report, the suction force is estimated from an energy balance.

At both short sides of the retaining wall suction effects may exist as well, since there are gaps through which water flows, and the velocity head can be expected to increase. In this analysis it is assumed that at both short sides an approximately equal suction force occurs, and thus this contribution is not taken in account.

5.2.2. Definition

The full derivation and definition of the different models are given in Appendix H. The model equations are summarized in table 5.1 and 5.2. The parameters in the model definitions are given in Table 5.3. Quantification and testing of these models is treated in subsection 6.1.1.

Model Identifier	Model description	Included variables	Formula
B1	Local head difference	<ul style="list-style-type: none"> •Peak discharge (Q) •Vertical opening (d) 	$F = \rho g \cdot [A_{\text{short}}\Delta h + 6.5\Delta h^2],$ $\Delta h = \left(\frac{Q}{\mu \cdot B \cdot d}\right)^2 \cdot \frac{1}{2g}$
B2	Momentum balance	<ul style="list-style-type: none"> •Peak discharge (Q) •Vertical opening (d) •Seaside Water level (d_s) 	$F = 0.021 \left[\frac{1}{2} \rho g B (\Delta h^2 + 2d_s \cdot \Delta h) - \rho Q^2 \left(\frac{\Delta h}{B \cdot d_s \cdot (d_s + \Delta h)} \right) \right],$ $\Delta h = \left(\frac{Q}{\mu \cdot B \cdot d}\right)^2 \cdot \frac{1}{2g}$

Table 5.1: Force model for short side loading

Model Identifier	Model description	Included variables	Formula
C1	Water level variation related	• Trim angle effect (θ_{eff})	$F = -G \cdot \theta_{\text{eff}}$
C2	Suction force related to average flow velocity	• Discharge (Q) • Vertical opening (d) • Trim angle peak (θ_{peak})	$F = \theta_{\text{peak}} \cdot A_{\text{bottom}} \cdot \rho g \cdot u^2, u = \frac{Q}{\mu \cdot B \cdot d}$

Table 5.2: Force related additional effects

Parameters		
g	Gravitational constant	9.81 m/s ²
ρ	Water density	1,012 kg/m ³
G	Gate weight	126,000 kN
B	Waterway width	360 m
μ	Contraction coefficient	0.65 [-]
A_{bottom}	Retaining wall bottom surface area	2,763 m ²
A_{short}	Retaining wall short side surface area	60 m ²

Table 5.3: Parameters employed in formulae from Table 5.1-5.2

5.3. Trim angle effect

5.3.1. Description

The mystery force is expected to generate a moment on the retaining wall, which leads to a trim angle increase (Figure 5.2). In this section, this assumption is extended to a model for the trim angle effect. If, as expected, the mystery force is related to the discharge, the mystery force builds up slowly (the period over which the discharge and mystery force build up is in the order of 1 hour). For this reason, the trim effect is considered quasi-stationary, without considering inertia effects. In the model the retaining wall is regarded as a ship-like object in pitch, the degree of freedom indicated with θ in Figure 5.9, and loaded by the moment induced by the mystery force. In this report the terms trim and pitch are used interchangeably, they refer to the same movement of the retaining walls.

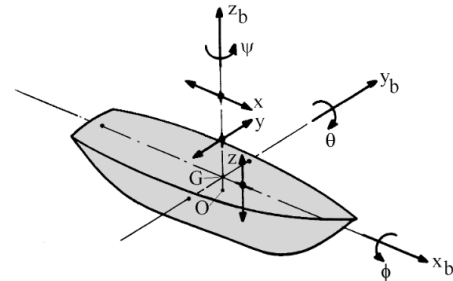


Figure 5.9: Ship degrees of freedom, image from Journée and Massie, 2001

As given in section 5.1 other contributions than due to the mystery force may exist. Changes in pitch have been suggested to lead to a water level variation over the cross-section of the waterway, which lead to trim of the retaining walls. Furthermore, the distribution of suction force on the bottom of the retaining wall may generate a moment on the retaining wall.

From the mystery force models, no clear contribution of these two effects is identified (subsection 6.1.1). For quantification of a water level variation over the channel width, information on its relation with the flow conditions are required. For quantification of a moment due to the suction force, information on the distribution of the flow velocity over the channel cross-section is a prerequisite. For these reasons, the modelling of contributions other than the mystery force to the trim effect is not considered in this report.

5.3.2. Definition

A model is defined based on the above description, where the barrier is simplified to two rectangular gates. This reduces the system to one spatial dimension, the axis along the cross-section of the waterway (Figure 5.10).

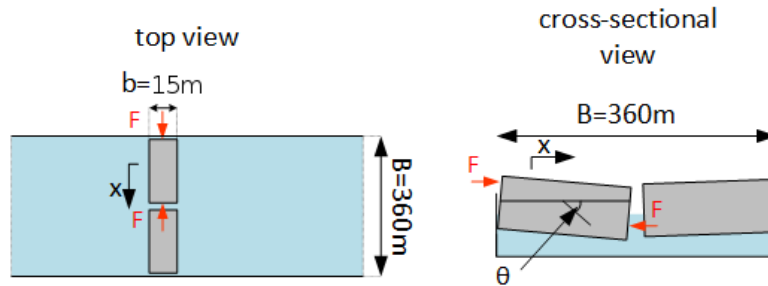


Figure 5.10: 1D retaining wall model with rotational degree of freedom

The retaining walls are modelled to only move in the given degree of freedom θ (as a pitching ship), equivalent to the degree of freedom denoted as trim in descriptions of the Maeslant barrier (Figure 2.2). The governing equation is given for one retaining wall (load and resistance on both walls is assumed the same). As the model assumes a quasi-stationary situation, time derivatives in the equation for pitch are not taken into account. This gives the following hypothesized model for the trim θ in radians (Journée & Massie, 2001):

$$\theta = \frac{M}{k_{hd}} = \frac{e \cdot F_{MF}}{k_{hd}} \quad (5.2)$$

With:

- $e = 20$ m: estimated arm between the two points of loading of F
- $k_{hd} = 7.0 \cdot 10^{10}$ Nm/rad: estimated rotational stiffness of retaining wall (only considering the effect of hydrostatic loading)
- F_{MF} (N): mystery force, the presumed load on the retaining wall

The derivation of the estimated spring stiffness, k_{hd} , and arm, e , is given in Appendix I. The eccentricity, e , of the loading due to the mystery force is an estimate based on the presumed location of the mystery force. The mystery force is estimated at the centre of the hydrostatic loading, one third of the draught from the bottom of the retaining wall. It seems reasonable that this estimate may not be off by more than 2 m. This estimated value of 2 m leads to an uncertainty in the moment due to the mystery force of 10%.

To consider effects that are not modelled in this model an empirical stiffness, k_{emp} , may be considered, instead of the estimated stiffness, k_{hd} , with as goal the incorporation of these effects in an equivalent stiffness that describes the retaining wall response. The underlying assumption is that these effects scale with the mystery force, and thus roughly with the discharge squared (which follows from the models in section 5.2).

5.4. Mode 3 effect

5.4.1. Description

As described in section 5.1, a change of trim of the retaining walls is expected to lead to cross-sectional variation of the discharge under the retaining wall, which in turn may influence the water level on the seaside of the barrier (this relation is the basis for the mode 3 effect, see section 2.5).

The schematization for the mode 3 model is similar as used for the trim effect model (see Figure 5.10), one of the retaining walls is modelled as rectangular pitching object and symmetry of the two retaining walls is again assumed, because of which the equations are derived for one retaining wall.

The inertia and damping effects of the retaining wall, which have not been considered in the quasi-steady approach for the trim angle effect, are estimated based on the analogy with a pitching ship. The damping term is estimated from an assumed damping ratio and the system inertia and stiffness.

To model the water level on the seaside of the retaining wall, the downstream waterway is divided in two discrete segments (Figure 5.11). For both of these two segments, a discharge balance is considered. This discharge balance determines the change of water level in the respective segment, if the amount of water in a segment decreases the water level must decrease and vice versa. This results in a model with three unknown functions of time (two water levels and the retaining wall pitch), through a further assumption of anti-symmetry of the water levels this is reduced to two (one water level and the retaining wall pitch).

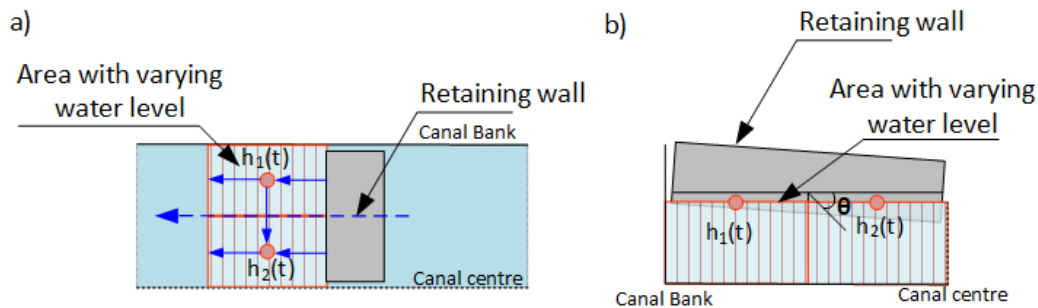


Figure 5.11: a) Mode 3 model top view, b) model front view. Two variables (h_1, h_2) that represent the water level deviation in 2 marked discrete segments, θ indicates the retaining wall pitch. The solid arrows indicate flow in and out of the marked segments, the dotted arrow the overall flow direction.

The different flows (solid arrows in Figure 5.11) are determined for deviations from a stationary seaward flow, by assuming small changes of the retaining wall position and of the water level in the two discrete segments. The water levels h_1 and h_2 are both described as deviations from the stationary seaside water level. In the text below the different flows, indicated with the solid arrows in Figure 5.11 are described as modelled.

The discharge from upstream that flows under the retaining wall into the marked segments is assumed to directly follow changes in the system (as described with Equation 2.1). A change of retaining wall position is also associated with another effect, due to a change of the water volume stored directly under the retaining wall the flow into the downstream segments may be impacted. Both these effects are implemented as described during the design phase research (BMK, 1992b).

A deviation of the water level in the discrete segments is associated with a deviation of the flow towards further downstream. Since this flow needs time to respond to an increased head difference, it is associated with inertia. Downstream of the areas highlighted in Figure 5.11 the water level is assumed to be constant. For this to hold, the area further downstream must be large such that the effects of discharge variations are small. Over longer periods of time this does not hold, for example the tide influences the water level in the canal. No indication exists that this slow variation is relevant for the occurrence of the mode 3 effect

The discharge between the two segments, marked in Figure 5.11, is associated with a similar inertia, which enables the possibility of an effect similar to a standing wave. The first order wave in the described model corresponds to the second order wave observed in the full model (section 2.5). This flow was not explicitly included in the model used during the design phase.

From the model described above a system of second order equations is derived of which the onset of instability is investigated.

5.4.2. Definition

The system is derived in terms of three unknown functions of time, which are the water level deviations from a stationary situation in the two discrete segments and the door pitch angle: $h_1(t)$, $h_2(t)$, $\theta(t)$ (Figure 5.11). After derivation, this system is simplified into a system of $h_1(t)$ and $\theta(t)$

In the system definition, expressions that hold for both downstream areas separately are written with the subscript i (with $i = 1, 2$ which describe the equations belonging to h_1 and h_2 respectively).

Continuity equation

For each of the two discrete segments, the discharge balance is expressed as:

$$\Delta x \cdot \Delta s \cdot \dot{h}_i = \Sigma \Delta Q_j \quad (5.3)$$

In which:

- $\Delta x \cdot \Delta s$: the area of the discrete segments (Figure 5.12). Δx is half of the retaining wall width. Δs is a measure of the streamwise length of the segment.
- \dot{h}_i : time derivative of h_i , the velocity of water level change in the segment.
- $\Sigma \Delta Q_j$: sum of discharge deviations in and out of the segment

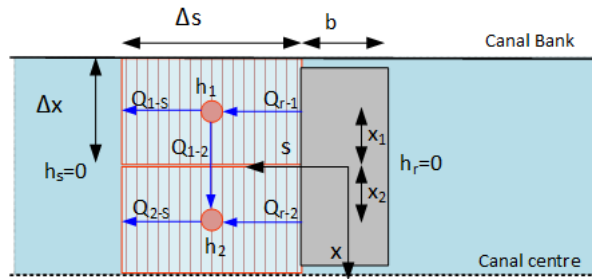


Figure 5.12: Discharge elements contributing to the continuity in h_1 and h_2 . $h_s = 0$ and $h_r = 0$ indicate that up- and downstream no deviations from the stationary situation occur

To describe the different discharge contributions, ΔQ_j , a notation of the different flows is introduced (Figure 5.12). The directions in the figure indicate the assumed positive flow direction. The deviation in discharge, ΔQ_j , is a function in time of the change from a stationary discharge $Q_{j,0}$, which together describe the total discharge as function of time:

$$Q_j(t) = Q_{j,0} + \Delta Q_j(t) \quad (5.4)$$

For both discrete basins, the general continuity equation can be expanded with the relevant discharge terms from Figure 5.12:

$$\Delta x \cdot \Delta s \cdot \dot{h}_1 = \Sigma \Delta Q_j = \Delta Q_{r-1} - \Delta Q_{1-s} - \Delta Q_{1-2} \quad (5.5)$$

$$\Delta x \cdot \Delta s \cdot \dot{h}_2 = \Sigma \Delta Q_j = \Delta Q_{r-2} - \Delta Q_{2-s} + \Delta Q_{1-2} \quad (5.6)$$

Geometry definition

To derive the different discharge contributions, ΔQ_j , the system geometry is defined (Figure 5.13).

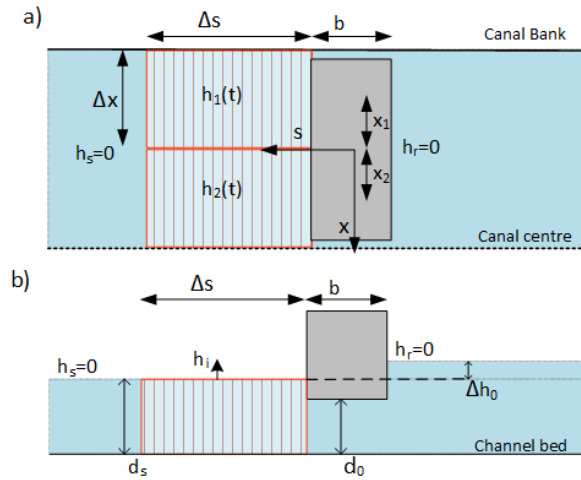


Figure 5.13: Mode 3 model top view (a) and side view (b) with defined geometry

The following terms follow directly from schematizing the Maeslant barrier (Rijkswaterstaat, n.d.-b):

- $\Delta x = 90$ m: half the retaining wall width
- $x_1 = -45$ m: location of segment h_1 along x -axis
- $x_2 = 45$ m: location of segment h_1 along x -axis
- $b = 15$ m: retaining wall streamwise width

The following variables are dependent on the flow situation and therefore have no set value:

- d_s (m): seaside water level relative to bed
- Δh_0 (m): initial local head difference.
- d_0 (m): initial vertical flow gap below the retaining wall.

Δs (in meters) is the unknown measure describing the streamwise length participating in the system, this factor does not follow from the system definition and during the quantification it is estimated such that the model results best match expectations.

The system is defined such that the two functions of time h_i describe small deviations from the water depth, d_s . At both the sea and river side, the water depth remains at their initial level (d_s and $d_s + \Delta h_0$ respectively), indicated with $h_s = 0$ and $h_r = 0$ in Figure 5.13.

Retaining wall discharge ΔQ_{r-i}

The flow from upstream, ΔQ_{r-i} (Figure 5.12), has two contributions, one due to impact on the flow and one due to change of the storage volume directly under the retaining wall, these two effects indicated with subscript a and b respectively.

The discharge from upstream is derived based on Torricelli's law, taking into account deviations of the retaining wall pitch and water levels changes in the discrete segments. The total vertical flow gap is a function of the retaining wall pitch, $d(\theta)$, which follows from the schematization in Figure 5.14. The total head difference is a function of the water level deviation, $\Delta h(h_i)$. The impact of h_i on the head difference follows from the definitions in Figure 5.13.

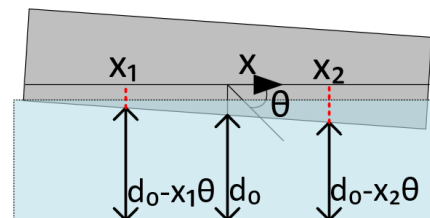


Figure 5.14: Retaining wall front view for d_i schematisation

This leads to the equation for $Q_{r-i,a}$:

$$Q_{r-i,a} = \Delta x \cdot \mu \cdot d(\theta) \cdot \sqrt{2g\Delta h(h_i)} \quad (5.7)$$

With as functions for the vertical flow gap and local head difference:

$$\begin{aligned} d(\theta) &= d_0 - x_i \theta \\ \Delta h(h_i) &= \Delta h_0 - h_i \end{aligned} \quad (5.8)$$

In which:

- $\Delta x = 90$ m: half the retaining wall width
- $\mu = 0.65$ (-): assumed discharge coefficient (Appendix H)
- $g = 9.81$ m/s²: gravitational constant
- d_0 (m): vertical flow gap without trim of retaining wall
- θ (rad): retaining wall trim angle
- x_i (m): location of segment h_i along x -axis
- Δh_0 (m): local head difference
- h_i (m): water level variation

The discharge *variation*, $\Delta Q_{r-i,a}$, for small changes of θ and h_i , is obtained from the total discharge by differentiating $Q_{r-i,a}$ with respect to θ and h_i (BMK, 1992b). The linearized discharge deviation is described with these two derivatives:

$$\Delta Q_{r-i,a} = \frac{\partial Q_{r-i,a}}{\partial \theta} \theta + \frac{\partial Q_{r-i,a}}{\partial h_i} h_i \quad (5.9)$$

The derivative with respect to θ is:

$$\frac{\partial Q_{r-i,a}}{\partial \theta} = \frac{\partial [d(\theta)]}{\partial \theta} \cdot \Delta x \cdot \mu \cdot \sqrt{2g\Delta h_0} = -x_i \cdot \Delta x \cdot \mu \cdot \sqrt{2g\Delta h_0} \quad (5.10)$$

The derivative with respect to h_i is obtained through two steps, first the chain rule is applied:

$$\begin{aligned} \frac{\partial Q_{r-i,a}}{\partial h_i} &= \frac{\partial [\Delta x \cdot \mu \cdot d_0 \cdot \sqrt{2g\Delta h(h_i)}]}{\partial h_i} = \frac{\partial [\sqrt{2g(\Delta h_0 - h_i)}]}{\partial h_i} \cdot \Delta x \cdot \mu \cdot d_0 \\ &= \frac{\partial \sqrt{2g(\Delta h_0 - h_i)}}{\partial [2g(\Delta h_0 - h_i)]} \cdot \frac{\partial [2g(\Delta h_0 - h_i)]}{\partial h_i} \cdot \Delta x \cdot \mu \cdot d_0 = \frac{1}{2\sqrt{2g(\Delta h_0 - h_i)}} \cdot -2g \cdot \Delta x \cdot \mu \cdot d_0 \end{aligned} \quad (5.11)$$

Next this non-linear result is linearised in $h_i = 0$, and rewritten:

$$\approx \frac{1}{2\sqrt{2g\Delta h_0}} \cdot -2g \cdot \Delta x \cdot \mu \cdot d_0 = \frac{\sqrt{2g\Delta h_0}}{2(2g\Delta h_0)} \cdot -2g \cdot \Delta x \cdot \mu \cdot d_0 = -\Delta x \cdot \mu \cdot \sqrt{2g\Delta h_0} \cdot \frac{d_0}{2\Delta h_0} \quad (5.12)$$

This result of the two terms is analogous to the result found for the one-dimensional model used in the design phase (BMK, 1992b):

$$\Delta Q_{r-i,a} = -\Delta x \cdot \mu \sqrt{2g\Delta h_0} \cdot x_i \theta - \Delta x \cdot \mu \sqrt{2g\Delta h_0} \cdot \frac{d_0}{2\Delta h_0} \cdot h_i \quad (5.13)$$

With variables as defined in Equation 5.7. The first term describes the effect due to a change of vertical flow gap $x_i \theta$ and the second term due to a change of head difference with h_i .

A change of pitch of the retaining wall changes the water volume stored under the retaining wall. One half the wall is raised and the stored volume increases, and vice versa. This change of volume under

the retaining wall is found for each half of the retaining wall by taking the product of the area under the retaining wall and the average rate of change of the vertical retaining wall position (Figure 5.14). It is assumed this directly results in a changed flow towards the downstream segments:

$$\Delta Q_{r-i,b} = b \cdot \Delta x \cdot x_i \cdot \dot{\theta} \quad (5.14)$$

with:

- $b = 15$ m: retaining wall streamwise width
- $\Delta x = 90$ m: half the retaining wall width
- $\dot{\theta}$ (rad/s): retaining wall trim angle velocity
- x_i (m): location of segment along x -axis

Seaward discharge Q_{i-s}

Further downstream of the barrier, seaward of the discrete segments, the depth is assumed to be constant at d_s from the bed (Figure 5.13). A change of water level directly downstream of the barrier h_i leads to a head difference between the segment in front of the barrier and further downstream. This will lead to flow, which due to inertia effects cannot instantly follow the change in head difference. This effect is modelled for the segment h_1 with a force balance around the control volume schematized as in Figure 5.15.

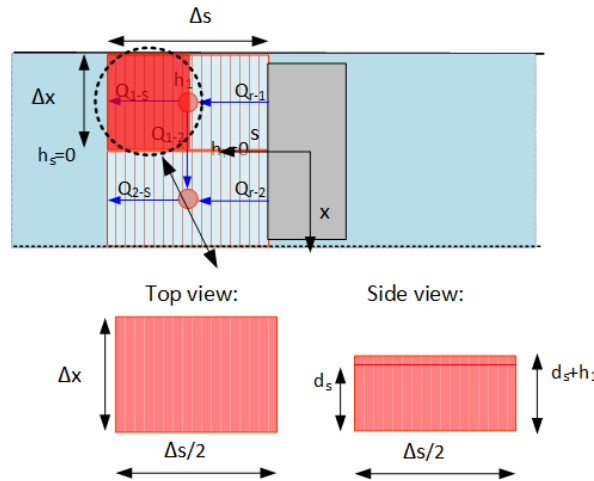


Figure 5.15: Control volume for flow component Q_{1-s}

For the given schematization the force balance is completed for small values of h_1 , such that the sum of forces is equal to a hydrostatic pressure difference, which is given as a linear function of h_1 . In this derivation, the bed is assumed flat and advective and friction terms are not considered (with geometry as defined in Figure 5.13). The equation is derived from Newton's second law:

$$m \cdot \dot{u}_{1-s} = \sum F \quad (5.15)$$

with as mass term, m , the mass of the control volume:

$$m = \rho \cdot \Delta x \cdot \Delta s / 2 \quad (5.16)$$

With the unknown acceleration term, \dot{u}_{1-s} , expressed in terms of the unknown discharge change:

$$\dot{u}_{1-s} = \dot{Q}_{1-s} / (d_s \cdot \Delta x) \quad (5.17)$$

The total forcing, $\sum F$, for small values of h_1 , and only considering hydrostatic terms is:

$$\sum F = \rho g \cdot \Delta x \cdot d_s \cdot h_1 \quad (5.18)$$

The result is a formulation for the change of discharge:

$$\dot{Q}_{1-s} = \left(\frac{2}{\Delta s} \right) \cdot g \cdot d_s \cdot \Delta x \cdot h_1 \quad (5.19)$$

With the following variables used in the derivation:

- $\rho = 1012 \text{ kg/m}^3$: water density
- $\Delta x = 90 \text{ m}$: half the retaining wall width
- $\Delta s \text{ (m)}$: parametric segment length
- $d_s \text{ (m)}$: seaside water level relative to bed
- $g = 9.81 \text{ m/s}^2$: gravitational constant

This change of discharge \dot{Q} must be equal to the change of the deviation of the discharge $\Delta \dot{Q}$ (as follows from the definition in Equation 5.4).

The same type of relation for hold for the seaward discharge Q_{2-s} :

$$\dot{Q}_{2-s} = \left(\frac{2}{\Delta s} \right) \cdot g \cdot d_s \cdot \Delta x \cdot h_2 \quad (5.20)$$

Cross-section discharge

A difference in water levels between the two discrete basins results in a discharge Q_{1-2} . This discharge also experiences inertia effects, and is found using a similar derivation as for the seaward components. Only the result is given (geometry as defined in Figure 5.13, variables as in Equation 5.19):

$$\dot{Q}_{1-2} = \left(\frac{1}{\Delta x} \right) \cdot g \cdot d_s \cdot \Delta s \cdot (h_1 - h_2) \quad (5.21)$$

Based on this relation, the existence of standing waves in the cross-section can be explained based on an analogy of this discrete system with the Saint-Venant equations. The Saint-Venant equations consist of a continuity equation and a momentum balance equation, similar to the discrete system described with the equations for h_1 , h_2 , and \dot{Q}_{1-2} .

To further support this analogy, and to gain insight into the waves predicted by the discrete system, the simplified 1D-case is considered where h_1 , h_2 , and \dot{Q}_{1-2} form a system in the textbox.

Discrete model for standing wave

For the 1D-case, the system reduces to the following three equations:

$$\begin{aligned}\Delta x \cdot \Delta s \cdot \dot{h}_1 &= -Q_{1-2} \\ \Delta x \cdot \Delta s \cdot \dot{h}_2 &= Q_{1-2} \\ \Rightarrow \dot{Q}_{1-2} &= \left(\frac{1}{\Delta x}\right) \cdot g \cdot d_s \cdot \Delta s \cdot (h_1 - h_2)\end{aligned}\quad (5.22)$$

By taking the time derivative of the first equation, this equation can be combined with the third equation. From the first two equations, it follows that $h_2 = -h_1$ (if this also follows from the initial conditions). The system reduces to:

$$\begin{aligned}\Delta x \cdot \Delta s \cdot \ddot{h}_1 &= -\left(\frac{2}{\Delta x}\right) \cdot g d_s \cdot \Delta s \cdot h_1 \\ \ddot{h}_1 + \left(\frac{2}{\Delta x^2}\right) \cdot g \cdot d_s \cdot h_1 &= 0\end{aligned}\quad (5.23)$$

The natural period of the system is (which is found through substituting the general solution form $\exp(i\omega t)$, where ω is the angular frequency):

$$T = \frac{2\pi}{\omega} = 2\pi / \sqrt{\left(\frac{2}{\Delta x^2}\right) \cdot g \cdot d_s} = \frac{\sqrt{2}\pi \cdot \Delta x}{\sqrt{g \cdot d_s}}\quad (5.24)$$

For $\Delta x = 90$ m, and the approximate depth at the barrier $d_s = 17$ m this yields:

$$T = \frac{\sqrt{2}\pi \cdot 90}{\sqrt{g \cdot 17}} = 31.0\text{s}\quad (5.25)$$

This can be compared with result from shallow water linear wave theory, which is computed with expected wavelength ($\lambda = 360$ m, Figure 2.4) and the shallow water wave speed ($c = \sqrt{g \cdot d_s}$)

$$c = \frac{\lambda}{T} \Rightarrow T = \frac{\lambda}{\sqrt{g \cdot d_s}} = \frac{360}{\sqrt{g \cdot 17}} = 27.9\text{s}\quad (5.26)$$

The period for the discrete system is higher than found from linear wave theory, the difference is about 10%.

Retaining wall governing equation

The governing equation, based on the earlier introduced analogy of the retaining wall as a pitching ship (with degree of freedom θ , as in Figure 5.11), has the form (Journée & Massie, 2001):

$$(J + J_{hd})\ddot{\theta} + \zeta\sqrt{(k_{est} \cdot (J + J_{hd}))}\dot{\theta} + k_{est}\theta = e \cdot F_{MF}\quad (5.27)$$

With:

- $J = 3.5 \cdot 10^{10}$ kg · m²: retaining wall inertia (bar schematization)
- $J_{hd} = 3.9 \cdot 10^{11}$ kg · m²: retaining wall added inertia (2D schematization)
- $k_{est} = 7.25 \cdot 10^9$ N · m/rad: retaining wall spring term, estimated from constant trim effect (subsection 6.1.2)
- $\zeta\sqrt{(k_{est} \cdot (J + J_{hd}))} = 5.6 \cdot 10^9$ kg · m/(s · rad): retaining damping term, from an estimated damping ratio of 5%, and the retaining wall inertia and stiffness
- $e \cdot F_{MF}$ (Nm): moment induced by mystery force, estimated arm $e=20$ m multiplied by force F (from Appendix I)

The inertia and damping in this system are derived by approximating the floating retaining walls, as treated in Appendix J. The spring coefficient is directly taken from the analysis regarding the constant trim effect, thereby assuming that the spring coefficient is the same for both effects.

In addition, the retaining wall is loaded by an external moment due to loading water level deviation in the two downstream segments (Figure 5.16). Assuming the water level deviations h_1 and h_2 act over the full streamwise width of the retaining wall b gives:

$$\rho g \cdot b \cdot \Delta x \sum_{i=1}^2 (x_i \cdot h_i) \quad (5.28)$$

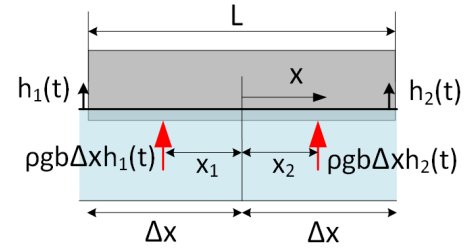


Figure 5.16: Moment exerted on retaining wall by h_1 and h_2

With:

- $\rho = 1012 \text{ kg/m}^3$: water density
- $g = 9.81 \text{ m/s}^2$: gravitational constant
- $b = 15 \text{ m}$: retaining wall streamwise width
- $\Delta x = 90 \text{ m}$: half the retaining wall width
- x_i (m): location along x -axis of segment
- h_i (m): water level variation of segment

Inclusion of this term yields the equation:

$$(J + J_{\text{hd}})\ddot{\theta} + \zeta\sqrt{(k_{\text{est}} \cdot (J + J_{\text{hd}}))}\dot{\theta} + k_{\text{hd}}\theta = e \cdot F + \rho g \cdot b \cdot \Delta x \sum (x_i \cdot h_i) \quad (5.29)$$

With variables as defined before.

System description

Based on the equations of the downstream basin and of the retaining wall, a coupled system is described. The impact of the pitch of the flow towards on the two discrete segments is antisymmetric, and all equations are linear, it is therefore assumed that $h_2 = -h_1$ (assuming no influence of initial conditions), which reduces the number of degrees of freedom of the coupled system.

Combining the equations for the different discharge components with the continuity equation for h_1 yields a second order differential equation. The steps are given below, and are similar to the system derived during the design phase (BMK, 1992b).

First, the continuity equation is differentiated in time (Δ 's are dropped for the discharge contributions since $\dot{Q} = \Delta\dot{Q}$, as follows from Equation 5.4):

$$\Delta x \cdot \Delta s \cdot \ddot{h}_1 = \dot{Q}_{r-1} - \dot{Q}_{1-s} - \dot{Q}_{1-2} \quad (5.30)$$

The two components of the discharge deviation ΔQ_{r-1} are differentiated with respect to time for use in Equation 5.30:

$$\dot{Q}_{r-1,a} = -\Delta x \cdot \mu\sqrt{2g\Delta h_0} \cdot x_1 \dot{\theta} - \Delta x \cdot \mu\sqrt{2g\Delta h_0} \cdot \frac{d_0}{2\Delta h_0} \cdot \dot{h}_1 \quad (5.31)$$

$$\dot{Q}_{r-1,b} = b \cdot \Delta x \cdot x_i \cdot \ddot{\theta} \quad (5.32)$$

Next, Equation 5.30 is expanded using the relations for the discharge components:

$$\Delta x \cdot \Delta s \cdot \ddot{h}_1 = -\Delta x \cdot \mu\sqrt{2g\Delta h_0} \cdot x_1 \dot{\theta} - \Delta x \cdot \mu\sqrt{2g\Delta h_0} \cdot \frac{d_0}{2\Delta h_0} \cdot \dot{h}_1 + b \cdot \Delta x \cdot x_1 \cdot \ddot{\theta} - \left(\frac{2}{\Delta s}\right) \cdot g d_s \cdot \Delta x \cdot h_1 - \left(\frac{2}{\Delta x}\right) \cdot g d_s \cdot \Delta s \cdot h_1 \quad (5.33)$$

This equation combined with the retaining wall governing equation (Equation 5.29), the system is written in the form:

$$M \begin{bmatrix} \ddot{\theta} \\ \dot{h}_1 \end{bmatrix} + C \begin{bmatrix} \dot{\theta} \\ \dot{h}_1 \end{bmatrix} + K \begin{bmatrix} \theta \\ h_1 \end{bmatrix} = \begin{bmatrix} e \cdot F \\ 0 \end{bmatrix} \quad (5.34)$$

With the matrices:

$$M = \begin{bmatrix} J + J_{hd} & 0 \\ -b \cdot \Delta x \cdot x_1 & \Delta x \cdot \Delta s \end{bmatrix}$$

$$C = \begin{bmatrix} \zeta \sqrt{(k_{est} \cdot (J + J_{hd}))} & 0 \\ \Delta x \cdot \mu \sqrt{2g\Delta h_0} \cdot x_1 & \Delta x \cdot \mu \sqrt{2g\Delta h_0} \cdot \frac{d_0}{2\Delta h_0} \end{bmatrix} \quad (5.35)$$

$$K = \begin{bmatrix} k_{est} & 2\rho g \cdot b x_1 \cdot \Delta x \\ 0 & \left(\frac{\Delta x}{\Delta s} + \frac{\Delta s}{\Delta x} \right) \cdot 2g d_s \end{bmatrix}$$

In this equation, the considered degrees of freedom are the retaining wall pitch, θ , and the water level, h_1 (Figure 5.11). All terms are defined in the derivation given in this subsection, and are therefore not repeated here.

6

Results and predictions

In this chapter, the conceptual models defined chapter 5 are tested against the data, and it is assessed whether these models give relevant predictions on the considered seaward flow effects. Where this is not the case, possible shortcomings of the models are shortly described, which are expanded upon in chapter 7. In addition, a selection of the most relevant statistical models is made to supplement the areas where the conceptual models are lacking. Using the selected conceptual and statistical models, a preliminary estimate of the different effects under extreme conditions is made.

6.1. Conceptual models

For each of the three seaward flow effects the different variables, considered in the conceptual models in chapter 5, are retrieved from the data. For quantification of the different variables, the value at the discharge peak is considered, the point at which the different effects are at their peak (subsection 3.6.2). The exact timing of the peak discharge is not always clear, for quantification a pragmatic approach based on the visualized data is used (Appendix D).

The model output is compared against the quantified magnitude of the different effects from section 3.5. Where applicable, uncertain model parameters are considered in the results to get further insight in the model quality. Based on these outcomes, a short evaluation of the conceptual models is given.

6.1.1. Mystery force results

Quantification

The variables considered in the models described in Table 5.1 and Table 5.2 are quantified in this paragraph, starting with the peak of the local discharge, which is chosen as the reference point.

The seaside water level is observed to be approximately at its minimum at the peak of the local discharge (Appendix D). Consequently, the same follows for the vertical flow gap, since the floating gates follow the water level. For these two variables, the minimum value found during the high floating phase is used as model input.

The trim effect, the increase of retaining wall trim during the period where the discharge peaks, is possibly linked to an effect due to a water level variation over the cross-section. The trim effect as identified previously (subsection 3.5.2) is, for this reason, used to give an upper bound estimate for the effect due to a cross-sectional water level variation (C1). For the tangential load due to suction force (C2) the absolute trim angle itself desired, not the relative increase of trim under flow considered for the trim effect, since the effect is the result of a load acting perpendicular to the retaining wall bottom. To obtain this value, the peak value of the trim angle signal as used for identifying the trim effect is used (subsection 3.5.2).

The results are compared to the mystery force as collected in subsection 3.2.2. The data for the test closure without data from strain gauges is disregarded, as also done for the empirical models in section 4.5.

Results

First, the head difference over the barrier for the different closures is determined. This step is given separately because it is the main input for the two models relating to the loading on the short side of the gate (B-models). The mystery force appears to show some correlation with this calculated head difference (Figure 6.1).

Based on the head difference, the B-models are completed, the corresponding results are compared in Figure 6.2. The models use multiple input variables, and for this reason the representation with the observed force on the horizontal axis and the modelled force on the vertical axis is used (as used in section 4.4).

It can be seen that the momentum model (B2) predicts forces more inline with the observations when compared to the hydrostatic model (B1). The hydrostatic model consequently predicts lower values than found for the mystery force, this leads to negative values for R^2 . This may seem counter-intuitive and is therefore further explained in the textbox below, using the observed mean plotted in Figure 6.2.

R^2 in model comparison

The B1 model has a negative R^2 -score (Figure 6.2). However, the scatter plot shows linear correlation. To understand that no discrepancy exists, the meaning of both the figure and R^2 must be considered.

In this case, R^2 is calculated between a modelled and observed value. From the used definition of R^2 (known as the coefficient of determination) it can be seen that it yields negative values if the model has a bigger residual sum of squares than a sum of squares based on the observed mean (Equation 4.2). The definition is seen to be different from simply the square of the correlation coefficient (which never yields a negative value). This difference comes to light because the modelled value is not the same as a linear regression fit (which never has a bigger residual sum of squares than the observed mean).

In short, in Figure 6.2 the model B1 has a worse fit to the data than a model consisting of solely the observed mean, and for that reason has a negative R^2 -score.

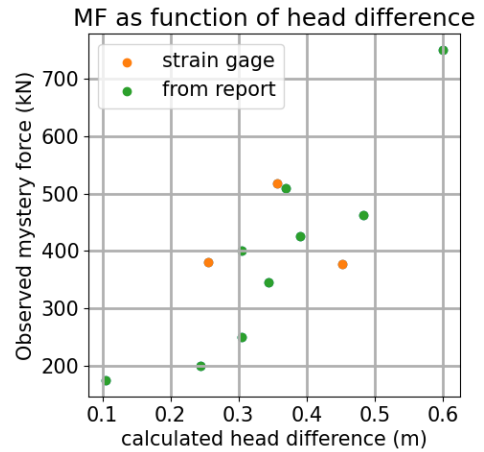


Figure 6.1: Head difference at maximum mystery force

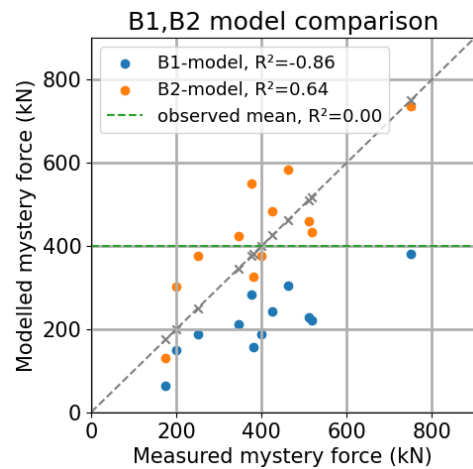


Figure 6.2: Results from physical base models plotted as function of observed mystery force

Addition of the C models is tested on the momentum model. As a first step these effects are simply added to the momentum model, the result is shown in Figure 6.3. Including the water level effect (C1) reduces the predicted forces significantly, the effect due to the suction force (C2) is limited. Neither has a clear positive effect on R^2 .

To further assess the momentum balance model, two uncertain parameters are considered as fitting parameter of the model. Considered are the discharge coefficient μ and the width B . Each of these parameters is considered separately as an unknown parameter, for which a non-linear curve fit is performed. Table 6.1 gives the fitted parameters, the R^2 of the resulting fit and the 90% confidence interval of the estimated parameter.

Parameter	unit	fitted value	90%-interval	R^2
B	meter	392	(351,433)	0.71
μ	-	0.68	(0.64,0.71)	0.71

Table 6.1: parameter fit for B2 (momentum model)

In terms of R^2 -score, both fits give a similar improvement to the fit in Figure 6.2. It can be checked that the confidence interval relative to the fitted value for the fitted discharge coefficient μ is about 50% smaller than that of the fit for the width B . This suggests that the best theoretical model for the mystery force is obtained with the coefficient μ amended to the estimated value:

$$\mu_{est} = 0.68 \tag{6.1}$$

The magnitude of both C models is only a rough estimate. To consider a possible over-estimation, a multiple regression fit to the observed mystery force is performed including the momentum balance model and both C models, with as regression parameters μ and reduction factors c_{C1} and c_{C2} . This fit yielded no further improvement in terms of R^2 compared to the result Table 6.1, and thus no indication for inclusion of either effect is given.

6.1.2. Trim effect results

Quantification

The described model considers only the mystery force as independent variable. Two options are considered, the observed mystery force as used in subsection 6.1.1, and the mystery force modelled with the fitted momentum balance model (section 5.2). This last quantity is used to check if this modelled force may be a better input than the observed force.

The results are compared to the trim effect as quantified in subsection 3.5.2.

Results

As a first step, the model is tested based on the estimated spring stiffness (based on the expected hydrostatic response) and the observed mystery force (Figure 6.4). It can be seen that this model severely underestimates the trim effect. Three possible reasons are given, the modelled moment on the retaining wall is too low, the stiffness of the retaining wall in trim is overestimated, or unidentified loads are present.

No clear reason for an underestimation of the load can be given. The mystery force is directly observed. The arm, leading to the moment, is an estimation, however it seems unlikely to significantly bigger than estimated, as it is limited by the height over the retaining wall.

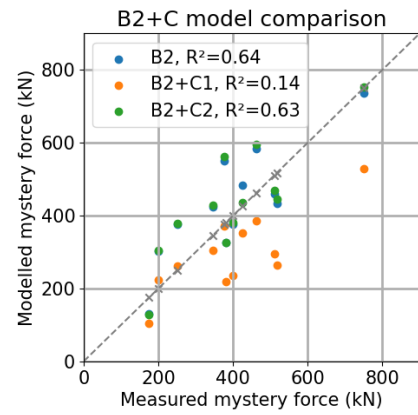


Figure 6.3: Results from momentum model plus C effects plotted as function of observed mystery force

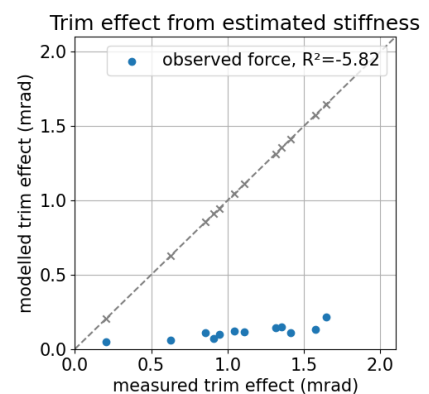


Figure 6.4: Result for constant trim effect

The total stiffness of the retaining wall is a more uncertain factor, furthermore as given in section 5.3 other factors that can act as load in pitch may exist. In the continuation of this subsection, an empirical stiffness is estimated that best models the observed trim effect.

A regression analysis is done with the stiffness as parameter. In addition to the observed mystery force, the mystery force from the momentum model is considered. The model for the fit is as following:

$$\hat{\theta} = \frac{e \cdot F_{MF}}{\hat{\beta}_0 \cdot k_{hd}} = \frac{e \cdot F_{MF}}{k_{emp}} \quad (6.2)$$

With:

- $e = 20$ m: estimated arm between the two points of loading of F
- $k_{hd} = 7.0 \cdot 10^{10}$ Nm/rad: estimated rotational stiffness of retaining wall (only considering the effect of hydrostatic loading)
- F_{MF} (N): mystery force, the presumed load on the retaining wall

$\beta_0 \cdot k_{hd}$ is equal to the empirical stiffness, k_{emp} . Such that β_0 expresses the estimated stiffness as a fraction of the initial estimate.

In terms of expected stiffness, both fits give very similar results (Figure 6.5), as expected since the momentum model is a fit to the observed mystery force. The difference between the quality of the fit for the observed and predicted mystery force is more notable. The predicted mystery force has a significantly higher R^2 score (0.86 over 0.69).

The fitted rotational stiffness is about 10% of the original estimate. This gives an amended model with a fitted rotational stiffness of the retaining wall:

$$\hat{\theta} = \frac{e \cdot F_{MF}}{k_{emp}} \quad (6.3)$$

- $e = 20$ m: Estimated arm between the two points of loading of F
- $k_{emp} = 7.25 \cdot 10^9$ Nm/rad: fitted retaining wall stiffness
- F_{MF} (N): mystery force, the presumed load on the retaining wall

6.1.3. Mode 3 effect results

Quantification

The quantification of the mode 3 effect is broken up in three elements. First, a global image of the relevant hydraulic conditions is given, used to give an indication of the conditions under which the derived mode 3 system is unstable. Since only an indication for instability of the system is looked at, the exact conditions per closure are less relevant. An estimate of the relevant range for the unknown model parameter Δs is given. Two coefficients are introduced to calibrate the influence of the discharge towards further down stream and of the damping effect due to the changing water level.

The model does not give predictions on the magnitude of the effect, this aspect is not considered for the mode 3 model.

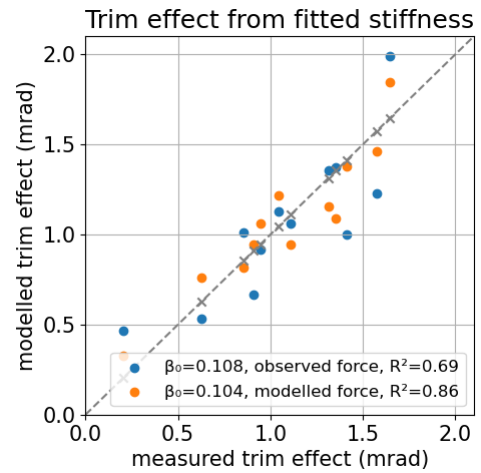


Figure 6.5: Constant trim effect model results with a fitted stiffness

Quantification: hydraulic conditions

The seaside water depth (d_s) and vertical flow gap (d_0) are considered as constant factors, the variations of these two factors are relatively minor. The magnitude is estimated based on observations, and the depth at the barrier (Appendix D, Figure H.4):

- $d_s = 17\text{m}$
- $d_0 = 10\text{m}$

For the initial head difference, Δh_0 , the variation is bigger, and through the damping matrix it may play a role in the determining the conditions in which the mode 3 effect occurs. A range of head differences between 0.2 and 1 m is considered, it is expected that the mode 3 effect occurs for a head difference exceeding 0.2-0.3 m (based on the range for which a mode 3 effect was observed, see the textbox). The head difference per closure is not explicitly considered in this section.

Relation head difference and mode 3

To assess the onset of the mode 3 effect, it is clarified at which head difference instability is expected. This is relevant since the parameters in the damping matrix are a function of this local head difference. The observed mode 3 variance is plotted as function of the local head difference (Figure 6.6). The local head difference is calculated as detailed in Equation H.1. Shown are the maximum mode 3 variance (Appendix C) against the calculated head difference at the peak discharge for each closure (green data points). Furthermore, for two closures with a clear mode 3 effect and complete data on the discharge the local head difference is calculated for the whole high floating period. The mode 3 variance is plotted as function of this head difference (the used time history of the discharge and mode 3 variance are as given in the overviews in Appendix D).

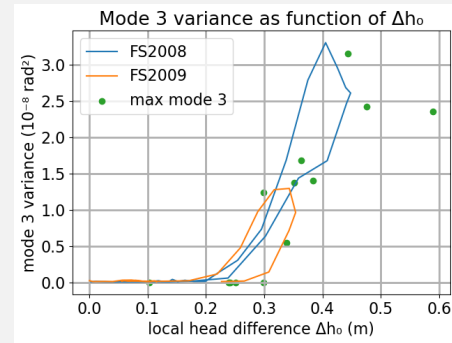


Figure 6.6: Mode 3 variance as function of local head difference

From Figure 6.6 it follows that the mode 3 effect occurs for a local head difference that exceeds 0.2-0.3 m, no exact value can be identified based on Figure 6.6. This may be a consequence of the identification method used for the mode 3 effect section 3.3, or effects related to the quality of the original data. For further analysis, it is estimated the mode 3 system is unstable for a local head difference exceeding 0.25 m.

Quantification: model parameters Δs

The value of the parameter Δs (the length of the downstream segments) is unknown. As a first estimate, a range of 10-500 meters is for Δs is considered.

The effect of Δs in this model can be described with the differential equation for h_1 (Equation 5.33) and dividing this equation by Δs (the differential equation for θ has no terms containing Δs and is therefore not considered):

$$\begin{aligned}
 & -\frac{1}{\Delta s} \cdot b \cdot \Delta x \cdot x_1 \cdot \dot{\theta} + \Delta x \cdot \dot{h}_1 \\
 & + \frac{1}{\Delta s} \cdot \Delta x \cdot \mu \sqrt{2g\Delta h_0} \cdot x_1 \cdot \dot{\theta} + \frac{1}{\Delta s} \cdot \Delta x \cdot \mu \sqrt{2g\Delta h_0} \cdot \frac{d_0}{2\Delta h_0} \cdot \dot{h}_1 \\
 & + \left(\frac{\Delta x}{(\Delta s)^2} + \frac{1}{\Delta x} \right) \cdot 2gd_s \cdot h_1 = 0
 \end{aligned} \tag{6.4}$$

For $\Delta s \Rightarrow \infty$ the effect of the terms related to flow from upstream, the terms, highlighted in red, reduces to 0. The discharge deviation is divided over an infinite area, and discharge deviations by the retaining wall can thus no longer affect the water level. For $\Delta s \Rightarrow \infty$ the effect of discharge deviations towards

the seaward end of the model, the term, highlighted in blue, also reduces to 0. The discharge towards the seaward end is no longer able to respond to a change of the water level at h_1 . By these two effects together, the downstream situation reduces to the equation for the one-dimensional standing wave for $\Delta s \Rightarrow \infty$ (described in Equation 5.23). This analysis of the different highlighted terms follows from the definition of h_1 in section 5.4.

Δs has two effects, the size of the discrete segment, and the inertia of flow towards the seaward end, that may be better described with distinct parameters. To do this end, a new coefficient, c_s , is added in the spring matrix:

$$K = \begin{bmatrix} k_{hd} & 2\rho g b x_1 \Delta x \\ 0 & \left(\mathbf{c}_s \cdot \frac{\Delta x}{\Delta s} + \frac{\Delta s}{\Delta x} \right) \cdot 2g d_s \end{bmatrix} \quad (6.5)$$

For $c_s = 1$ the system is the same, unchanged from the original definition. For values lower than 1 the relative effect of discharge variations towards sea is reduced (it is an increase of inertia effects, as follows from Equation 5.19), for $c_s = 0$ the system reduces to a system where no discharge variation towards further seaside takes place, regardless of the value for Δs .

Quantification: damping parameters

For the mode 3 effect an onset of instability is considered, the damping matrix that influences this onset is (from Equation 5.35):

$$C = \begin{bmatrix} \zeta \sqrt{(k_{hd} \cdot (J + J_{hd}))} & 0 \\ \Delta x \cdot \mu \sqrt{2g \Delta h_0} \cdot x_1 & \mathbf{c}_r \cdot \Delta x \cdot \mu \sqrt{2g \Delta h_0} \cdot \frac{d_0}{2\Delta h_0} \end{bmatrix} \quad (6.6)$$

It can be seen that this matrix contains an entry that is negative, highlighted in red (since x_1 is negative, see Figure 5.11), this factor can play a role in the onset of instability. It increases in magnitude when the initial head difference (Δh_0) increases. Furthermore, for increasing initial head differences the damping term, highlighted in blue, decreases in magnitude. From this, it appears that the stability of the system decreases for an increase in head difference over the barrier. To be able to assess the impact of the damping term in blue on the onset of instability, a coefficient, c_r , is introduced in the damping matrix, which is initially estimated as 1.

Results

The results for the mode 3 effect focus on explaining the occurrence of this effect, and not on its magnitude. The mystery force is regarded as a force that build up slow compared to the eigenperiods of the system, as only relations with the discharge, which build up relatively slowly (over a period of 1 hour, see Figure 3.10), have been found. For this reason, the mystery force is assumed to play no relevant role in the system.

First, an analysis on the expected natural periods of the system without damping matrix is given. Next, the influence of uncertain parameters in the model is analysed to derive a set of parameters for the system which best explain the observed behaviour.

Results: undamped modes

The solutions to system without external forcing and effects through the damping matrix can be found through substitution of the following general solution:

$$\begin{bmatrix} \theta(t) \\ h_1(t) \end{bmatrix} = \begin{bmatrix} 1 \\ r \end{bmatrix} \cdot \exp(i\omega t) \quad (6.7)$$

with:

- ω (rad/s): angular frequency
- $[1, r]$: Eigenvector describing magnitude of h_1 (meters) relative to θ (radians)

r describes the amplitude of the water level deviation (in meters) relative to a unity amplitude (in radians) of the retaining wall pitch. If the retaining wall follows the water level variation, it is expected that (from the cross-section geometry, see Figure 5.16):

$$r \approx -x_1 = 45 \text{ m} \quad (6.8)$$

The following determinant gives two solutions (which follows from the substitution in the system, defined in Equation 5.35):

$$|K - \omega_i^2 M| = \begin{vmatrix} -\omega_i^2(J + J_{hd}) + k_{emp} & 2\rho g \cdot b \cdot \Delta x \cdot x_1 \\ \omega_i^2 \cdot b \cdot \Delta x \cdot x_1 & -\omega_i^2 \cdot \Delta x \cdot \Delta s + \left(c_s \frac{\Delta s}{\Delta x} + \frac{\Delta x}{\Delta s}\right) \cdot 2g \cdot d_s \end{vmatrix} = 0 \quad (6.9)$$

With parameters as defined in section 5.4, and k_{emp} as estimated in subsection 6.1.2.

From Equation 6.9 it follows that the found frequencies do not depend on the loading due to the initial head difference, but do depend on the unknown parameters Δs and c_s . The two modes of the system Equation 6.9 are numerically calculated the estimated range for Δs , 10-500 m, and for $c_s = 1$ (see Figure 6.7). The two modes are presented in terms of their eigenperiod ($T_i = 2\pi/\omega_i$) and eigenvector ($[1, r_i]$).

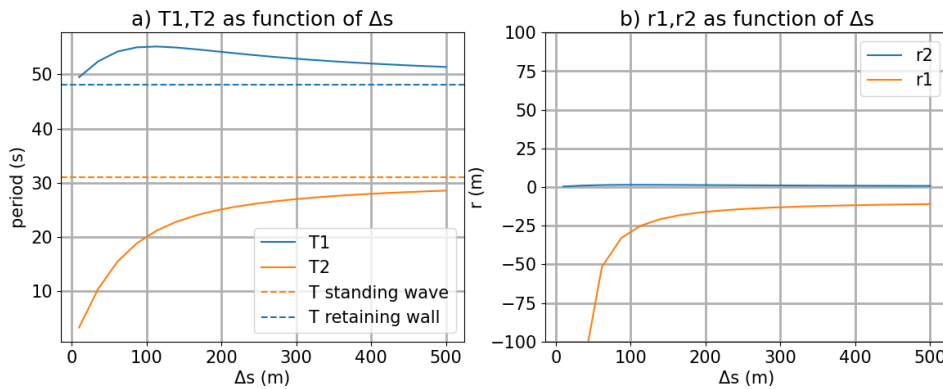


Figure 6.7: T and r as function of parameter Δs

It can be noted from Figure 6.7 that for big values of Δs the two periods trend towards respectively the eigenperiod of the pitching door and the eigenperiod of the standing wave (period calculated from Equation 5.29 and 5.25, plotted as dashed lines in Figure 6.7). Neither eigenmode explains the observed mode 3 effect, since the significant ($r \approx 45$ m) in phase motion of water level and pitch is not found for the period corresponding to the standing wave.

To understand this discrepancy, the eigenperiod of the retaining wall must be considered. From the physical model tests it followed that for the mode 3 effect the retaining wall was able to passively follow the standing wave (WL|Delft Hydraulics, 1990b), this implies that the eigenperiod of the retaining wall is significantly smaller than that of the standing wave (WL|Delft Hydraulics, 1990b).

In further analysis it is assumed that this is the case, the properties of the retaining wall are changed to accommodate this. A further evaluation of this aspect is given in subsection 7.2.4. Two possible factors in the model that may explain an overestimation of the retaining wall eigenperiod are put forward:

- The added inertia of the retaining wall is overestimated
 - It is noted that the 2D schematization gives a very high estimate (10 times the inertia).
- The estimated spring stiffness that follows from the constant pitch effect analysis may be lower than the spring stiffness of the mode 3 effect.

By reducing the total inertia to double the estimated inertia of the retaining wall without added mass ($\approx 20\%$ of the initial estimate), and the spring stiffness to the originally estimated hydrodynamic stiffness (found in Appendix I), the analysis of the eigenmodes is redone (resulting in Figure 6.8):

- $J + J_{hd} = 7.5 \cdot 10^{10} \text{ kg}\cdot\text{m}^2$
- $k_{hd} = 7.0 \cdot 10^{10} \text{ N}\cdot\text{m}/\text{rad}$

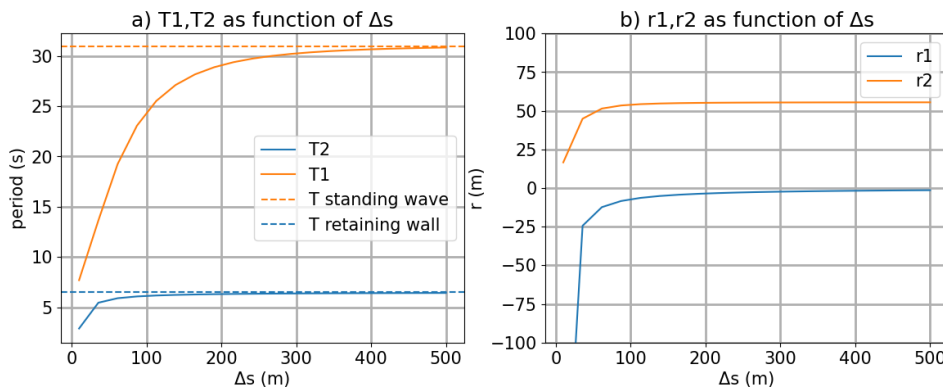


Figure 6.8: T and r as function of parameter Δs , with reduced retaining wall period

The eigenperiod of the retaining wall itself however is now reduced to about 6 seconds. The eigenmode with the period corresponding to the standing wave now has an eigenvector that matches the mode 3 effect, with the expected coupling of water level deviation and retaining wall pitch.

Results: general solution

In the following paragraphs, the properties of the system including the damping matrix are considered, to assess the possibility of instability of the system.

In the case of this damped system the eigenmodes are expected to show the two degrees of freedom to move at the same frequency, but a phase shift between the two may be present, furthermore the oscillation is expected to dampen or grow over time. The given extension of Equation 6.7 satisfies this:

$$\begin{bmatrix} \theta(t) \\ h_1(t) \end{bmatrix} = \begin{bmatrix} 1 \\ r \end{bmatrix} \cdot \begin{bmatrix} \exp([\alpha + i\omega]t) \\ \exp([\alpha + i\omega]t + i\varphi) \end{bmatrix} \quad (6.10)$$

Substituting this form in the governing equations and splitting the imaginary and real parts of the two governing equations into separate equations yields four equations with four unknowns (as expected for a second order two degree of freedom system):

- ω (rad/s): angular frequency
- $[1, r]$: Eigenvector describing magnitude of h_1 (meters) relative to θ (rad)
- α (-): exponential growth factor
- φ (rad): phase shift of h_1 relative to θ

Supporting reasoning for this analysis method, and the presented solution form, is given in Appendix K.

The mode 3 effect is, in this analysis, considered as a phenomenon related to instability. If this holds, it is to be expected that a mode with a period matching the mode 3 effect has a factor $\alpha > 0$ under the situation as observed during the high floating phase (the local head difference as described in Figure 6.6). Furthermore, for the mode 3 effect only a minimal phase shift, φ , is expected (the movement of the water level and retaining wall is observed to be in phase, WL|Delft Hydraulics, 1990b).

In the following paragraphs, the influence of unknown and uncertain parameters on the presented solution form is illustrated, and compared to observations on the mode 3 effect. In the first place, the focus is on the period and stability of the found solution. First, the parameters related to the geometry of the downstream segments ($\Delta s, c_s$) are considered, since these are the most uncertain. A rough estimate of these parameters is made, based on the results of the undamped system. Second, the damping matrix is considered to assess the expected onset of instability. The influence of the damping ratio of the pitching retaining wall, ζ , and the influence of the coefficient c_r in the damping matrix (Equation 6.6) are considered.

Practically, the unknowns in the given general solution are numerically calculated for ranges as identified to be relevant (using the method from Appendix K). For uniformity, each considered range is divided into 100 discrete points, for each of which the properties of the considered solution form are numerically calculated. The parameters in the model are defined as in subsection 5.4.2, except for the spring stiffness and the inertia, these are as redefined based on the results of the system without damping matrix.

The hydraulic conditions are as defined in the quantification step, with the initial head difference taken constant at 0.3 m unless otherwise indicated. Only the mode with the highest period is considered, this mode matches the standing wave as found from analysis of the system without damping matrix (Figure 6.8).

Results: streamwise length and seaward flow

From the analysis of the undamped system (Figure 6.7) it followed that for large values for Δs a standing wave similar to the 1D-standing wave is found. In Equation 6.5 a parameter c_s is introduced to decouple the effect of the storage in the discrete segment and the effect of discharge variations to further downstream. The parameters in the presented solution form are determined for:

- Δs : 30-200 m, chosen based on results from Figure 6.7.
- c_s : 0-1 (-), range from no effect of downstream discharge to the discharge effect estimated in the system derivation (see quantification).

In Figure 6.9, it can be seen that the period is a function of both parameters. Periods that match the expected mode 3 effect can be found, in Figure 6.9 two contour lines are highlighted:

- 31 seconds, the period expected for the one-dimensional standing wave in the discrete model (Equation 5.25).
- 37 seconds, the period of the observed mode 3 effect (Figure 3.8).

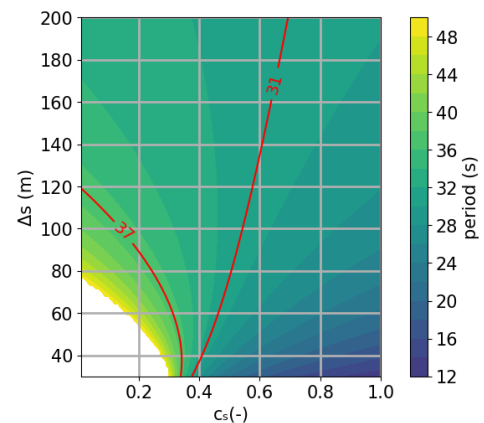


Figure 6.9: Period, $T(2\pi/\omega)$, as function of parameters Δs and c_s (with $\Delta h_0 = 0.3\text{m}$)

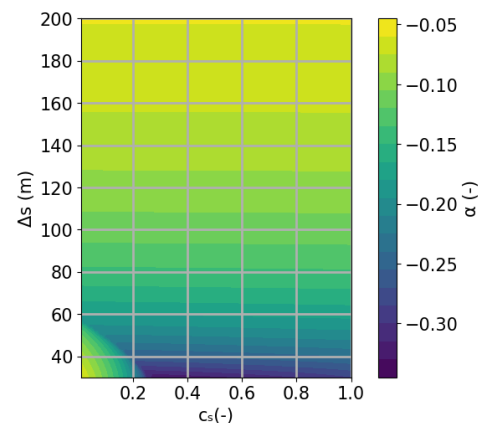


Figure 6.10: α , as function of parameters Δs and c_s (with $\Delta h_0 = 0.3\text{m}$)

For low values of Δs two observations may be made:

- In combination with low values of c_s the period rapidly increases, leading to an area in the $(\Delta s, c_s)$ -plane where the chosen solution form is not valid.
- In combination with high values of c_s the period rapidly decreases to values that appear too low to explain the mode 3 effect. This is inline with results in Figure 6.7.

From these results, calibration for the observed period using Δs and c_s appears to be a possibility. It is however not certain that this is the reason for the observed period of 37 seconds, see subsection 6.1.4.

Regarding Figure 6.10, it can be seen that c_s has little impact on the stability. For increasing values of Δs the system appears to be damped less (bigger value for α).

To avoid the areas with unexpectedly high or low periods in Figure 6.9 the system is further analysed for:

- $\Delta s > 120$ m
- $c_s = 0.4$ (-)

Results: instability onset

To assess the stability of the system the impact of the local head difference, Δh_0 , is considered for the range 0.2 to 7 m (Figure 6.11). This is an unrealistic range, but used to show the head difference at which the model expects instability when the damping matrix is as initially estimated:

- $\zeta_s = 0.05$ (-)
- $c_r = 1.0$ (-)

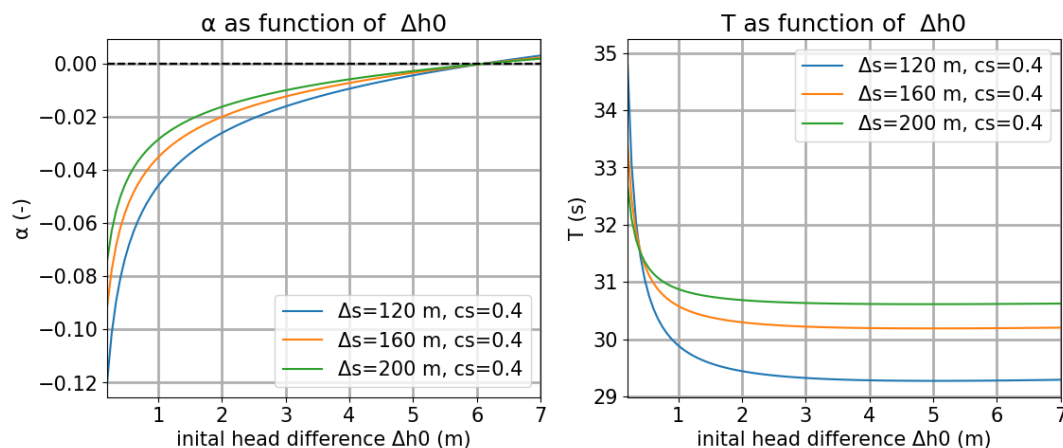


Figure 6.11: Stability and period of the system under varying initial head difference

From Figure 6.11 it is seen that, as expected, the damping decreases for an increasing head difference, and for $\Delta h_0 \approx 6$ m instability is found. However, the system appears stable for the range of head differences where the mode 3 effect is observed, 0.25-0.6 m (Figure 6.6). Furthermore, it can be seen that the head difference has a substantial impact on the period of the mode 3 effect. The mode 3 effect, however, has been observed with a constant period.

Although, as concluded from Figure 6.10, Δs has an impact on the value of α , it does not appear to have an impact on the onset of instability (the head difference where α first exceeds 0). Based on this, the value is chosen to as fixed for further analysis:

- $\Delta s = 120$ m

Results: damping calibration

It appears intuitive that the h_1 related damping term in the matrix C (in blue in Equation 6.6), may be overestimated. An overestimated damping term may explain the overstated impact of Δh_0 on the eigenperiods of the system. The effect of the damping term is assessed with the factor c_s as introduced in Equation 6.6.

An underestimation of the negative damping term (in red in Equation 6.6) could also be theorized, however this seems less likely. In the derivation it was assumed the discharge from upstream reacted directly to changes of the gate position and water level, the terms in the damping matrix are therefore more likely an over than an underestimation.

A calibration of the damping matrix to the observed onset of instability, a situation with a local head difference of 0.25 m (Figure 6.6), is performed. The parameters in the damping matrix, ζ and c_r are analysed to determine a system with parameters such that $\alpha > 0$ for $\Delta h_0 > 0.25$ m.

For both ζ and c_r , the range from 0 (no damping effect) to 1 is considered. This results in Figure 6.12, the contour line $\alpha = 0$ is highlighted.

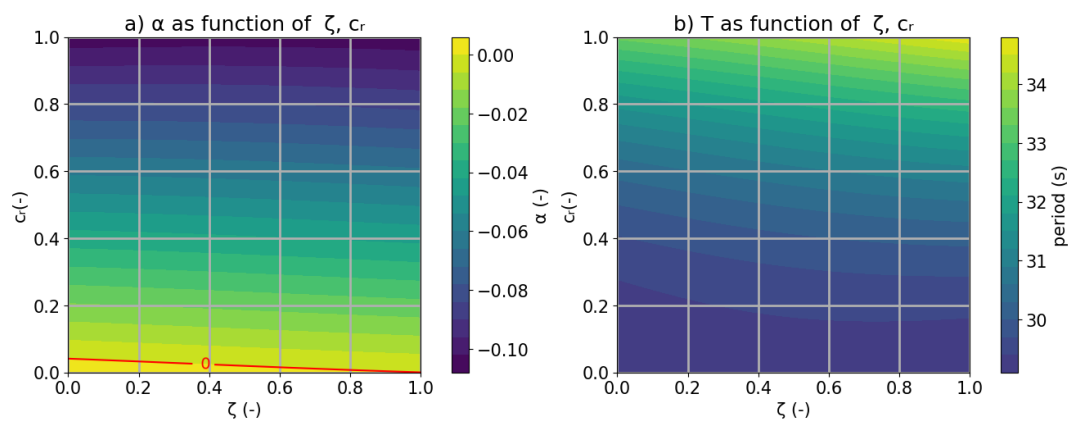


Figure 6.12: Stability and period of the system under varying initial head difference and c_r with $\Delta s = 120$ m and $c_s = 0.4$

From Figure 6.12 it can be seen that for unexpectedly small values of the parameter c_r the system may show instability ($\alpha > 0$), further analysis of the results shows that at $\zeta = 0.05$, $c_r = 0.04$ provides an onset of instability at $\Delta h_0 = 0.25$ m.

Results: summary

The analysis of the model parameters gives a choice of parameters which yield an effect with characteristics similar to the observed mode 3 effect. The parameters as derived in this subsection are:

- $\Delta s = 120$ m
- $c_s = 0.4$ (-)
- $c_r = 0.04$ (-)
- $\zeta = 0.05$ (-)

The characteristics of the general solution, (Equation 6.10), that follow from these parameters are given in Figure 6.13 as a function of the head difference range that follows from the quantification. α increases for an increasing head difference, exceeding 0 for a head difference bigger than 0.25 m. The other parameters are hardly influenced by a change of head difference, and the retaining wall pitch and water level movement are in phase.

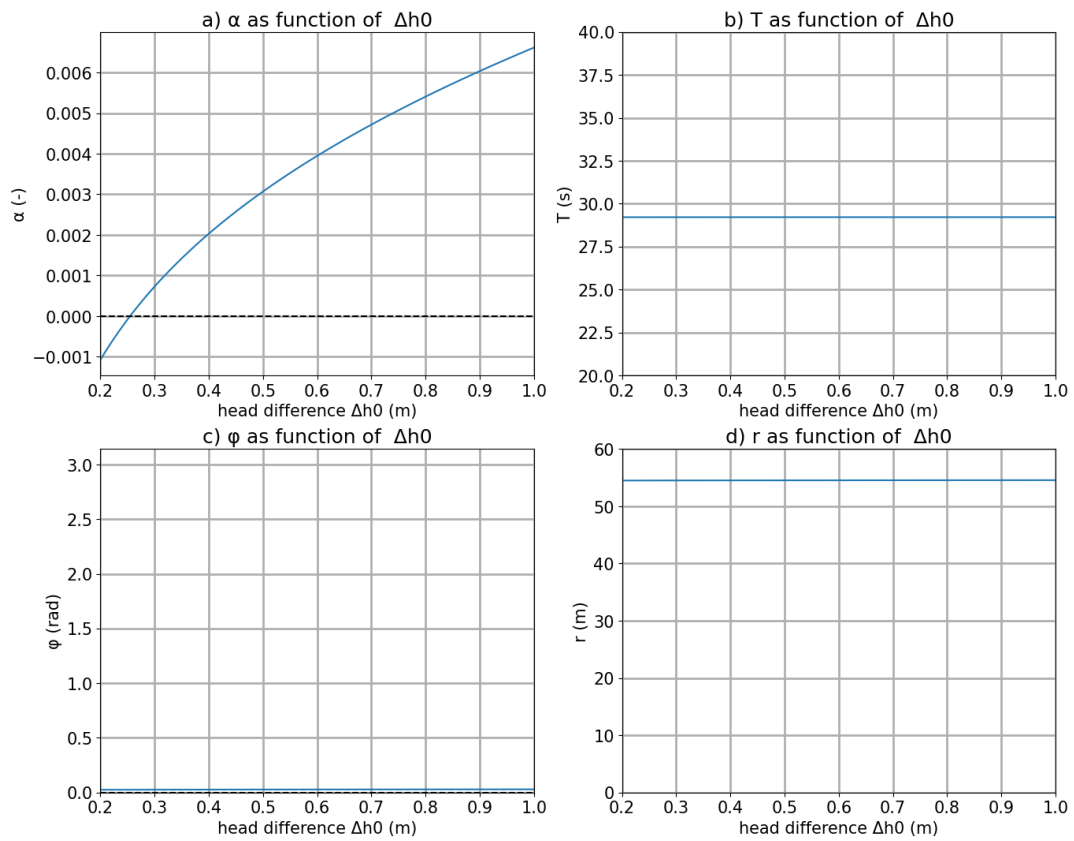


Figure 6.13: Parameters of estimated model as function of Δh_0

6.1.4. Evaluation

The considered conceptual models are summarized in Table 6.2. For each model, the R^2 -score and included variables are given. The mode 3 model gives no predictions on the magnitude of the effect and is not included in Table 6.2.

The different models have a different number of input variables and, there is uncertainty associated with R^2 (no statistical significance tests are applied), the comparison between the different models based on R^2 should be seen as indicative.

Effect	Type	R ²	Input
Mystery force	Hydrostatic model balance	-0.86	Discharge, seaside water level, vertical flow gap
	Momentum balance	0.64	Discharge, seaside water level, vertical flow gap
	Fitted momentum balance	0.71	Discharge, seaside water level, vertical flow gap
	Momentum balance and water level variation	0.14	Discharge, seaside water level, vertical flow gap, trim effect
	Momentum balance and suction force effect	0.63	Discharge, seaside water level, vertical flow gap, trim angle
Trim effect	Hydrostatic stiffness	-5.82	Observed mystery force
	Empiric stiffness	0.69	Observed mystery force
	Empiric stiffness	0.86	Momentum balance Mystery force

Table 6.2: R² parameter of the different conceptual models

Mystery force

The hydrostatic model for the mystery force has a negative R²-score. As seen in Figure 6.2, the predicted magnitude of the mystery force is about half of the observed force. The momentum balance model provides values closer to the mystery force, a fit through the discharge coefficient further increases the quality of the momentum balance model. A relation with effects due to a water level variation or the suction force has not been established, either through the initial estimate of the effect (the value presented in Table 6.2) or through a regression fit in which a reduction factor was considered to correct the initial estimate (subsection 6.1.1).

Trim effect

Regarding the trim effect, the proposed model does not give a full physical basis for the observations. The trim effect is underestimated by a factor 10, leading to the extremely low R²-score in Table 6.2. A regression fit for the stiffness of the retaining wall in pitch leads to a model with a R²-score comparable to the best conceptual model for the mystery force. When the momentum balance model for the mystery force is used as input, instead of the observed mystery force, the R²-score further increases.

It is relevant to assess whether this empiric fit for the stiffness can be supported with physical reasoning, to this end different aspects are considered in the discussion of the trim effect model in subsection 7.2.3. Considered are the impact of the schematized geometry on the hydrodynamic stiffness and effects due to a cross-sectional water variation and a suction force, and whether they may be modelled with the empirically derived stiffness as done in subsection 6.1.2.

Mode 3 effect

The conceptual model detailed for the mode 3 effect results in a system of differential equations that, under certain conditions, can have unstable periodic solutions such that an oscillation with a period and modal shape similar to the standing wave (as expected for the mode 3 effect, see section 2.5) may occur.

Model parameters Δs and c_s , together, play an important role in the period of the system (subsection 6.1.3). Calibration of these parameters may result in a system with the observed mode 3 period of 37 seconds. Not considered physical effects may play a role in the physical explanation of the observed mode 3 period, such as the length of the retaining walls, and effects due to the parking docks or the bed geometry. Furthermore, it is a possibility that the values of Δs and c_s that best describe the system are not constant, they may be a function of the hydraulic conditions. A more fundamental critique is, that the parameters, Δs and c_s , follow from the used schematization. In a more nuanced schematization, where the downstream basin is modelled with a large number of discrete segments, these parameters do not play a role, this is further detailed in subsection 7.2.4.

The coefficients ζ and c_r (on the diagonals of the damping matrix C) are calibrated such that the model becomes unstable at a head difference of 0.25 m, the approximate local head difference at which onset of the mode 3 effect is expected (Figure 6.6). This calibration leads to an unexpectedly low value for c_r (see subsection 7.2.4), i.e. the expected damping effects need to be significantly reduced to explain the occurrence of the mode 3 effect. Again, a more nuanced schematization of the downstream basin may play a role. Furthermore, the response of the discharge under the retaining walls to changes in the system is important for the onset of instability (section 5.4, subsection 6.1.3), suggestions for the description of this discharge are further detailed in subsection 7.2.4.

The conceptual model does not consider any factors that limit the growth of the mode 3 effect, in case it occurs it may grow in magnitude indefinitely. In subsection 7.2.4 it is treated how, a better description of the downstream basin may play a role in modelling the effect with a limited magnitude.

6.2. Statistical models

6.2.1. Evaluation

In this subsection, it is considered whether the statistical models from chapter 4 can be used in addition to the conceptual models, to obtain more complete estimates for the effects in extreme conditions. To this end, the relevant statistical and empirical models, from chapter 4, are summarized in Table 6.3. Given are the type of relation, R^2 -score, and the input variables. The linear relations with the observed global head difference, Rhine discharge, and wind speed, which yielded very weak relations (section 4.2) are not considered in Table 6.3.

Regarding the empirical relations with the local discharge, only relations with the discharge squared are given, as this relates to the local head difference. For the mystery force and trim effect, the model without intercept is considered. For the mode 3 effect, the model including intercept is given, since it scored considerably than the model without intercept.

Effect	Type	R^2	Input
Mystery force	Single, linear	0.66	River side water level change
	Multiple, linear	0.79	River side water level change, seaside tidal range
	Single, squared	0.65	Local discharge
Trim effect	Single, linear	0.86	River side water level change
	Single, squared	0.82	Local discharge
Mode 3 effect (trim angle)	Single, linear	0.69	River side water level change
	Single, exponential	0.86	River side water level change
	Single, parabolic	0.93	River side water level change
	Single, squared	0.63	Local discharge

Table 6.3: R^2 -score of the different statistical models

Mystery force

The statistical models on the mystery force, in general, score lower than the other models in Table 6.3. The multiple regression for the mystery force did yield an improvement for R^2 , but this value was not replicated by the conceptual models, and as such this increase in R^2 is not supported with physical arguments.

It is concluded that regarding the mystery force, the statistical models have limited value compared to the conceptual momentum balance model. However, the discharge squared model is considered in the extrapolation step, in addition to the conceptual model, since this model has also been considered in earlier research. This gives more context to the extrapolation of the conceptual model.

Regarding possible causes for the low R^2 -score, the low data quality of the mystery force models is discussed in subsection 7.1.1. Another reason for low quality of the found relations may be dependence of the mystery force on variables that are not considered in the analyses in this report. An example of variables not considered are those describing wind waves. However, there is no direct indication to assume that low period waves, such as wind waves, play a role in a quasi-constant effect, such as the mystery force.

Trim effect

The statistical trim effect relation has the same R^2 -score as the conceptual model with the fitted spring stiffness (see Table 6.2). No multivariate relations with a higher R^2 -score have been discerned. From the conceptual model, the relation with loading of the retaining wall is only partly explained (subsection 6.1.4). In this report, the empirical fit to the discharge is considered, to avoid the suggestion that a complete conceptual model is given for the trim effect.

Mode 3 effect

The mode 3 magnitude is not explained by the described conceptual model, for this reason the use of statistical relations is required for this effect. For the mode 3 effect, the non-linear relations yield the highest R^2 -scores.

Based on the considered non-linear relations a limited maximum for the magnitude of the mode 3 effect is expected, however a detailed look at the value of this maximum is not yet given. To do this, a logistic curve is considered, of a shape similar to the earlier models, with a plateau limiting the maximum magnitude. The assumed existence of a limited maximum is based on a limited number of data points. For an overview of the expected magnitude in extreme conditions it is relevant to assess whether a growing magnitude may be expected, this is considered with the discharge squared model.

6.3. Extreme conditions

Based on models selected through the model evaluation (subsection 6.1.4, 6.2) an extrapolation of the different effects is presented. These extrapolations give some insight in the expected magnitude of the different effects in extreme situations. In the final conclusions of this report this extrapolation is used to conclude whether exceedance of tolerance limits of the barrier, for the different effects, can be expected.

The models that follow from the given evaluation are summarized in Table 6.4, and follow from the model evaluation in subsection 6.1.4 and section 6.2.

	Model	Input variables	Fitted parameter
Mystery force	Empiric discharge squared model	Discharge (Q)	Empiric coefficient (β_1)
	Momentum balance model	Discharge (Q), flow gap (d), water level (d_s)	Discharge coefficient (μ)
Trim effect	Empiric discharge squared model	Discharge (Q)	Empiric coefficient (β_1)
Mode 3 effect	Logistic model	River side water level change (x)	(multiple)
	Empiric discharge squared model	Discharge (Q)	Empiric coefficient (β_1)

Table 6.4: models considered to for effects extrapolation

In preceding analyses, the uncertainty of the model parameters has been considered for the different models. In the extrapolation in this chapter the expected extreme conditions (discharge, water level) are a different, distinct from the previous, source of uncertainty. Both of these types of uncertainty are considered in this section. To include uncertainty in the relevant extremes, the effects are plotted for a range of hydraulic conditions. Uncertainty intervals for the models, obtained in previous chapters, are given to illustrate the uncertainty in the fitted parameters.

Based on the results, including a consideration of both described types of uncertainty, an indicative judgement is given on the maximum magnitude of the effects. The focus is on the mystery force, for which the conceptual model appears the most complete. For the trim effect, the extrapolation is more uncertain since no complete physical basis is established using the conceptual model.

For the mode 3 effect, no definitive conclusions on the magnitude in extreme situations are given. In line with the evaluation in section 6.2, it is assessed if a clear statistical upper bound of the mode 3 magnitude can be identified using a model with a logistic curve, similar to the plateau derived in subsection 4.4.1, and whether models that instead predict further growth of the mode 3 magnitude may be relevant.

6.3.1. Input variables

Discharge

Earlier estimations for the seaward discharge at the barrier yielded a discharge of about 18,500 m³/s (Rijkswaterstaat, 2009), with an estimated chance of 10⁻⁶ per year. The discharge 18,500 m³/s is considered as reference point, for which the magnitude of the effects is determined. For a further overview, the considered extrapolations are presented for the discharge range from 0-20,000 m³/s.

The method used to obtain the extreme discharge presented above has limitations. First, only a limited set of possible storm conditions is considered. Second, it is unclear if or how the probability of a long waiting period before the retaining walls are moved back into the parking docks is included in the used models. This is a relevant aspect, since this may impact the maximum seaward discharge experienced by the floating retaining walls.

Water level

The seaside water level and vertical flow gap under the barrier in extreme conditions play a role in the momentum balance model for the mystery force. These two quantities are related, the vertical flow gap under the retaining wall is governed by the seaside water level, due to the floating aspect retaining walls. From the test closures, it appears that the relevant value for the two parameters is the local minimum in the water level that is found after the closure (subsection 3.6.2).

The minimum seaside water level and flow gap during situations with extreme seaward discharges may differ from the observations during the test closures. Causes of this may be an impact of wind-set up that is still present for hours after the storm peak, and through a build up of water behind the barrier due to a high river discharge. No analysis of the water level under extreme conditions are known, instead an estimation is made for the seaside water level from which the vertical flow gap is derived.

The sea and river side water levels during the 2018 storm closure are shown in Figure 6.14. The low tide directly after the high water peak has a local minimum above 0 m NAP, only the second low tide after the surge reached values comparable to the astronomical tide without wind induced setup. In terms of peak water level and river discharge, the 2018 closure was not extreme, with a high water peak of +2.7 m NAP and a Rhine discharge of about 4,000 m³/s. More extreme values of these factors, which are expected in case of a high seaward discharge (Rijkswaterstaat, 2009), may be associated with a further increase of the low water level observed after the high water peak.

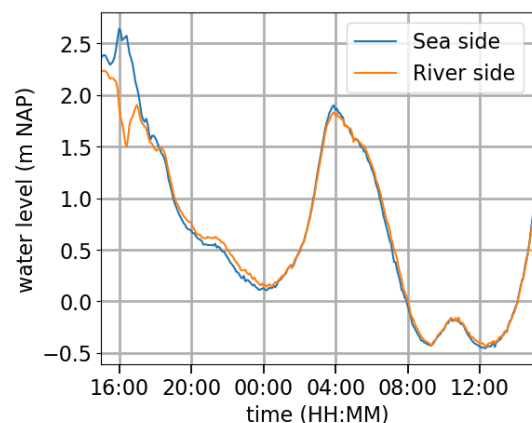


Figure 6.14: Sea and river side water level after the high water peak (2018 storm closure)

Two possible scenarios, regarding the water level, are considered, one with the seaside water level at peak discharge at +0 m NAP, comparable to the local minimum observed during the 2018 test closure. A second scenario with a more extreme seaside water level at +2 m NAP is considered, however it is noted that such a water level may be an overestimation.

Based on the observed relation of the minimum seaside water level and the corresponding vertical flow gap during the test closures, the flow gap for the two scenarios is derived, see Table 6.5. The seaside depth, d_s , follows from the assumed average depth at -17 m NAP (Figure H.4).

	Sea level (m NAP)	Flow gap, d (m)	Seaside depth, d_s (m)
Test closure observations (mean)	-0.6	9.9	16.4
Scenario +0 m NAP	0.0	10.5	17.0
Scenario +2 m NAP	2.0	12.5	19.0

Table 6.5: Considered scenarios for momentum balance modes

Local head difference

From the expected discharge and two scenarios regarding the water levels the local head difference can be given, see Figure 6.15, as calculated from Equation H.1 (with the contraction coefficient as obtained in Table 6.1):

$$\Delta h = \left(\frac{Q}{\mu_{est} \cdot B \cdot d} \right)^2 \cdot \frac{1}{2g} \tag{6.11}$$

With:

- $\mu_{est} = 0.68$ (-): estimated contraction
- $B = 360$ m: waterway width
- d (m): vertical flow gap under gate
- $g = 9.81$ m/s²: gravitational constant

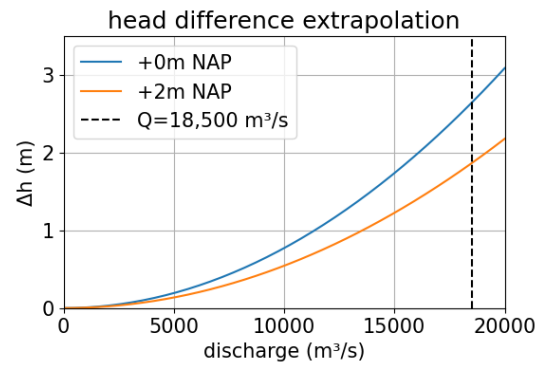


Figure 6.15: Head difference as calculated for the considered discharge range

6.3.2. Mystery Force

The models are not treated in detail in this section. The empirical discharge squared model is treated in section 4.5. The momentum balance model is defined in section 5.2.

The mystery force according to the different models in Table 6.4 is given in Figure 6.16. The uncertainty interval for the different models is indicated for the 90%-confidence interval of the estimated slope parameter (empirical model) and of the contraction coefficient μ (momentum balance model).

The dashed vertical line indicates the earlier noted extreme discharge of 18,500 m³/s, the range of the results at 18,500 m³/s is 2,300-5,400 kN. The found uncertainty interval for the different models is supported by a resampling of the dataset given in Appendix L.

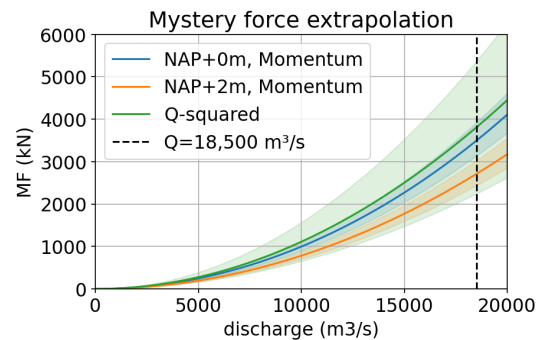


Figure 6.16: Mystery force models extrapolated for extreme discharges

6.3.3. Trim effect

The trim effect is extrapolated for the identified discharge range, using the empirical fit with the local discharge squared found in section 4.5. The uncertainty in the model is based on the found confidence interval for the slope parameter. The extrapolated trim effect, presented in Figure 6.17, has a range of 7.5-13 milliradians at 18,500 m³/s.

6.3.4. Mode 3 effect

The observed mode 3 magnitude is modelled well with exponential and parabolic relations of a shape such that they have a limited maximum magnitude (Figure 4.9). It is unclear if these models can be extrapolated to extreme situations, supporting reasoning from the conceptual model is missing.

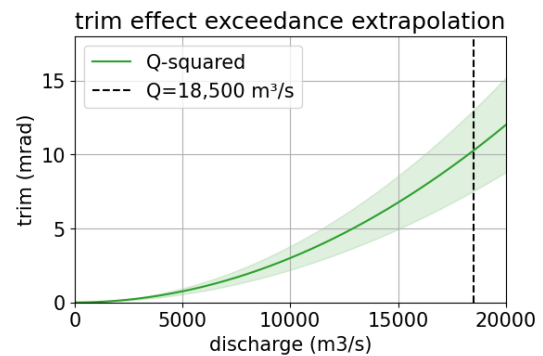


Figure 6.17: Trim angle model extrapolated based on the empirical discharge squared model

To elaborate on the uncertainty of the extrapolation, two alternative fits to the mode 3 effect are considered. A logistic fit is used to formulate an upper bound, provided that for further extrapolation the plateau holds. The empirical fit with the local discharge squared to consider, to assess if the plateauing model may be a misinterpretation based on the limited size of the dataset, and that instead a growing amplitude may be expected. This is relevant, since this would lead to a big mode 3 amplitude.

Logistic model

A logistic curve is considered as fit to the observed data (as suggested in subsection 4.4.1). From this, an upper bound for the height of the plateau found in the original models is considered. To approximate uncertainty intervals of the fitted parameters, the jackknife resampling is used, explained in the text box on the next page.

Jackknife resampling

The jackknife resampling method gives a simple technique which uses resampling of the original data set to obtain estimates for the regression parameters, and their uncertainty. Description of this method is based on Sahinler and Topuz, 2007.

Using the jackknife resampling technique, the fit for a dataset with n entries is done n times. For each of these fits, one of the entries in the data set is disregarded. For each model parameter, β , this leads to n different estimates. A final estimate for the parameters is obtained by taking the mean of the set of estimated parameters (Sahinler & Topuz, 2007):

$$\hat{\beta} = \frac{1}{n} \sum_{i=1}^n \hat{\beta}_i \quad (6.12)$$

The 90%-confidence interval according to the jackknife resampling is found by taking the standard error of the estimated set of parameters, and combining this with the appropriate t -distribution (similar to the confidence interval obtained earlier, where the standard error was found through assumed normality of the linear regression errors) (Sahinler & Topuz, 2007):

$$\hat{\beta} - s_{\hat{\beta}} \cdot t_{\text{dof},5\%} > \beta < \hat{\beta} + s_{\hat{\beta}} \cdot t_{\text{dof},95\%} \quad (6.13)$$

With $s_{\hat{\beta}}$ indicating the standard error of the estimated set of parameters. The jackknife standard error is derived from the jackknife variance (Sahinler & Topuz, 2007):

$$\text{var}(\hat{\beta}) = \frac{n-1}{n} \sum_{i=1}^n (\hat{\beta}_i - \hat{\beta})^2, s_{\hat{\beta}} = \sqrt{\text{var}(\hat{\beta})} \quad (6.14)$$

$t_{\text{dof},\alpha}$ indicates the critical values of the appropriate t -distribution.

The used logistic function has the shape (Rzdkowski & Sobczak, 2020):

$$W^2 = \frac{A}{1 + \exp[k(x - x_0)]} \quad (6.15)$$

With:

- x (m): Independent variable, water level change
- A (10^{-8} rad^2): The value of the plateau
- x_0 (m): Midpoint of the S-shape
- k (-): Parameter for steepness of the S-shape
- W^2 (10^{-8} rad^2): Mode 3 magnitude

The logistic fits to the mode 3 effect in the trim angle, following from the jackknife resampling, are shown in Figure 6.18. The mean of the estimated fits is included, and is with an R^2 -score of 0.92 score comparable to the earlier fits.

Based on the 90% confidence interval derived from the fits, the upper bound of the estimated plateau has a mode 3 variance of $3.25 \cdot 10^{-8} \text{ rad}$ (from a t -distribution based on the standard error of the set of fitted parameters). For reference, the mean and confidence intervals of all logistic fit parameters are given in Table 6.6.

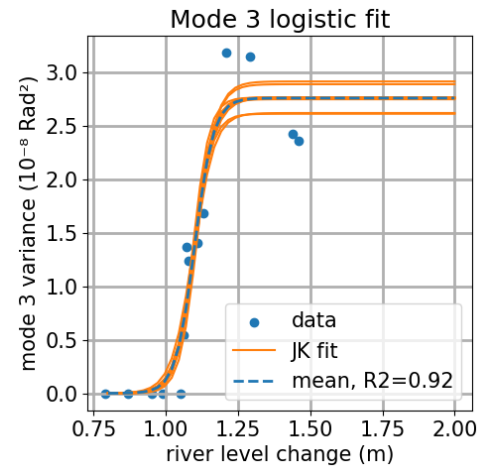


Figure 6.18: Logistic fits to the mode 3 data using jackknife resampling

	mean	5%	95%
A	2.76	2.27	3.25
x_0	1.10	1.08	1.12
k	30.4	16.4	44.4

Table 6.6: Logistic model parameters

Based on this, it can be concluded that the logistic model, including uncertainty, gives no indication for problematic magnitudes of the mode 3 effect (the derived confidence interval does not give values of the plateau much higher than observed).

Parabolic growth model

Earlier research pointed toward increased mode 3 effects for higher head differences (WL|Delft Hydraulics, 1990b). To consider this, the empiric fit with the local discharge squared is considered, as in section 4.5:

$$W^2 = \beta_1 \cdot Q^2 + \beta_2 \quad (6.16)$$

With β_1 the fitted slope parameter and β_2 the fitted intercept.

The fits are shown in Figure 6.19. Visually, the fit appears worse than the logistic model. This is reflected by the low R^2 -score of 0.40. Based on this low score, the maximum expected mode 3 amplitude according to the parabolic model, and the obtained parameters are not further considered.

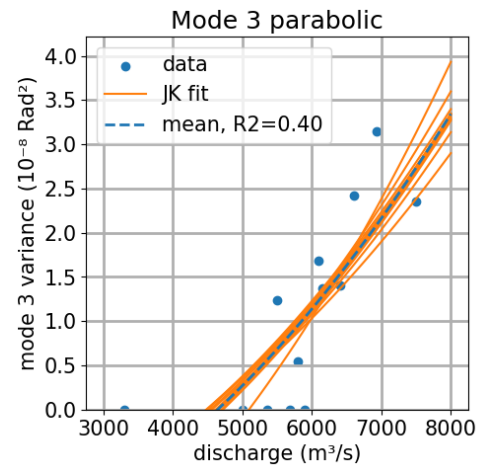


Figure 6.19: Parabolic fits to the mode 3 data using jackknife resample

6.4. Summary

In section 6.1 the conceptual models from chapter 5 are tested against the observed effects. The mystery force can be modelled with the momentum balance model (with a R^2 -score of 0.71). The hydrostatic model, and additional effects due to suction force and a water level variation, appear irrelevant for modelling the mystery force. For the trim effect the model with the empirical rotational stiffness to be relevant (with a R^2 -score of 0.86), however this stiffness is not physically explained. For the conceptual mode 3 model a calibration is performed to explain the occurrence of the effect in observed conditions, this calibration is not physically explained. Furthermore, no magnitude of the mode 3 effect is provided by the conceptual model.

In section 6.2 the statistical models from chapter 4 are considered, to see where they supplement the conceptual models. The relation with the local discharge squared is considered relevant for the mystery force and trim effect, since it has been considered before for the mystery force, and scores reasonably well (R^2 -score of 0.65). Statistical relations are relevant for the mode 3 effect, since the conceptual model gives no predictions on the magnitude of this effect.

The models are extrapolated in section 6.3, based on an extreme local discharge of 18,500 m^3/s , of which the chance of occurrence is estimated to be 10^{-6} per year. Extrapolation for the mystery force (subsection 6.3.2) leads to expected forces with a magnitude of 2,300-5,400 kN (including 90%-confidence intervals), see Figure 6.20, where the extrapolations are compared to observations during test closures. For the momentum balance model the extrapolated values depend on the water level, between the two considered scenarios of 0 and +2 m NAP the difference is about 20% (a higher water level leads to a reduced mystery force).

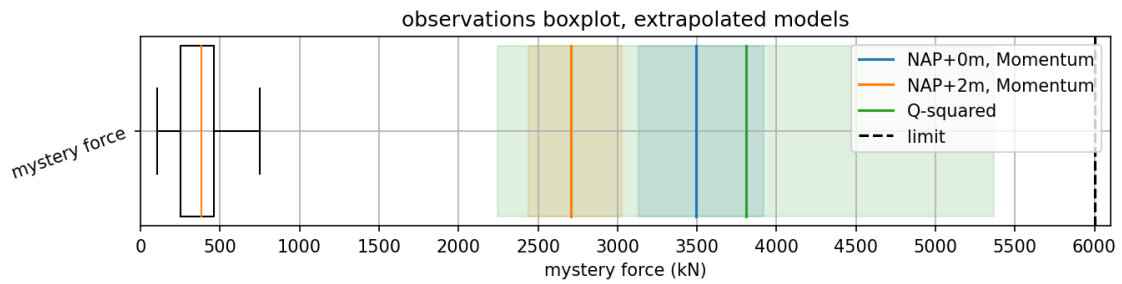


Figure 6.20: Boxplot of the observed mystery force and different model predictions for 18,500 m³/s (from Figure 6.16)

The trim effect is extrapolated based on the empirical discharge squared model, see Figure 6.21. The expected trim effect is 7.5-13 milliradians at 18,500 m³/s.

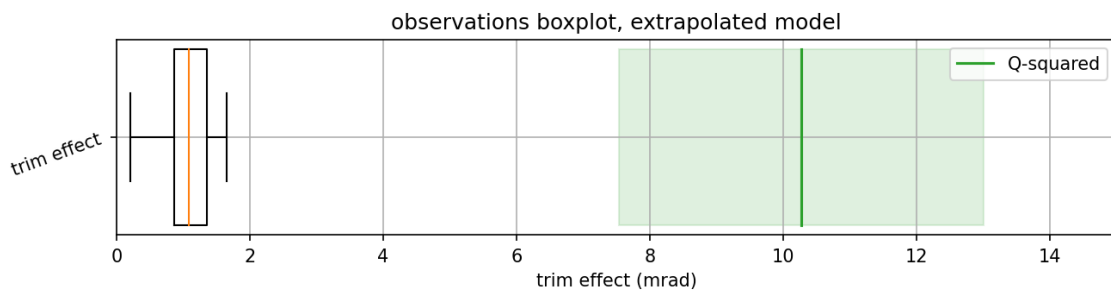


Figure 6.21: Boxplot of the observed trim effect and model predictions for 18,500 m³/s (from Figure 6.17)

Regarding the mode 3 effect, statistical relations with the parameter river level change (defined in Table 3.2) and the local discharge are considered. The logistic model has a limited plateau, if this model is valid, the found plateau would not be exceeded, regardless of the extreme discharge. The logistic fit suggests an upper bound mode 3 variance of $3.25 \cdot 10^{-8} \text{ rad}^2$, and fits the data well (R^2 of 0.92). A model, that grows with the discharge squared, is shown to be a significantly weaker explanation of the mode 3 amplitude. For this reason, this model is not considered for further extrapolation.

Discussion

In the previous chapters, the different seaward flow effects were analysis based on statistical relations and theoretical models. In this chapter, possible shortcomings of the used methods are further discussed.

7.1. Data

7.1.1. Mystery force data

For most closures, the mystery force magnitude is based on a reported value. Variations on a timescale shorter than 5 minutes in the pull/push rod load may be included in this reported mystery force.

To gain insight in the possible contribution of this aspect, a detail of the mystery force data for the 2008 test closure is given (Figure 7.1). Given are the 5-minute average used to find the mystery force in this report and two shorter period moving averages, which show variation on top of the 5-minute average. These variations, when included in the mystery force, induce an error of order 10% in the mystery force magnitude (≈ 40 kN on a mystery force of ≈ 400 kN).

An error of 10% does not invalidate the statistical or conceptual model analysis, but it may play a role in the strength of the relations found.

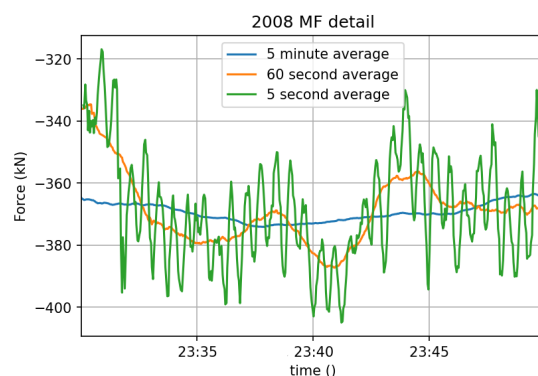


Figure 7.1: Excerpt of the 2008 mystery force data, with three distinct moving averages

7.1.2. Trim angle data

It has been derived that the trim angle data has an approximate resolution of 0.01-0.1 milliradians (Appendix A). The resolution of the trim data, and noise in the signal, limits the minimum mode 3 effect that can be resolved. A threshold variance of 10^{-9} rad² is considered based on these two aspects (subsection 3.5.3). This method appears sufficient for most closures (9 out of 14), as variances in the order of 10^{-8} rad² are observed (Appendix C). It cannot be excluded that this method is inadequate for some closures, which may have a limited mode 3 effect.

The consequences of this appear limited, per definition the magnitude of the effect for these edge cases must be very small. However, it is relevant when assessing, in more detail, at which threshold for hydraulic conditions the mode 3 effects may occur.

7.1.3. Local head difference

An estimation of the local head difference was made for the conceptual models based on the local discharge and the flow gap. The estimation of the local discharge in this report is based on an elementary 1d-schematisation (Equation H.1), and cannot readily be verified by data. The schematization seems somewhat conservative with an assumed width of 360 m (the total length of the circular retaining walls is more than 400 meters, WL|Delft Hydraulics, 1990b), and a contraction coefficient of 0.65 (general literature on submerged underflow weirs suggest values up to 0.8, Voorendt and Molenaar, 2020, p. 76).

Using the equation for the local head difference (Equation H.1) the relative influence of less conservative estimated for the width and contraction coefficient is checked:

$$\begin{aligned} \left(\frac{Q}{\mu \cdot B \cdot d_0}\right)^2 \cdot \frac{1}{2g} &= \left(\frac{Q}{0.65 \cdot 360 \cdot d_0}\right)^2 \cdot \frac{1}{2g} = \Delta h_{\text{baseline}} \\ \left(\frac{Q}{0.65 \cdot 400 \cdot d_0}\right)^2 \cdot \frac{1}{2g} &= \Delta h_B = 0.81 \Delta h_{\text{baseline}} \\ \left(\frac{Q}{0.80 \cdot 360 \cdot d_0}\right)^2 \cdot \frac{1}{2g} &= \Delta h_{\mu} = 0.66 \Delta h_{\text{baseline}} \end{aligned} \quad (7.1)$$

With

- μ (-): contraction coefficient
- B (m): waterway width
- d_0 (m): vertical flow gap under gate
- $g = 9.81 \text{ m/s}^2$: gravitational constant

It can be seen that the local head difference decreases significantly (19-34%), for less conservative parameters. If these are combined, the head difference is 46% lower. It has been demonstrated that the effect of uncertain parameters in the schematisation of Δh_0 is big.

Regarding impact on the results the consequences are smaller, this illustrated with for two most relevant models. For the momentum balance model (which approximately scales with Δh , Table 5.1) it would simply suggest that a larger part of the now smaller total gate load must act as a tangential load to explain the mystery force. For the mode 3 model it would suggest that the effect occurs for an even lower local head difference, the earlier finding that damping effects are overestimated in the defined model would in that case be strengthened further.

7.2. Models

7.2.1. Statistical models

A correlation matrix that gives indications on a larger set of relations is used in this report (Figure 4.7). The focus of this correlation matrix is on describing the hydraulic conditions. The inclusion of the mean wind speed and Rhine discharge in the correlation matrix presents a limited step towards gaining insight in the causal factors behind the strong seaward flow. The presented correlation matrix, therefore, cannot be used for definitive conclusions on the causal factors behind the strong flow.

7.2.2. Statistical model input

One of the main variables in the statistical models is the water level change on the riverside of the barrier (as described in Table 3.2). The relations between this variable and the main flow related variables used in the theoretical models, the local discharge and the local head difference deduced from this discharge, are considered below.

From the full correlation matrix (Appendix E) it can be seen that the river level change shows correlation with the peak local discharge (rank correlation of 0.90). This relation is expected, a relatively big change of water level implies movement of a relatively big quantity of water. This however does not explain why this parameter appears to be a *better* predictor than the local discharge for purely statistical relations.

Aside from the discharge, the low water level plays a role in the deduced local head difference, as it relates to the flow gap under the retaining wall. A high correlation of the water level change with this low water level could explain the strong relations found. However, from the correlation of the river level change and the discharge peak with the low water level (Appendix E) it can be seen that the local discharge peak shows a higher correlation with this low water level, this does not appear to explain the predictive value of the river level change.

For further insight, the relation with the model parameters, the river level change and local discharge per closure, is plotted as function of the local head difference as calculated for the theoretical models (Equation H.1). The overall picture of the two variables is very similar, and no further conclusions are drawn.

It has been demonstrated that indeed the water level change strongly correlates to the variables considered relevant in the theoretical models. However, why the relation is stronger than for the local peak discharge is not cleared up. Lastly, two possible reasons are qualitatively given that may play a role:

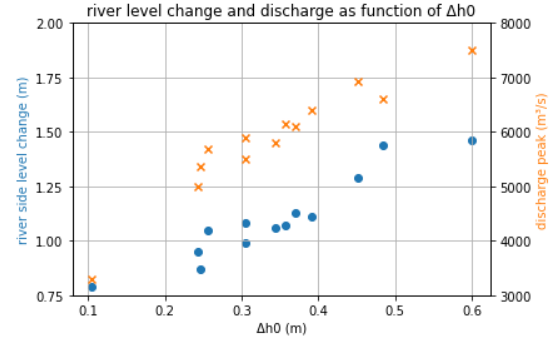


Figure 7.2: River level change and peak discharge as function of the calculated local head difference

- **Statistical significance:** The improvement by the using the river level change over the peak discharge is not statistically significant, i.e. there is no real improvement.
- **Model quality:** The numerical model may not give the relevant peak discharge, due to the 10-minute time step or because of deviations in the model. The river level change is a more direct observation of the system, and the water level has a higher sampling frequency.

7.2.3. Conceptual trim effect model

From analysis the stiffness estimate of the retaining wall in trim appears to be an overestimate, the spring stiffness, as empirically derived from the fit to the observations, is an order 10 smaller. In this section different uncertainties, not explicitly considered in the model definition, are discussed.

Hydrodynamic stiffness

In the conceptual trim effect model, the structure is modelled with two symmetric rectangular gates, a simplification of the sector-gates. The schematized shape impacts the spring stiffness of the retaining wall, which is determined with the following equation (which follows from the analysis as described in Appendix I):

$$k_{hd} \approx \rho g \cdot \frac{1}{12} \cdot b \cdot L^3 \quad (7.2)$$

With:

- $b = 15$ m: retaining wall streamwise width
- $L = 180$ m: retaining wall length
- $g = 9.81$ m/s²: gravitational constant
- $\rho = 1012$ kg/m³: water density

In the schematization, the retaining wall has a length of 180 meters, this is half the canal width. Due to the circular shape, the total length of the retaining wall is longer, approximately 210 meters (estimated from Rijkswaterstaat, n.d.-a). This length increase of 16% leads to a stiffness increase of:

$$k_{hd,+16\%L} = \rho g \cdot \frac{1}{12} \cdot b \cdot (1.16L)^3 = 1.56 \cdot k_{hd} \quad (7.3)$$

This is a 56% increase of the initial estimate. Due to the rounded shape, the retaining wall stiffness using $L = 210$ m is an overestimation (the round shape reduces the effective arm relative to the centre of gravity). The expected stiffness is somewhere between the original estimate and the value derived above.

The width of the retaining wall, b , plays a role in the hydrodynamic stiffness, under a high head difference over the barrier the protrusion on the riverside of the barrier could potentially be submerged (see Figure 7.3). The rotational stiffness scales linearly with the width, b (Equation 1.2). For the situations with the width b_2 , as in Figure 7.3, the stiffness reduces by a factor 2-3, compared to the original value, b_1 .

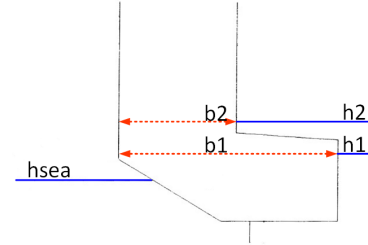


Figure 7.3: illustration of change of width b due to a change of the upstream water level

Suction force

The distribution of the suction force over the retaining wall is unknown, and related to the distribution of the flow velocity over the cross-section. In this analysis, it is assumed that the total hydraulic head near the bank and in the middle of the river is equal, but that between these two points a difference in flow velocity is present. This assumption leads to a difference in pressure head, $\Delta h_{\text{suction}}$, over the cross-section, which loads the retaining wall in pitch. The relation between $\Delta h_{\text{suction}}$ and the difference in velocity head over the cross-section is described from Bernoulli's law:

$$u_{\text{bank}}^2 + 2 \cdot g \cdot \Delta h_{\text{suction}} = u_{\text{river}}^2 \Rightarrow u_{\text{river}} = \sqrt{u_{\text{bank}}^2 + 2 \cdot g \cdot \Delta h_{\text{suction}}} \quad (7.4)$$

with:

- u_{bank} (m/s): flow velocity near the bank
- u_{river} (m/s): flow velocity in the middle of the waterway
- $\Delta h_{\text{suction}}$ (m): Differential pressure head over retaining wall length
- $g = 9.81$ m/s²: gravitational constant

For simplicity the variation of the velocity head over the cross-section is modelled with a triangular distribution, with the peak magnitude, $\Delta h_{\text{suction}}$, in the middle of the waterway (Figure 7.4).

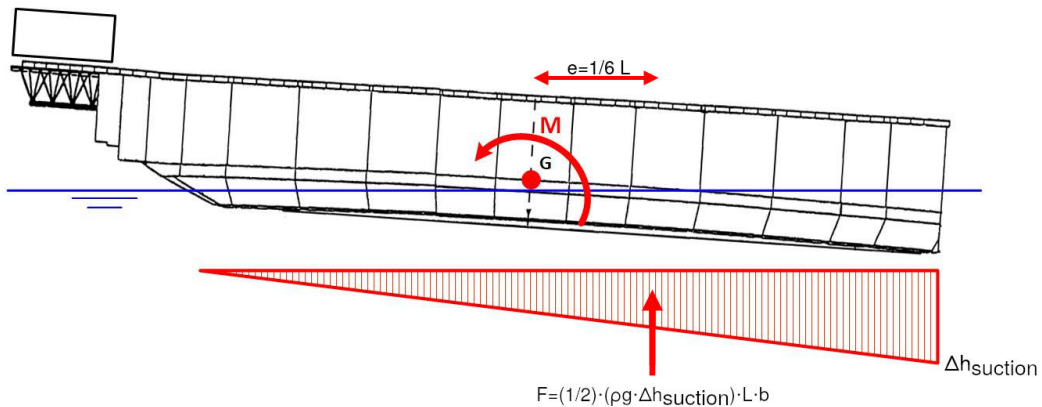


Figure 7.4: illustration of pressure head differential induced by differential flow velocity

The moment acting on the retaining wall in pitch as schematized in Figure 7.4 is:

$$M_{\text{suction}} = F_{\text{suction}} \cdot e_{\text{suction}} = \left(\frac{1}{2} \cdot \rho g \cdot \Delta h_{\text{suction}} \cdot L \cdot b \right) \cdot \frac{1}{6} L \quad (7.5)$$

With:

- $\Delta h_{\text{suction}}$ (m): Differential pressure head over retaining wall length
- $b = 15$ m: retaining wall streamwise width
- $L = 180$ m: retaining wall length
- $g = 9.81$ m/s²: gravitational constant
- $\rho = 1012$ kg/m³: water density

The load in pitch due to the mystery force has the following order of magnitude (using the median mystery force, and arm as follows from Equation 6.3):

$$M_{\text{MF,median}} = F_{\text{MF,median}} \cdot e = 380 \text{ kN} \cdot 20 \text{ m} \approx 8000 \text{ kNm} \quad (7.6)$$

The value of $\Delta h_{\text{suction}}$, corresponding to a moment of 8,000 kNm, is calculated from Equation 7.5 to be 0.02 m. For a moment that is 10 times bigger $\Delta h_{\text{suction}}$ is 0.2 m. If it is assumed that near the bank the flow velocity is 2.0 m/s, the flow velocity for these two values of $\Delta h_{\text{suction}}$ is:

$$\begin{aligned} u_{\text{river},0.02} &= \sqrt{2.0^2 + 2 \cdot g \cdot 0.02} = 2.1 \text{ m/s} \\ u_{\text{river},0.20} &= \sqrt{2.0^2 + 2 \cdot g \cdot 0.20} = 2.8 \text{ m/s} \end{aligned} \quad (7.7)$$

A change in flow velocity between 0.1-0.8 m/s over the cross-section does not appear unrealistic, and therefore influence of the suction force on the trim effect cannot be excluded.

The suction force relates to the square of the flow velocity, which has a linear relation with the local head difference (see also section H.5). This may explain why the empirical relation with the mystery force, which has a similar relationship with the head difference, models the effect well. The extrapolation of the trim effect is therefore expected to remain valid.

Water level variation

A water level variation over the cross-section may explain the trim effect without considering any extra loading of the retaining wall in pitch, or an unrealistically low rotational stiffness. To make the case that the water level variation plays a significant role in the trim effect, explanation of the discrepancy with the mystery force models may be considered. In the analysis of the mystery force, using the conceptual models, no effect due to a water level variation could be discerned (subsection 6.1.1). Alternatively, additional observations on the water level could provide direct evidence of this effect.

7.2.4. Conceptual mode 3 model

Retaining wall eigenperiod

In the conceptual mode 3 model, the retaining wall is modelled as a pitching object, which consequently has an eigenperiod. For this conceptual model, the inertia and stiffness of the retaining wall are amended such that the eigenperiod of the pitching retaining wall is significantly lower than the period of the standing wave (subsection 6.1.3).

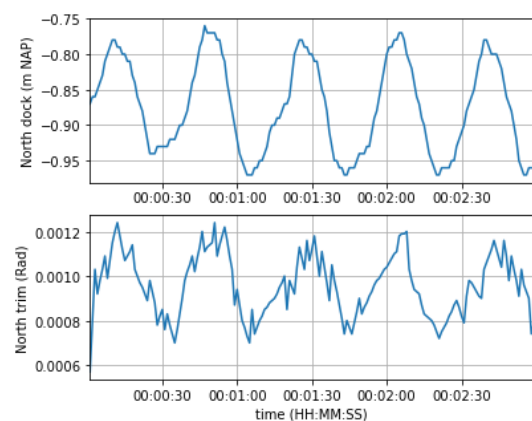


Figure 7.5: Excerpt of the 2008 data, to illustrate the phase correspondence of the trim angle and water level signal

This model choice is supported by the observed in-phase movement of the water level in the parking and the retaining wall trim angle, which is not to be expected if the eigenperiod of the retaining wall is bigger than that of the standing wave (Figure 7.5). Furthermore, an eigenperiod in pitch of 10-11 seconds is found for the retaining wall over a wide range of vertical flow gaps in the physical tests (WL|Delft Hydraulics, 1990b, see Figure 7.6).

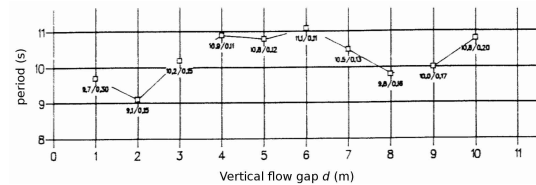


Figure 7.6: Eigenperiod of the retaining wall in pitch as function of the vertical flow gap, found in 3d model test with the numbers representing (period/damping ratio) (WL|Delft Hydraulics, 1990b)

This model choice is further supported by oscillations of the retaining wall with a period of roughly 4-8 seconds towards the end of the high floating phase (not quantified in this report, but visible in the wavelet analysis in, for example, Figure D.7). This is presumably related to movements in the pitch or heave eigenperiods (Duvivier & Nederend, 2013). Some physical tests showed a sudden decrease of the pitch and heave eigenperiods when fully floating (WL|Delft Hydraulics, 1990b), which explains the observed period of 4-8 seconds in relation to the results in Figure 7.6.

Model extension

In the conceptual mode 3 model, a limited description of the flow at the barrier is considered. In the next two paragraphs, it is treated how two of the applied schematizations play a role in the obtained results. In anticipation of the recommendations in chapter 8, it is treated how the model may be extended to give a better description of flow at the barrier.

Retaining wall discharge variation

The mode 3 effect is treated as an instability caused by the terms in the damping matrix of the derived system (Equation 6.6). Two terms in this damping matrix describe how the discharge under the retaining wall is influenced by changes of the system (one for the downstream water level movement h_1 , and one for retaining wall pitch θ). The term related to h_1 has a damping effect, the term related to θ has an opposite effect. This follows from the description of the discharge as used in the design phase (BMK, 1992b), which is based on Torricelli's law (treated in Equation 5.7 to Equation 5.13).

From analysis of the conceptual mode 3 model, it followed that the observed effect could only be explained by a significant reduction of the water level related damping factor in the damping matrix, a finding which lacks supporting physical reasoning.

To get further insight in the behaviour of the flow under the retaining wall, the alternative of a momentum balance and continuity equation of the volume under the retaining wall may be considered, illustrated in Figure 7.7). The flow under the retaining wall can then be seen as analogous to incompressible flow in pipes, where movement of the retaining wall due to a hydrostatic pressure change is analogous to expansion of a pipe wall. The effect of the downstream water level, which acts at the downstream end of the control volume, now has a different influence on the discharge, since the discharge responds with inertia.

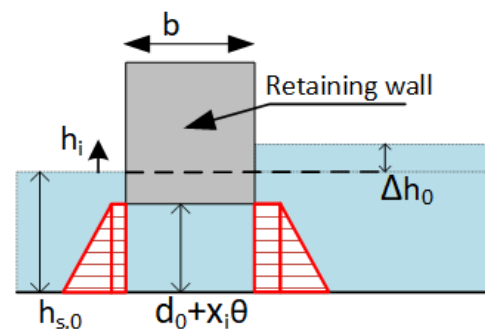


Figure 7.7: Control volume under retaining wall with hydrostatic pressure illustrated in red, with definitions as in Figure H.7

Downstream basin

The downstream basin is described with two discrete segments, this system has solutions that show a mode 3 effect which grows towards an infinite amplitude. The wave directly in front of the barrier can, in reality, be expected to propagate further downstream as a propagating wave, with the same phase speed as the standing wave. Through this, the wave directly in front of the barrier loses momentum, and thus a limiting effect on the mode 3 wave can be expected.

The mode 3 is an effect in a 2-dimensional basin which over the cross-section looks like a standing wave, but also has a propagating effect in streamwise direction. A snapshot of what the wave pattern in the downstream basin may look like is illustrated in Figure 7.8. The propagating effect towards downstream is modelled with the same wavelength as the standing wave (expected as it is induced by the wave form directly in front of the barrier, as a wave generator in a flume) and as exponentially decaying (due to expected friction effects). The 2d field is obtained by multiplying the shown standing wave and propagating wave component for every point in the downstream basin.

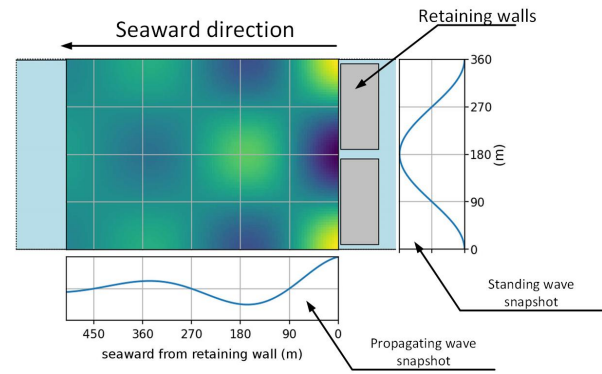
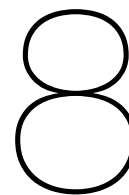


Figure 7.8: Top view illustration of what results may be expected from a more complete 2d model of the seaside area.

To model this effect, a more detailed model should consider the downstream canal with a number of discrete segments in streamwise direction. Furthermore, the full discharge and the associated convective terms in the momentum equations between these segments may be considered, since these may play a further role in the loss of energy of the mode 3 effect at the barrier.



Conclusions and recommendations

8.1. Conclusions

This report considers the retaining walls of the Maeslant barrier, the elements of the gates that retain the high water. Three effects have been investigated, which all have been observed when the retaining walls are floating in the waterway under a flow in seaward direction. It has been assessed whether an exceedance of design limits of the barrier due to these effects may be expected. The three effects, as treated in the introduction, are:

- A compressive force in the connection between the gate and the guiding tower, which pushes the retaining wall towards the parking docks, referred to as the **mystery force**.
- A quasi-constant change of the trim angle, which indicates a difference in vertical position between the two ends of the retaining wall, referred to as the **trim angle effect**.
- A periodic oscillation of the retaining wall trim angle, in existing literature referred to as the **mode 3 effect**.

From overview figures of the data per closure, it is verified that the different effects occur roughly during the same time period. From a non-linear analysis, based on rank correlation, a strong relation between the three effects is found (rank correlation of 0.72 and higher).

The considered effects appear to correlate with the strength of the flow. Strong statistical relations with the river level change (the decrease of water level observed on the riverside of the barrier after the start of de-ballasting, as defined in Table 3.2) have been found for all three effects (R^2 between 0.66 and 0.93). This input parameter closely correlates with the maximum seaward discharge at the barrier. For the mystery force and trim effect linear relations are found, for the mode 3 effect a non-linear relationship with a threshold and a maximum value is found. This relation can be modelled with, for example, a logistic curve. For the mystery force and trim effect, an empirical relationship with the local discharge squared is shown to be relevant (R^2 of 0.65 and 0.84 respectively). The relevant statistical models are summarized below:

- **Linear model with river level change:** mystery force, trim angle effect
- **Logistic model with river level change:** mode 3 effect
- **Model with peak local discharge squared:** mystery force, trim angle effect

The results of the conceptual models described in this report, of which the goal is to physically explain the observed effects, are mixed. The mystery force is described well using a momentum balance model that describes the hydraulic load on the gate. The trim effect is described as a function of a moment due to the mystery force, compensated by hydrostatic loads, this does not appear to give a full physical explanation, as the effect is significantly underestimated. Loading in trim due to a suction force may, however, play a relevant role in the trim angle effect being bigger than expected.

For the conceptual mode 3 model, the interaction of the retaining wall moving in trim and the water level downstream of the barrier is considered. This system results in a threshold head difference which leads to instability, but not in a maximum amplitude. This is a similar shortcoming as found in the design phase models, both models lack a description of effects that limit the amplitude of the mode 3 oscillation. Lastly, from the model, the mode 3 effect is only expected for much higher head differences than observed. The use of the model for the mode 3 effect appears limited.

Extrapolations of the mystery force and trim effect are considered for a local discharge at the barrier of 18,500 m³/s. The probability of such a discharge is unclear, but expected to be in the order of 10⁻⁶ per year.

Extrapolations for the mystery force yield 2,300-5,400 kN (based on the empirical local discharge model and momentum balance model). This is below the pull/push rod limit of 6,000 kN, the mystery force on its own does not appear to exceed design limits of the barrier. The extrapolation of the conceptual momentum balance model depends on the local water level, a higher water level increases the flow gap under the barrier, decreasing the local head difference, and through this the load on the barrier. For a level at 0 m NAP, the results are similar to the empirical local discharge model. For a level at +2 m NAP, the mystery force reduces by about 20%.

The extrapolation for the trim effect based on an empirical relation with the local discharge yields a trim effect of 7.5-13 millirad, which cannot be directly related to an exceedance of critical limits, if such limits are approached it may need to be compensated using ballast water.

The conceptual model for the mode 3 effect does not provide an expected magnitude of the effect. As it cannot verify the maximum magnitude found from statistical analysis, no definitive conclusions on the magnitude in extreme situations can be given. The statistical analysis, suggests a limit for the mode 3 effect, with a variance of 0.0325 millirad², including uncertainty interval. This is not much bigger than observed, and is therefore not expected to pose any problems to the structure. The considered dataset shows no strong indication for amplitudes that grow for more extreme situations. However, without physical reasoning, expectations for extreme situations remain largely unsubstantiated.

8.2. Recommendations

Based on the results and discussion of the considered models, suggestions for further research are put forward. Suggestions are given for further study of each of the different effects, starting with the mode 3 effect, for which further research appears to be the most relevant. Lastly, suggestions for additional observations during operation of the barrier are given.

Especially further study of the mode 3 effect appears relevant as both the occurrence and magnitude are at present not physically explained, because of which no definite conclusions of this effect in extreme situations can be given. The following suggestions are made:

- **Mode 3 model extension:** A description of the inertia of the flow under the retaining wall, and the propagation of the wave in the downstream basin. These mechanisms give a direction for effects that may physically explain the found onset of instability and the observed limit of the mode 3 magnitude.
- **Mode 3 interpretation:** The relation between the mode 3 effect and the other effects could also be theorized to be a form of resonance. This may be the case if the loading in pitch due to the mystery force builds up with a certain periodicity, due to effects, such as translating waves behind the barrier.

The trim angle effect is modelled with an empirical model but is not sufficiently physically explained, furthermore it may require operator input during operation:

- **Trim model extension:** Inclusion of other aspects that may load the retaining wall in trim, such as the suction force distribution along the retaining wall. Furthermore, the local head difference relative to the retaining wall position may influence the response to loading (see the final suggestions on additional observations).
- **Trim effect anticipation:** It may be further identified in which cases the trim effect may approach limits of what is deemed acceptable in terms of trim angle (such as for which combinations of storm surge and Rhine discharge), and what procedure must be followed in such a case, in order to compensate this effect with ballast water.

In terms of model improvement no concrete suggestions are made for the mystery force, however to analyse the contribution to the failure probability, the following minor recommendations are given:

- **Scenario analysis:** Inventory of (unaccounted for) scenarios, which may lead to a strong seaward flow, and thus to a high mystery force. Considered may be situations with seaward flow and a partially opened barrier. For long-term scenarios, the effect of climate change or changes in the water system on the expected extreme seaward discharge may be considered.
- **Hydraulic conditions:** An increased water level in extreme situations is expected to reduce the mystery force, due to an increases vertical flow gap. To more accurately derive the mystery force in extreme situations, the water level should be known in addition to the local discharge.
- **Total tangential loading:** In relation to the impact of the mystery force, all tangential loads should be considered. Additional loads may be due to the wind, the mode 3 effect, or short period waves. Based on this, the influence of the mystery force on the failure probability of the structure can be determined.

Lastly, two clear suggestions for observations at the barrier are formulated that can give further insight in the effects and validity of the conceptual models:

- **Effective retaining wall width:** It can be observed, whether under strong seaward flow, water reaches onto the retaining wall's rear protrusion (Figure 8.1). If this happens, the effective width of the retaining wall reduces (from b_1 to b_2), reducing its stiffness. Regarding the trim effect, this may partly explain the underestimation of the effect. If it does not occur for a local discharge as observed during test closures, it may still play a role in more extreme situations.
- **Local head difference:** In this report, the head difference is approximated from the calculated discharge and measured water level. Measurements of the water levels close to the barrier, during even a single closure, reduces the uncertainty surrounding the used schematization. This also relates to the point regarding the effective retaining width, since the effect, as illustrated in Figure 8.1, is dependent on the local head difference.

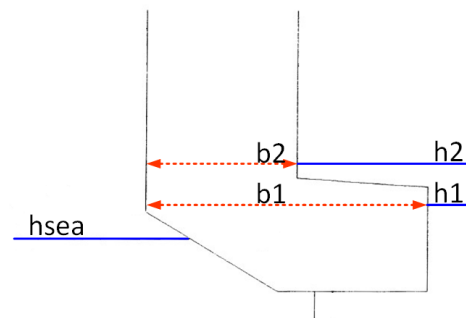


Figure 8.1: Illustration of change of width b due to a change of the upstream water level, copy of figure Figure 7.3

Bibliography

- Bakker, A. (2008). *Grote dip in de td-stang kracht [big pull/push rod force]* (memo).
- Bakker, A., Jongeling, T., Kolkman, P., & Wu, Y. S. (1991). Self-excited oscillations of a floating gate related to the gate discharge characteristics.
- BMK. (1992a). *Berekening dynamische/statische stabiliteit [calculation dynamic/static stability]* (BMK-document A-07-0014).
- BMK. (1992b). *Mathematisch model: Dynamisch/statisch stabiliteitsonderzoek [mathematical model: Dynamic/static stability research]* (BMK-document A-07-0010).
- BMK. (1992c). *Samenvatting stabiliteitsonderzoek variant 20 [summary stability research variant 20]* (BMK-document A-05-0008).
- BMK. (1994). *Topdocument kerende wand [top document retaining wall]* (BMK-document S-03-0022).
- Chakrabarti, S. (2001). Empirical calculation of roll damping for ships and barges. *Ocean Engineering*, 28(7), 915–932. [https://doi.org/10.1016/s0029-8018\(00\)00036-6](https://doi.org/10.1016/s0029-8018(00)00036-6)
- CROON elektrotechniek. (1998). *Metingen besw 96, aanvulling metingen besw 95 [measurements besw 96, additions measurements besw 95]* (BMK-document E-57-0093).
- Deltares. (2019). *SOBEK3-model waterstanden nabij de Maeslantkering [SOBEK3-model water levels near Maeslant barrier]* (Deltares project No. 1230119-000).
- Duvivier, E., & Nederend, H. (2013). *Analyse meetdata functioneringsssluiting 2013 [analysis data 2013 test closure]* (Report).
- Duvivier, E., & Nederend, H. (2016). *Analyse functioneringsssluiting 2015 [analysis 2015 test closure]* (Report).
- Elger, D. F., Williams, B. C., Crowe, C. T., & Roberson, J. A. (2013). *Engineering fluid mechanics, 10th edition si version*. John Wiley and Sons.
- Gauthier, T. (2001). Detecting trends using spearman's rank correlation coefficient. *Environmental Forensics*, 2(4), 359–362. <https://doi.org/10.1006/enfo.2001.0061>
- Google Earth. (2022). Maeslant barrier area satellite image. <https://earth.google.com/web/@51.96936687,4.14468189,4.16689796a,7200.56884691d,35y,19.82540689h,0t,0r>
- Hessels, J. (2011). *Inschatting debiet op basis van stromingsmetingen [discharge estimation bases on flow measurements]* (Document 048R019M050-REV.-1).
- Jongeling, T., & A.D., B. (1995). Oscillation of a sector-gate barrier caused by fluid resonance. *Proceedings of Sixth International Conference on Flow-Induced Vibration*, 10–12.
- Journée, J., & Massie, W. (2001). *Offshore hydromechanics first edition*.
- KNMI. (2022). Wind - windspeed, direction, standarddeviation at a 10 minute interval. <https://dataplatfom.knmi.nl/dataset/windgegevens-1-0>
- Kolkman, P., & Jongeling, T. (2007). *Dynamic behaviour of hydraulic structures: Part a: Structures in flowing fluid*. Delft Hydraulics. <https://repository.tudelft.nl/islandora/object/uuid%3A057be929-11e8-4da0-93cd-7df8c59d1d4d>
- Koninklijke PBNA. (n.d.-a). *Opleidingen svkw: Basismodule 2 werking kering inleiding (2) [base module 2: Barrier workings introduction (2)] (6001-010)*.
- Koninklijke PBNA. (n.d.-b). *Opleidingen svkw: Handboek 3: Bewegingswerken sectordeur [book 3: Movement mechanics sector gate] (6028-010)*.
- Koninklijke PBNA. (n.d.-c). *Opleidingen svkw: Vervolgmodule 9 bediening 8: Bewegingswerken [continued module 9 control 8: Movement mechanics] (6014-010)*.
- Lamers, W. (2010). *Drukkracht td-stang tijdens hoogdrijvende fase [pull/push-rod compressive force during high-floating phase]* (Report).
- Newman, J. N. (2018). *Marine hydrodynamics*. The MIT Press.
- OpenStreetMap. (2022). Map of maeslant barrier. <https://www.openstreetmap.org/#map=15/51.9538/4.1665>
- Pandas. (2022a). *Pandas.dataframe.resample*. <https://pandas.pydata.org/docs/reference/api/pandas.DataFrame.resample.html>

- Pandas. (2022b). Pandas.dataframe.rolling. <https://pandas.pydata.org/docs/reference/api/pandas.DataFrame.rolling.html>
- Rijkswaterstaat. (n.d.-a). *Basisdocumentatie maeslantkering: Basismodule 1 [Maeslant barrier base documentation: Module 1]* (version 4.0, M00-ALG-01-NL).
- Rijkswaterstaat. (n.d.-b). *Basisdocumentatie maeslantkering: Handboek 2: Kerende wand en vakwerkarmen [Maeslant barrier base documentation book 2: Retaining wall and truss arms]* (version 3.0, M00-ALG-04-NL).
- Rijkswaterstaat. (n.d.-c). Maeslantkering gate. <https://proxy.archieven.nl/0/0237AFD17643427EA195D039E4A65EFD>
- Rijkswaterstaat. (n.d.-d). Maeslantkering overview picture. <https://proxy.archieven.nl/0/CE8481B8A1014B42B3BA6C4268C96463>
- Rijkswaterstaat. (2007). Closed maeslant barrier. <https://proxy.archieven.nl/0/F9D13D5842194D239B28D3EDFA2DB96A>
- Rijkswaterstaat. (2009). *Verkenning ebdebiet onder mk tijdens overliggen [inventarisation seaward discharge under barrier]* (memo).
- Rijkswaterstaat. (2021). Bathymetrie nederland [bathymetry map of the netherlands]. https://maps.rijkswaterstaat.nl/geoweb55/index.html?viewer=Bathymetrie_Nederland
- Rijkswaterstaat. (2022a). Waterinfo. <https://waterinfo.rws.nl/>
- Rijkswaterstaat. (2022b). *Wettelijke beoordeling europaotkering i [legal review europaot barrier i]* (Report).
- Rzadkowski, G., & Sobczak, L. (2020). A generalized logistic function and its applications. *Foundations of Management*, 12(1), 85–92. <https://doi.org/doi:10.2478/fman-2020-0007>
- Sahinler, S., & Topuz, D. (2007). Bootstrap and jackknife resampling algorithms for estimation of regression parameters. *Journal of Applied Quantitative Methods*, 2(2), 188–199.
- Scikit-learn. (2022). Sklearn.linearmodel.linearregression. <https://scikit-learn.org/stable/modules/generated/sklearn.linearmodel.LinearRegression.html>
- Scipy Community. (2022a). Scipy.interpolate.interp1d. <https://docs.scipy.org/doc/scipy/reference/generated/scipy.interpolate.interp1d.html>
- Scipy Community. (2022b). Scipy.optimize.curve_fit. https://docs.scipy.org/doc/scipy/reference/generated/scipy.optimize.curve_fit.html
- Scipy Community. (2022c). Scipy.stats.linregress. <https://docs.scipy.org/doc/scipy/reference/generated/scipy.stats.linregress.html>
- Smith, H., & Draper, N. R. (1998). *Applied regression analysis*. Wiley.
- Torrence, C., & Compo, G. (1998). A practical guide to wavelet analysis. *Bulletin of the American Meteorological Society*, 79. https://atoc.colorado.edu/research/wavelets/bams_79_01_0061.pdf
- Torrence, C., & Compo, G. (2018). A practical guide to wavelet analysis. <https://atoc.colorado.edu/research/wavelets/software.html>
- Verheij, H., C., S., & R., G. (2008). *Inland waterways: Ports, waterways and inland navigation*. VSSD.
- Voorendt, M., & Molenaar, W. (2020). *Manual hydraulic structures*.
- WL|Delft Hydraulics. (1990a). *Maeslant kering: Onderzoek met behulp van een sectiemodel - optimalisatie vormgeving sectordeur [maeslant barrier: Research using a section model: Optimisation of the retaining wall shape]* (WL-Report Q1190). <https://repository.tudelft.nl/islandora/object/uuid%3Ad27017e8-f42e-4ec2-a39e-a86bbd29bada>
- WL|Delft Hydraulics. (1990b). *Maeslant kering: Vervolgonderzoek naar het responsiegedrag van de sectordeuren in een overzichtsmodeel [maeslant barrier: Research of response of the retaining walls in a physical model]* (WL-Report Q1140). <https://repository.tudelft.nl/islandora/object/uuid%3Ada211de6-03e0-430e-ba5a-7cfc1702f3e8>
- WL|Delft Hydraulics. (1991). *Maeslant kering: Analyse van het responsiegedrag van de sectordeuren met behulp van een rekenmodel [maeslant barrier: Analysis of response behaviour of the retaining walls with a mathematical model]* (WL-Report Q1271). <https://repository.tudelft.nl/islandora/object/uuid%3A0f35b499-5afa-470d-a8fb-df06f25a0452>

List of Figures

1	a) overzicht Maeslantkering met een van de kerende wanden (retaining wall) en de locatie van de mystery force gemarkeerd b) illustratie trimhoek (trim angle) vrijheidsgraad, afbeeldingen van Rijkswaterstaat, n.d.-a	ii
2	Illustratie van de verandering van breedte b door een verandering van de bovenstroomse waterstand, kopie van Figure 7.3	iii
3	a) overview of the Maeslant barrier with one of the retaining walls and location of the mystery force highlighted b) illustration of the trim angle degree of freedom, image from Rijkswaterstaat, n.d.-a	iv
4	Illustration of change of width b due to a change of the upstream water level, copy of Figure 7.3	v
1.1	Maeslant barrier introduction	1
1.2	a) overview of the Maeslant barrier with one of the retaining walls and location of the mystery force highlighted b) illustration of the trim angle degree of freedom	2
2.1	Maeslant barrier overview, image from Rijkswaterstaat, n.d.-a	4
2.2	Retaining wall degrees of freedom, positive directions are as indicated in the figure, image from Rijkswaterstaat, n.d.-b	5
2.3	Maeslant barrier radial and tangential load transfer	6
2.4	Cross-sectional view of waterway and movement of the gates with the corresponding standing wave where applicable (in blue)	7
2.5	Considered stability lines, image from Jongeling and A.D., 1995	7
2.6	Overview of the 2D scale model (1:40 scale), longitudinal and top view, image from WL Delft Hydraulics, 1990a	8
2.7	Discharge variation model definitions	8
2.8	schematization of the mass spring model from, image from BMK, 1992b	9
2.9	Final retaining wall cross-section sketch, image from BMK, 1992c	10
3.1	Time between end of de-ballasting and returning to docks per closure, time given in HH:MM format. 'FS' indicates the different test closures, 'VS' indicates the closure under storm conditions	14
3.2	Locations of sink and trim angle inclinometers, image from Rijkswaterstaat, n.d.-b	15
3.3	Approximate location of water level measurement stations, inferred from satellite pictures. Background image from Google Earth, 2022	15
3.4	Location KNMI weather station relative to barrier. Background image from Google Earth, 2022	16
3.5	Equidistant signal construction method	17
3.6	Transformation to equidistant signal method comparison	17
3.7	Equidistant signal interpolation interval of the signal in Figure 3.6	18
3.8	wavelet power spectrum at moment of mode 3 peak (only closures with an identified mode 3 effect)	21
3.9	Wavelet analysis of the 2019 trim signals	21
3.10	Overview of barrier behaviour and flow conditions during the 2008 test closure	23
3.11	Sea and river side water level for the 2009 and 2013 test closure, time span from moment of full closure until 4 hours after fully de-ballasted	25
3.12	Boxplots of the identified seaward flow effects (off all considered closures), with the boxes indicating the range of the upper and lower quartile	25

3.13	Boxplots of the quantities from Table 3.2 (off all considered closures), with the boxes indicating the range of the upper and lower quartile	26
4.1	Correlation between mode 3 results for the north and south retaining wall	29
4.2	Correlation between trim mode 3 compared to dock water level mode 3	29
4.3	Linear correlation between the considered effects (mode 3 variance as observed in the trim signals)	30
4.4	Linear correlation of negative head difference and the seaward flow effects	31
4.5	Linear correlation of Lobith discharge and the seaward flow effects	31
4.6	Linear correlation of Hoek van Holland mean wind speed and the seaward flow effects	32
4.7	Top part of the constructed correlation matrix	33
4.8	Linear correlation of river side water level change and the seaward flow effects	33
4.9	Exponential and parabolic fit for the mode 3 effect to the river level change	34
4.10	Linear correlation of mode 3 exponential fit residuals and the start water level	35
4.11	Multiple regression fit to mode 3 maximum variance	35
4.12	Mystery force multiple regression results	36
4.13	Mystery force empirical models	37
4.14	Trim angle effect empirical models	38
4.15	Mode 3 effect empirical models	38
5.1	Proposed load components that may contribute to the mystery force, image from Koninklijke PBNA, n.d.-c	40
5.2	Vertical position of loads that may contribute to the mystery force in front view of retaining wall, base image from Koninklijke PBNA, n.d.-a	41
5.3	Indicative hydrostatic pressure distribution due to trim and resulting moment, base image from Koninklijke PBNA, n.d.-a	41
5.4	Cross-sectional variation of the flow gap along the retaining wall under an exaggerated trim angle, base image from Koninklijke PBNA, n.d.-a	42
5.5	Tangential load from hydrostatic schematization	43
5.6	Barrier momentum balance schematization, with hydrostatic loads in red, momentum associated with flow in blue and the force from the gate in green	43
5.7	Tangential force induced by water level variation	43
5.8	Suction force on retaining wall	44
5.9	Ship degrees of freedom, image from Journée and Massie, 2001	45
5.10	1D retaining wall model with rotational degree of freedom	46
5.11	a) Mode 3 model top view, b) model front view. Two variables (h_1, h_2) that represent the water level deviation in 2 marked discrete segments, θ indicates the retaining wall pitch. The solid arrows indicate flow in and out of the marked segments, the dotted arrow the overall flow direction.	47
5.12	Discharge elements contributing to the continuity in h_1 and h_2 . $h_s = 0$ and $h_r = 0$ indicate that up- and downstream no deviations from the stationary situation occur	48
5.13	Mode 3 model top view (a) and side view (b) with defined geometry	49
5.14	Retaining wall front view for d_i schematisation	49
5.15	Control volume for flow component Q_{1-s}	51
5.16	Moment exerted on retaining wall by h_1 and h_2	54
6.1	Head difference at maximum mystery force	57
6.2	Results from physical base models plotted as function of observed mystery force	57
6.3	Results from momentum model plus C effects plotted as function of observed mystery force	58
6.4	Result for constant trim effect	58
6.5	Constant trim effect model results with a fitted stiffness	59
6.6	Mode 3 variance as function of local head difference	60
6.7	T and r as function of parameter Δs	62
6.8	T and r as function of parameter Δs , with reduced retaining wall period	63
6.9	Period, $T(2\pi/\omega)$, as function of parameters Δs and c_s (with $\Delta h_0 = 0.3\text{m}$)	64
6.10	α , as function of parameters Δs and c_s (with $\Delta h_0 = 0.3\text{m}$)	64

6.11	Stability and period of the system under varying initial head difference	65
6.12	Stability and period of the system under varying initial head difference and c_r with $\Delta s = 120\text{m}$ and $c_s = 0.4$	66
6.13	Parameters of estimated model as function of Δh_0	67
6.14	Sea and river side water level after the high water peak (2018 storm closure)	71
6.15	Head difference as calculated for the considered discharge range	72
6.16	Mystery force models extrapolated for extreme discharges	72
6.17	Trim angle model extrapolated based on the empirical discharge squared model	73
6.18	Logistic fits to the mode 3 data using jackknife resampling	74
6.19	Parabolic fits to the mode 3 data using jackknife resample	75
6.20	Boxplot of the observed mystery force and different model predictions for $18,500 \text{ m}^3/\text{s}$ (from Figure 6.16)	76
6.21	Boxplot of the observed trim effect and model predictions for $18,500 \text{ m}^3/\text{s}$ (from Figure 6.17)	76
7.1	Excerpt of the 2008 mystery force data, with three distinct moving averages	77
7.2	River level change and peak discharge as function of the calculated local head difference	79
7.3	illustration of change of width b due to a change of the upstream water level	80
7.4	illustration of pressure head differential induced by differential flow velocity	80
7.5	Excerpt of the 2008 data, to illustrate the phase correspondence of the trim angle and water level signal	81
7.6	Eigenperiod of the retaining wall in pitch as function of the vertical flow gap, found in 3d model test with the numbers representing (period/damping ratio) (WL Delft Hydraulics, 1990b)	82
7.7	Control volume under retaining wall with hydrostatic pressure illustrated in red, with definitions as in Figure H.7	82
7.8	Top view illustration of what results may be expected from a more complete 2d model of the seaside area.	83
8.1	Illustration of change of width b due to a change of the upstream water level, copy of figure Figure 7.3	86
B.1	Morlet wavelet example, image from Torrence and Compo, 1998	97
C.1	Magnitude of the identified trim peak, for the North (blue) and south (orange) wall. The vertical bar indicates the size of the peak (vertical axis in radians).	101
D.1	Overview of mode 3 behaviour and flow conditions during the 2007 test closure	102
D.2	Overview of mode 3 behaviour and flow conditions during the 2008 test closure	103
D.3	Overview of mode 3 behaviour and flow conditions during the 2009 test closure	104
D.4	Overview of mode 3 behaviour and flow conditions during the 2010 test closure	105
D.5	Overview of mode 3 behaviour and flow conditions during the 2011 test closure	106
D.6	Overview of mode 3 behaviour and flow conditions during the 2012 test closure	107
D.7	Overview of mode 3 behaviour and flow conditions during the 2013 test closure	108
D.8	Overview of mode 3 behaviour and flow conditions during the 2014 test closure	109
D.9	Overview of mode 3 behaviour and flow conditions during the 2015 test closure	110
D.10	Overview of mode 3 behaviour and flow conditions during the 2017 test closure	111
D.11	Overview of mode 3 behaviour and flow conditions during the 2018 test closure	112
D.12	Overview of mode 3 behaviour and flow conditions during the 2019 test closure	113
D.13	Overview of mode 3 behaviour and flow conditions during the 2020 test closure	114
D.14	Overview of mode 3 behaviour and flow conditions during the 2021 test closure	115
E.1	Full correlation matrix	116
G.1	Retaining wall modelled as pendulum Koninklijke PBNA, n.d.-a	119
H.1	Estimated head difference from local discharge	121

H.2	schematization for determining hydrostatic load on short side, original cross-section in black from (WL Delft Hydraulics, 1990b)	122
H.3	Mystery force predicted based on head difference	123
H.4	Maeslant barrier bathymetry data from (Rijkswaterstaat, 2021), background map from (OpenStreetMap, 2022)	124
H.5	Barrier momentum balance schematization, with hydrostatic loads in red, momentum associated with flow in blue and the force from the gate in green	124
H.6	Barrier momentum balance schematization top view, with location of boundaries in red, and the force on the barrier in green. Base image from Koninklijke PBNA, n.d.-a	124
H.7	Illustration of angle of short side relative to horizontal, not to scale. Base image from Koninklijke PBNA, n.d.-a	125
H.8	Mystery force predicted based on head difference	126
H.9	Tangential force induced by water level variation	127
I.1	Vertical positions used to determine \overline{GM}	130
I.2	Moment contribution due to load F	131
J.1	1D plate added mass components, image from Newman, 2018	132
L.1	a) Jackknife estimates compared to simple regression model b) comparison of slope parameter distribution from simple regression and jackknife resample	136
L.2	a) Jackknife estimates compared to simple regression model b) comparison of slope parameter distribution from simple regression and jackknife resample	137

List of Tables

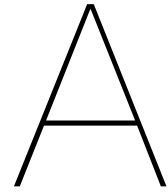
3.1	Final dataset items directly derived from raw data	19
3.2	quantities related to high floating phase conditions	24
4.1	Empirical discharge models	37
5.1	Force model for short side loading	44
5.2	Force related additional effects	45
5.3	Parameters employed in formulae from Table 5.1-5.2	45
6.1	parameter fit for B2 (momentum model)	58
6.2	R ² parameter of the different conceptual models	68
6.3	R ² -score of the different statistical models	69
6.4	models considered to for effects extrapolation	70
6.5	Considered scenarios for momentum balance modes	72
6.6	Logistic model parameters	75
C.1	Effects magnitude per closure	99
C.2	Data source for mystery force	100
F.1	Fitted parameters empirical mystery force models without intercept	117
F.2	Fitted parameters empirical mystery force models with intercept	117
F.3	Fitted parameters empirical trim effect models without intercept	117
F.4	Fitted parameters empirical trim effect models with intercept	118
F.5	Fitted parameters empirical mode 3 effect models without intercept	118
F.6	Fitted parameters empirical mode 3 effect models with intercept	118
H.1	short side hydrostatic area calculation	122
H.2	short side hydrostatic load calculation	123

List of Symbols

This list concerns the symbols used to describe quantities and variables considered in the main report. The spring model described in Equation 2.4 is only given to give an overview of the existing models, and clashes with other definitions, its variables are therefore not listed. Neither listed are model parameters in the statistical relations. Symbols only used in appendices are defined in their respective locations and not listed.

$[1, r]$	mode 3 effect eigenvector	
α	exponential growth factor	[-]
α_{stab}	design phase model stability factor	[-]
Δh	local head difference over the barrier	[m]
Δh_g	global head difference observed over the measurement locations	[m]
Δs	mode 3 model segment length	[m]
Δx	mode 3 model segment width	90 [m]
μ	discharge coefficient	[-]
ω	angular frequency	[rad/s]
ϕ	phase shift	[rad]
ρ	water density (brackish water)	1,012 [kg/m ³]
θ	retaining wall trim/pitch angle	[rad]
θ_{turn}	retaining wall turn angle	[rad]
ζ	Retaining wall damping ratio	-]
A_{bottom}	Retaining wall bottom surface area	2,763 [m ²]
A_{short}	Retaining wall short side surface area	60 [m ²]
B	waterway width	360 [m]
b	retaining wall width	15 [m]
c	shallow water wave speed	[m/s]
c_r	damping matrix coefficient	-]
c_s	seaward flow coefficient	-]
d, d_0	vertical flow gap under retaining wall	[m]
d_s, d_r	sea, river side water depth	[m]
e	mystery force eccentricity	[m]
F_{MF}	mystery force	[N]
G	sector gate weight	126,000 [kN]
g	gravitational constant	9.81 [m/s ²]
h_s	sea side water level deviation	[m]
J	retaining wall inertia	[kg m ²]

J_{hd}	added retaining wall inertia	[kg m ²]
k_{emp}	empirically estimated pitch stiffness	[Nm/rad]
k_{hd}	hydrostatic pitch stiffness	[Nm/rad]
Q	discharge	[m ³ /s]
q	discharge per unit width	[m ² /s]
T	oscillation period	[s]
u	flow velocity	[m/s]
W^2	mode 3 variance in retaining wall pitch, dock water level	[rad ² , m ²]
x_1, x_2	mode 3 model segments x-axis position	-45, 45 [m]



Trim angle data description

At each of the locations in figure 6 three inclinometers are present, this to increase the precision of the measurement (CROON elektrotechniek, 1998). The inclinometers have a standard deviation of 0.625 milliradians (CROON elektrotechniek, 1998), for a set of three sensors the standard deviation can be assumed to be:

$$\sigma = \frac{1}{\sqrt{N}}\sigma_{sensor} = \frac{1}{\sqrt{3}}(0.625\text{mRad}) = 0.361\text{mRad} \quad (\text{A.1})$$

The true precision of the available data depends on the number of samples that are used to make up the data, a quantity which is unclear. Therefore, further analysis of the data is performed. The data is given with a high number of decimal places, however examination of the trim data shows consecutive data points (in 99% percent of the cases) move in steps of 0.05 milliradians or more, suggesting that the resolution of the data is at least limited by this step. Therefore, it is assumed the trim angle data has a resolution somewhere in the range 0.01-0.1 milliradians.

B

Power spectrum analysis

In this thesis, the oscillatory movements of the retaining walls and signals relating to this effect are considered. The magnitude of these effects is not constant, and the frequencies with which the retaining walls vibrate may vary. An analysis based on the wavelet transform gives a method that can deal with these non-stationary aspects

This wavelet analysis is done based on MATLAB code provided by Torrence and Compo, 2018. A description of this analysis method is given in this section based on Torrence and Compo, 1998, a thorough look into the mathematical background is however not within the scope of this appendix.

B.1. The Wavelet transform

In the basis, the wavelet transform can be thought of as the fitting of a small periodic function, the wavelet, to the signal that is analysed. In this thesis the Morlet wavelet is used as base, it is a part of a sinusoid modulated by a Gaussian function (Torrence & Compo, 1998). Both the real and imaginary part of a Morlet wavelet are shown in Figure B.1.

The wavelet transform is performed at each entry of the original signal and for wavelets with a wide range of scales, this scale relates to the period of the sinusoid. A set of appropriate scales is created by the software using (Torrence & Compo, 1998):

$$s_j = s_0 2^{j\delta j}, j = 0, 1, \dots, N \quad (\text{B.1})$$

Where δj is a scale factor, that should be smaller than 0.5 for the Morlet wavelet (Torrence & Compo, 1998). In this thesis $\delta j = 0.125$ is used. The wavelet transform is the convolution of the signal with a scaled and translated wavelet (Torrence & Compo, 1998).

B.2. 2D wavelet power spectrum

From the fitting of the wavelets to the signal, a two-dimensional power spectrum can be created, by taking the square of the modulus of the complex wavelet transform result. In this spectrum, the power can be read as a function of the time and the period of the considered wavelet. The period is determined from the scale, s , of the Morlet wavelet using the following function (Torrence & Compo, 1998), where the non-dimensional frequency, ω_0 , is a chosen factor, equal to 6 in this thesis:

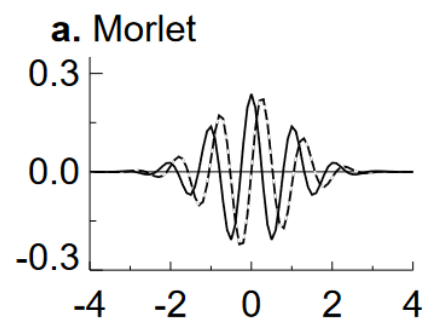


Figure B.1: Morlet wavelet example, image from Torrence and Compo, 1998

$$p = \frac{4\pi s}{\omega_0 + \sqrt{2 + \omega_0^2}} = \frac{4\pi s}{6 + \sqrt{2 + 6^2}} = 1.033s \quad (\text{B.2})$$

At the boundaries of the signal the wavelet transform does not yield reliable results, therefore a cone of influence can be indicated to show where this effect occurs. This cone of influence is a function of the wavelet scale, for the Morlet wavelet with scale s the cone of influence extends t seconds from the ends of the signal (Torrence & Compo, 1998), proportional with the wavelet scale:

$$t = \sqrt{2} s \quad (\text{B.3})$$

For the mode 3 behaviour, with a period of about 35 seconds, this means the cone of influence extends for:

$$t = \sqrt{2} \cdot 30 = 50 \text{ s} \quad (\text{B.4})$$

This is very small compared to the considered time periods, the high floating phase takes several hours and the mode 3 behaviour needs 15-50 minutes to build up (see section 2.5). This analysis method is therefore valid for the mode 3 effect.

B.3. Scale-averaged wavelet power

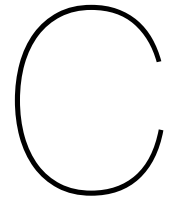
To obtain a measure for the magnitude of the mode 3 effect from the 2D spectrum, the wavelet power within the period band identified to be relevant for the effect is considered.

For each point in time, t , the wavelet power between the relevant scales s_{j_1} and s_{j_2} is determined with (Torrence & Compo, 1998):

$$\bar{W}^2 = \frac{\delta j \delta t}{C_\delta} \sum_{j_i=j_1}^{j_2} \frac{|W(s_j)|^2}{s_j} \quad (\text{B.5})$$

With:

- $\delta j = 0.125$: chosen scale factor
- $C_\delta = 0.776$: empirically derived reconstruction factor (Torrence & Compo, 1998)
- δt : signal time step
- s_j : wavelet scale
- $W(s_j)$: wavelet power spectrum at time t and scale s_j



Effects quantified characteristics

	Mode 3 peak variance (10^{-8} rad ²)	Mode 3 trim duration (HH:MM)	Mode 3 dock level peak variance (10^{-3} m ²)	Mode 3 dock level duration (HH:MM)	Mystery force (kN)	Trim angle effect (mrad)
FS2007	3.2	1:32	6.5	1:42	-	1.4
FS2008	3.2	2:08	6.9	2:14	377	1.4
FS2009	1.4	1:10	3.9	1:19	517	1.4
FS2010	0.0	0:00	0.0	0:00	380	0.9
FS2011	0.0	0:00	0.0	0:00	106	0.6
FS2012	0.0	0:00	0.0	0:00	250	0.9
FS2013	2.4	2:09	5.9	2:19	750	1.6
FS2014	0.0	0:00	0.0	0:00	200	0.6
FS2015	1.2	1:05	3.6	1:22	400	1.1
FS2017	1.7	1:42	4.7	1:53	510	1.3
FS2018	0.5	1:06	2.0	1:18	345	0.9
FS2019	2.4	1:52	6.3	2:09	463	1.6
FS2020	0.0	0:00	0.0	0:00	191	0.2
FS2021	1.4	1:11	4.4	1:21	425	1.1

Table C.1: Effects magnitude per closure

	mf data source
FS2007	no data
FS2008	strain gauge
FS2009	strain gauge
FS2010	strain gauge
FS2011	pressure data
FS2012	from report
FS2013	from report
FS2014	from report
FS2015	from report
FS2017	from report
FS2018	from report
FS2019	from report
FS2020	from report
FS2021	from report

Table C.2: Data source for mystery force

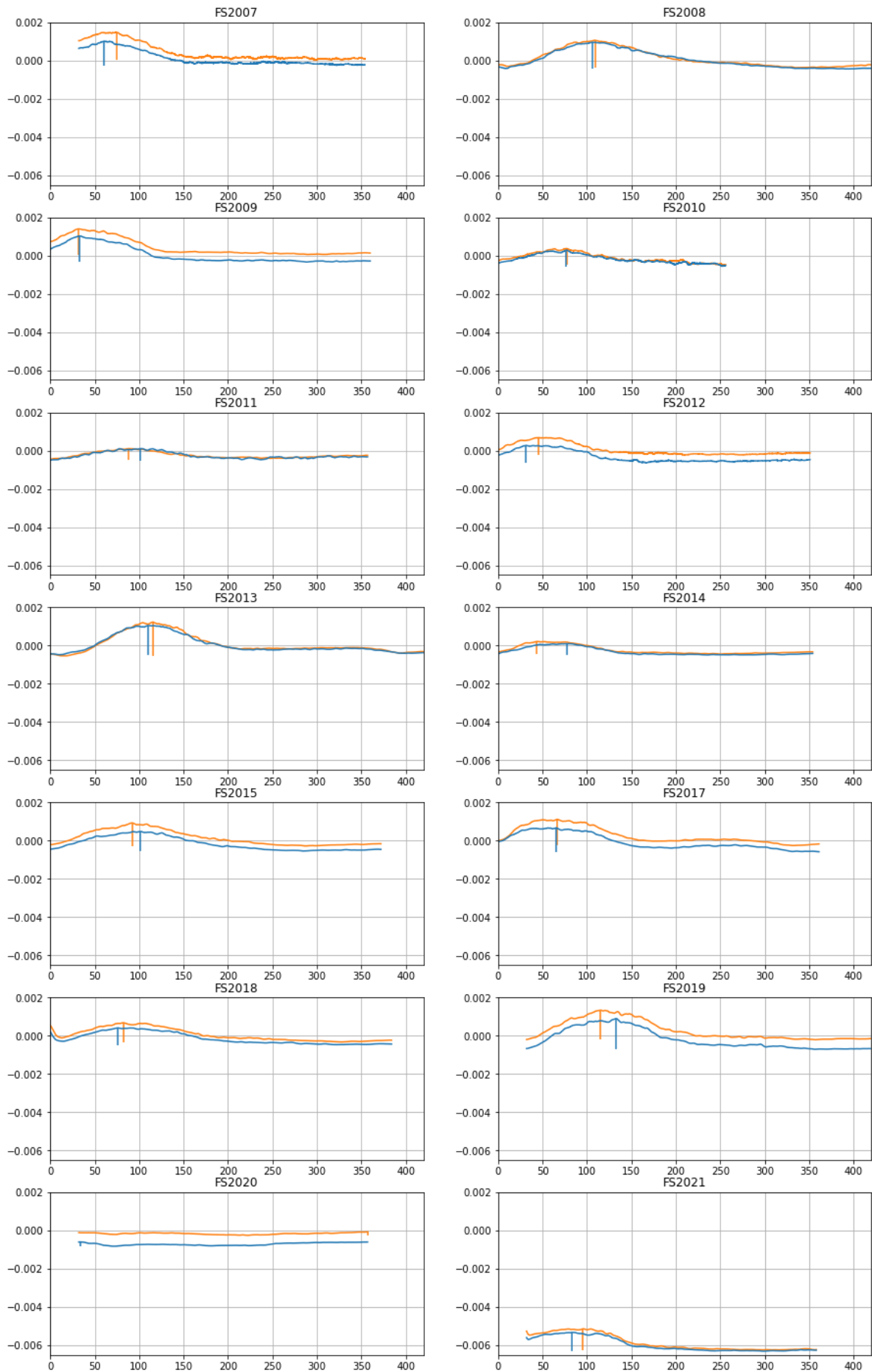
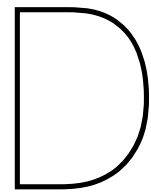


Figure C.1: Magnitude of the identified trim peak, for the North (blue) and south (orange) wall. The vertical bar indicates the size of the peak (vertical axis in radians).



Dynamic effect and hydraulic conditions overviews

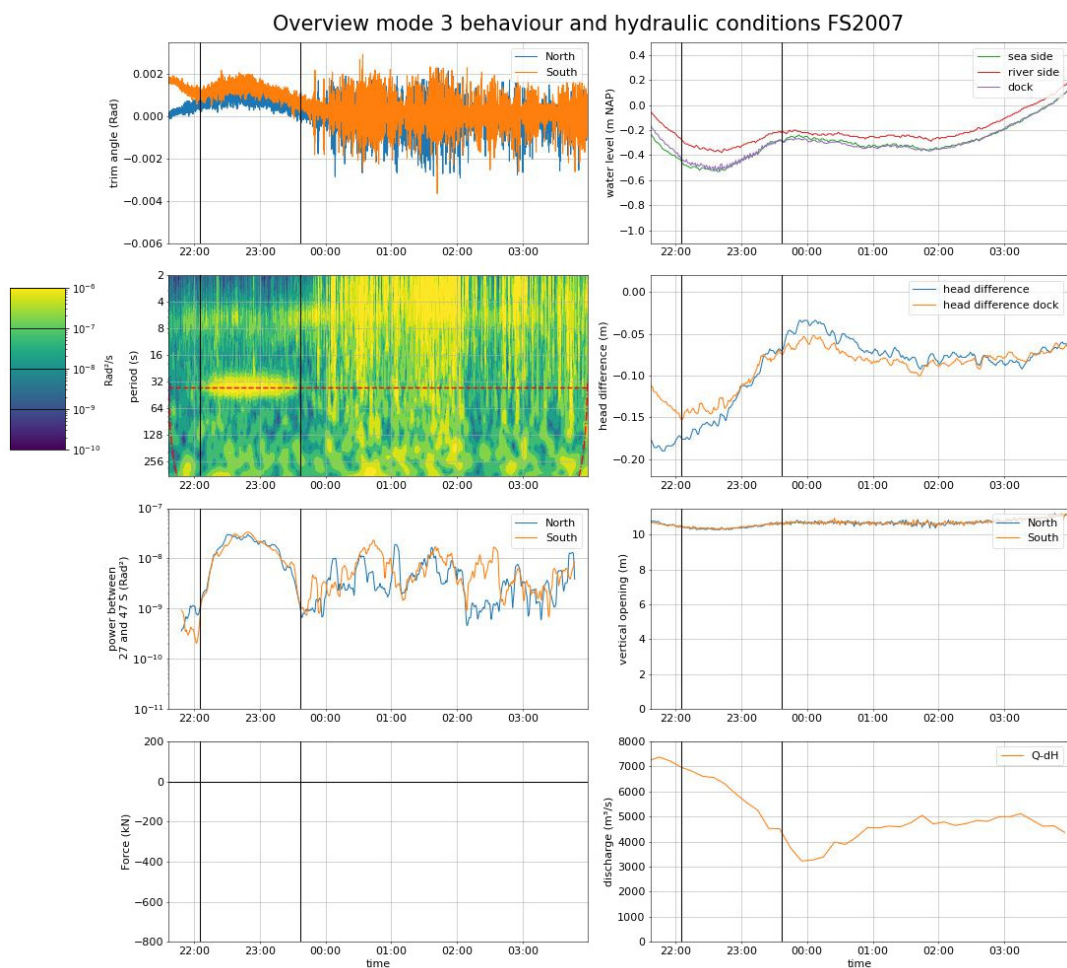


Figure D.1: Overview of mode 3 behaviour and flow conditions during the 2007 test closure

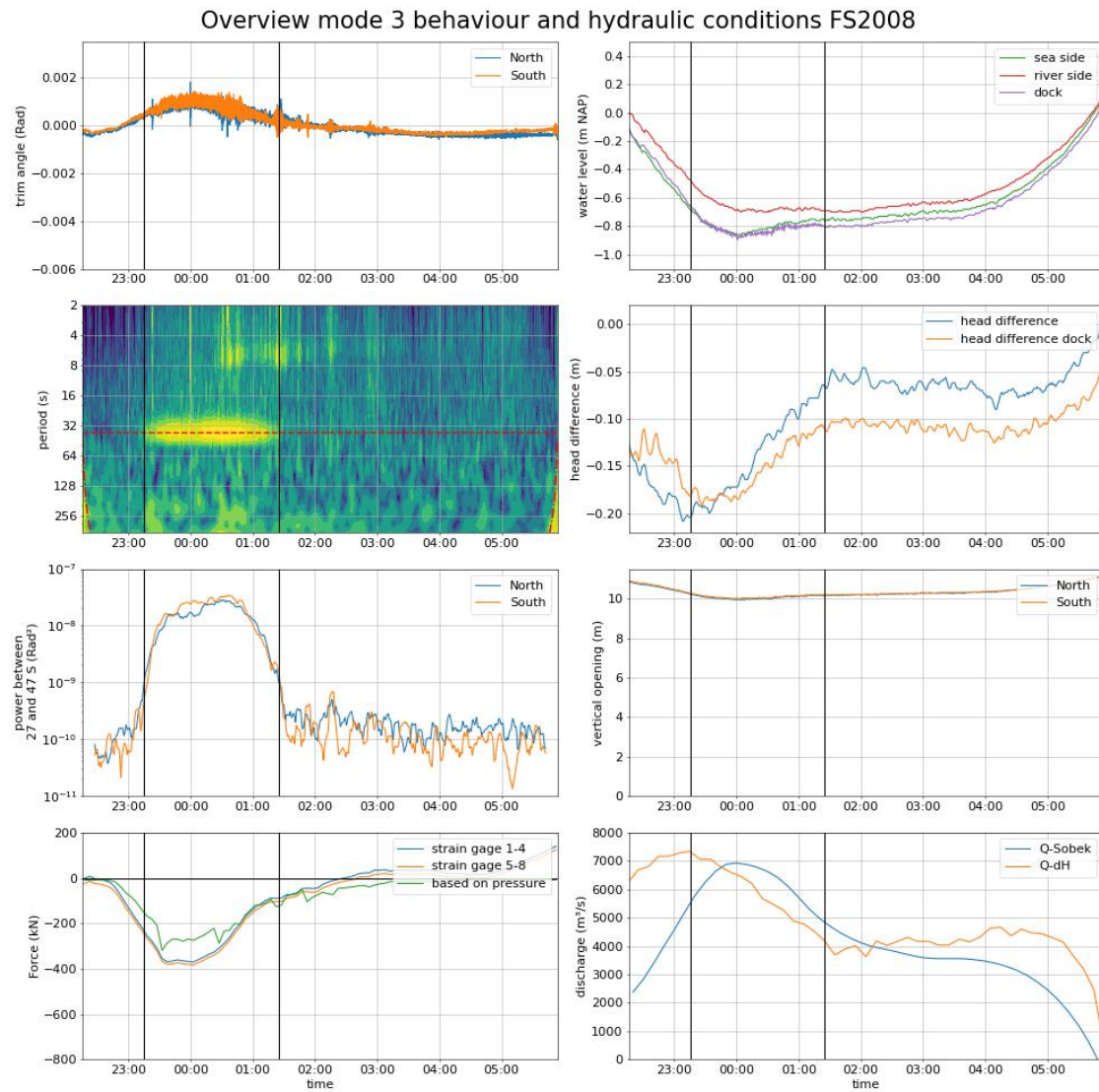


Figure D.2: Overview of mode 3 behaviour and flow conditions during the 2008 test closure

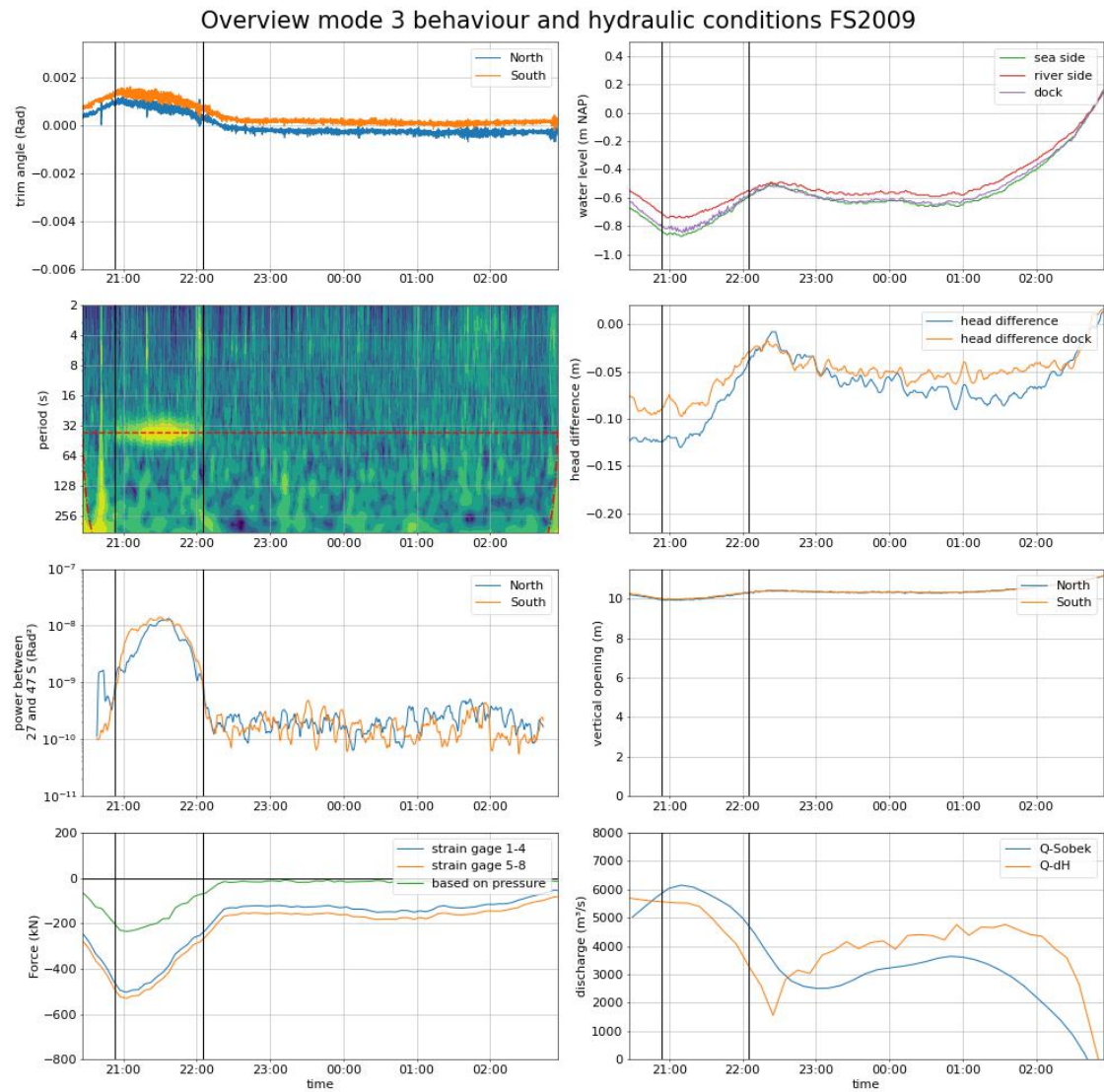


Figure D.3: Overview of mode 3 behaviour and flow conditions during the 2009 test closure

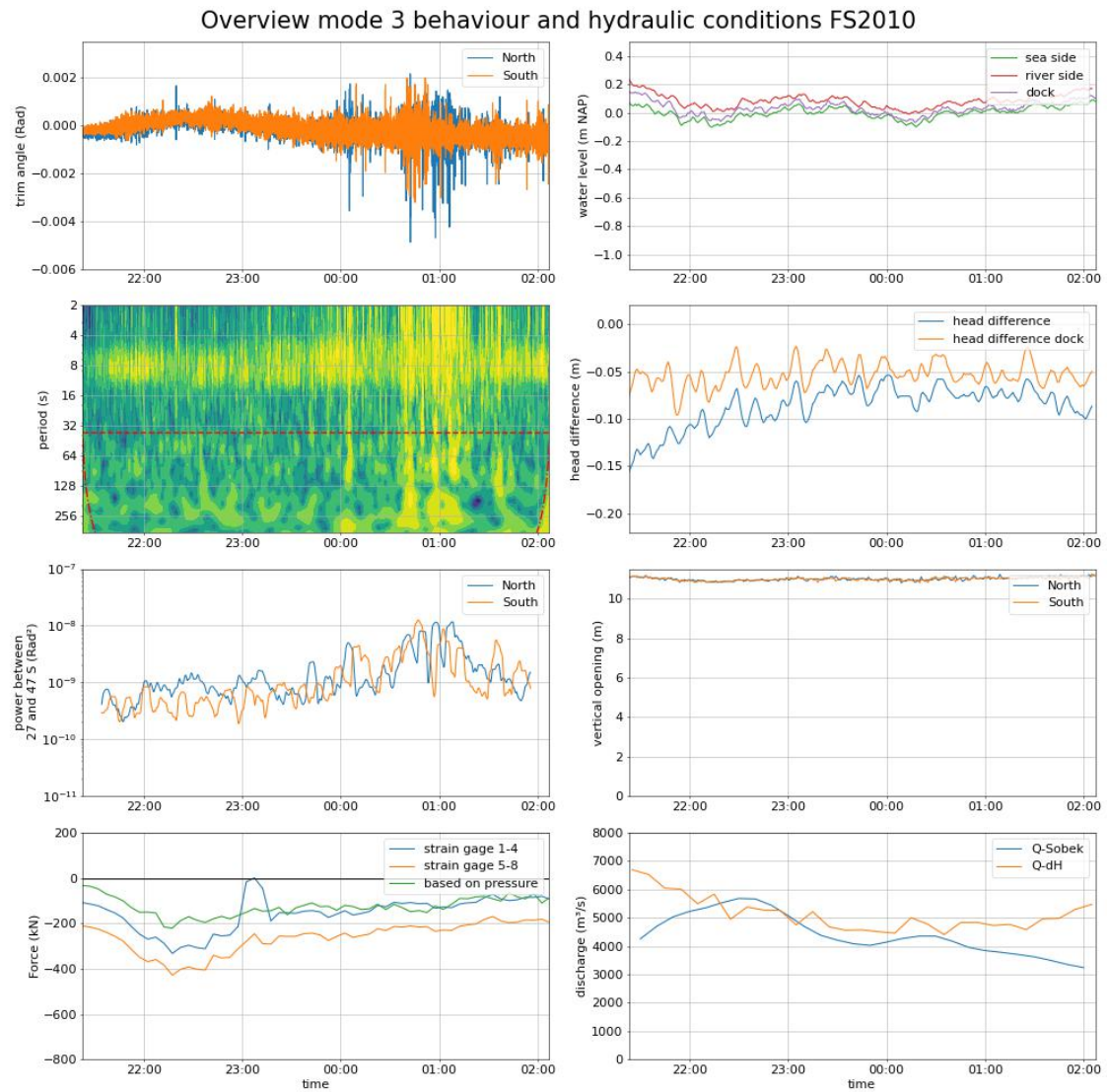


Figure D.4: Overview of mode 3 behaviour and flow conditions during the 2010 test closure

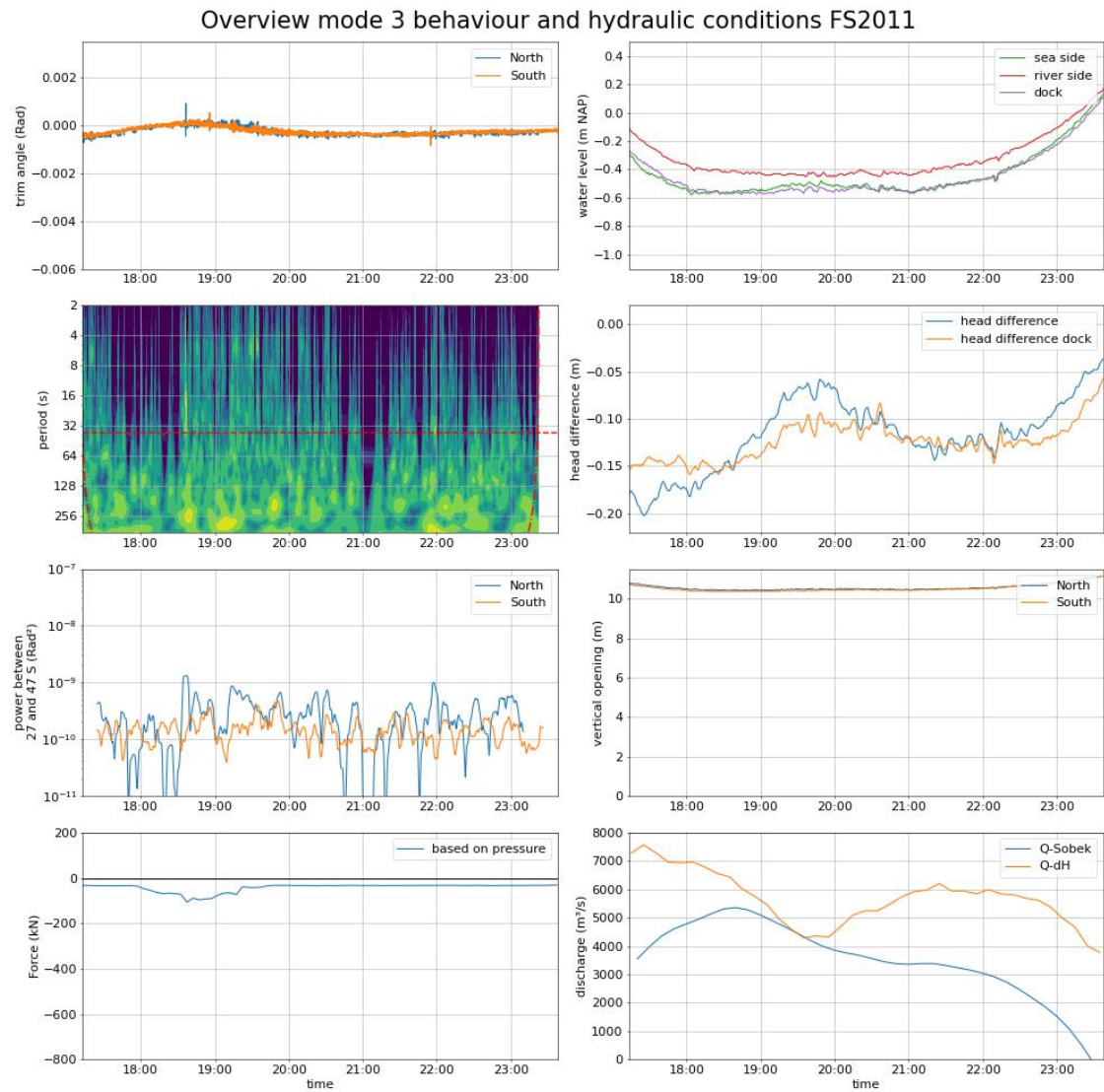


Figure D.5: Overview of mode 3 behaviour and flow conditions during the 2011 test closure

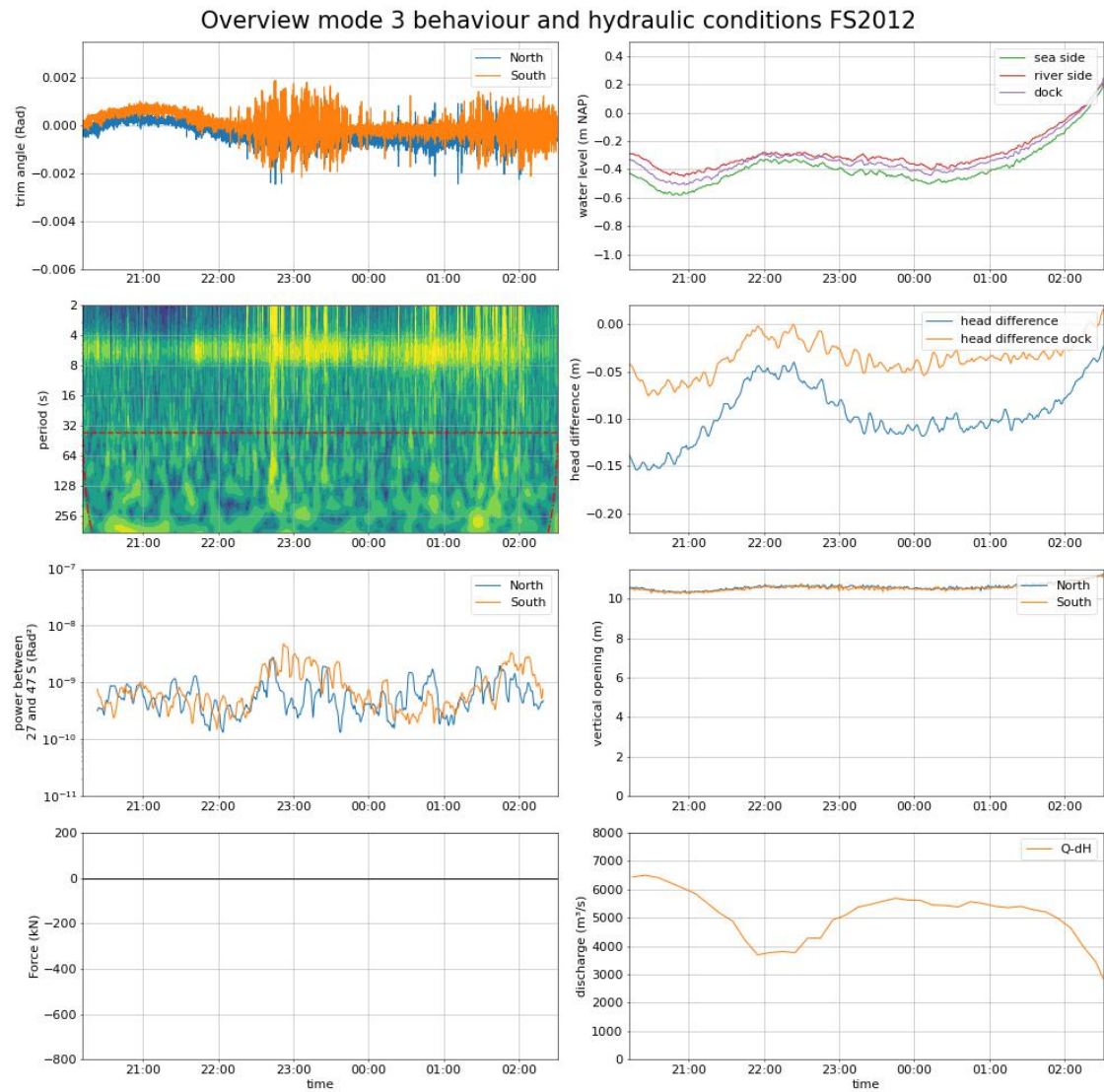


Figure D.6: Overview of mode 3 behaviour and flow conditions during the 2012 test closure

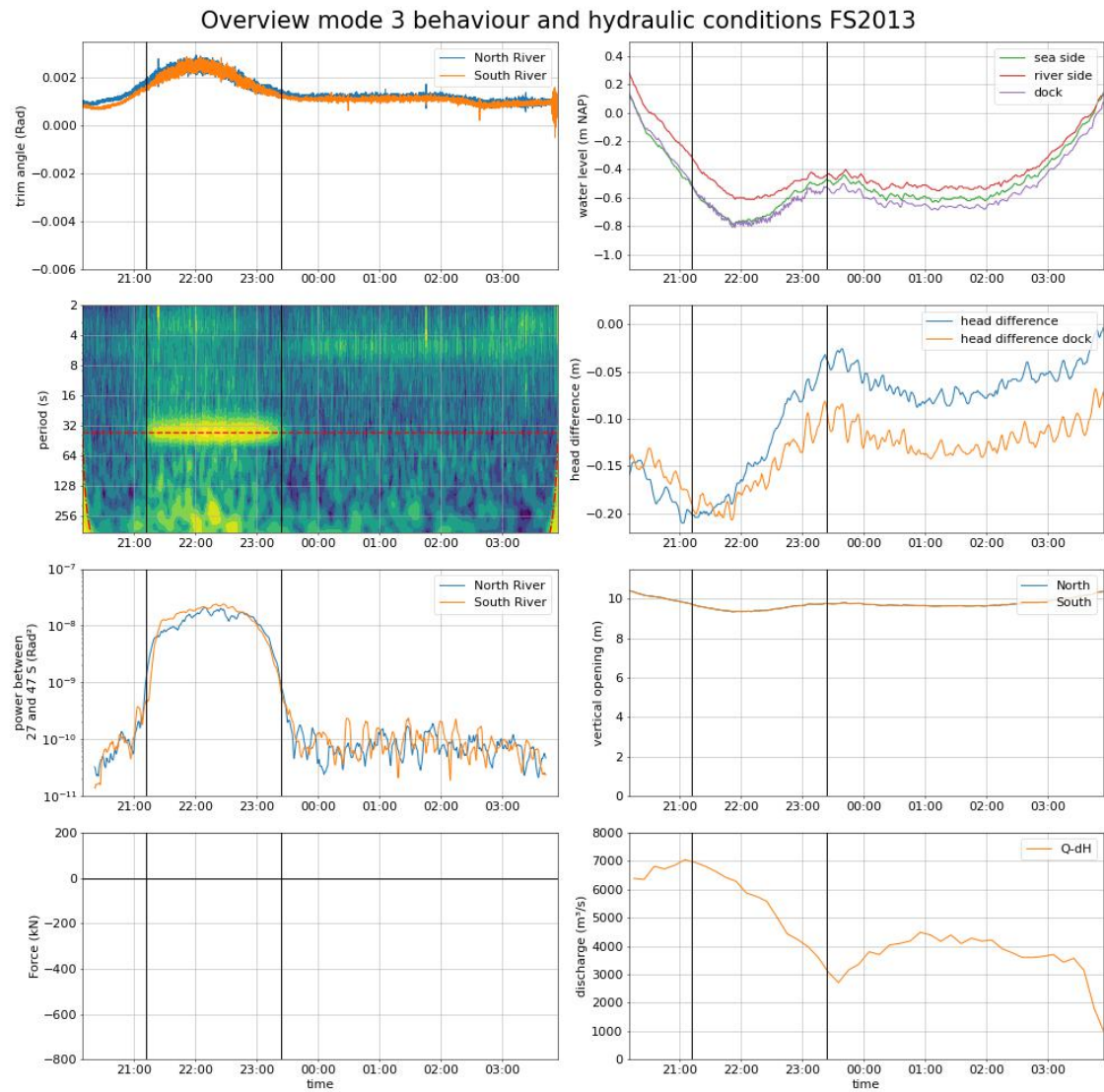


Figure D.7: Overview of mode 3 behaviour and flow conditions during the 2013 test closure

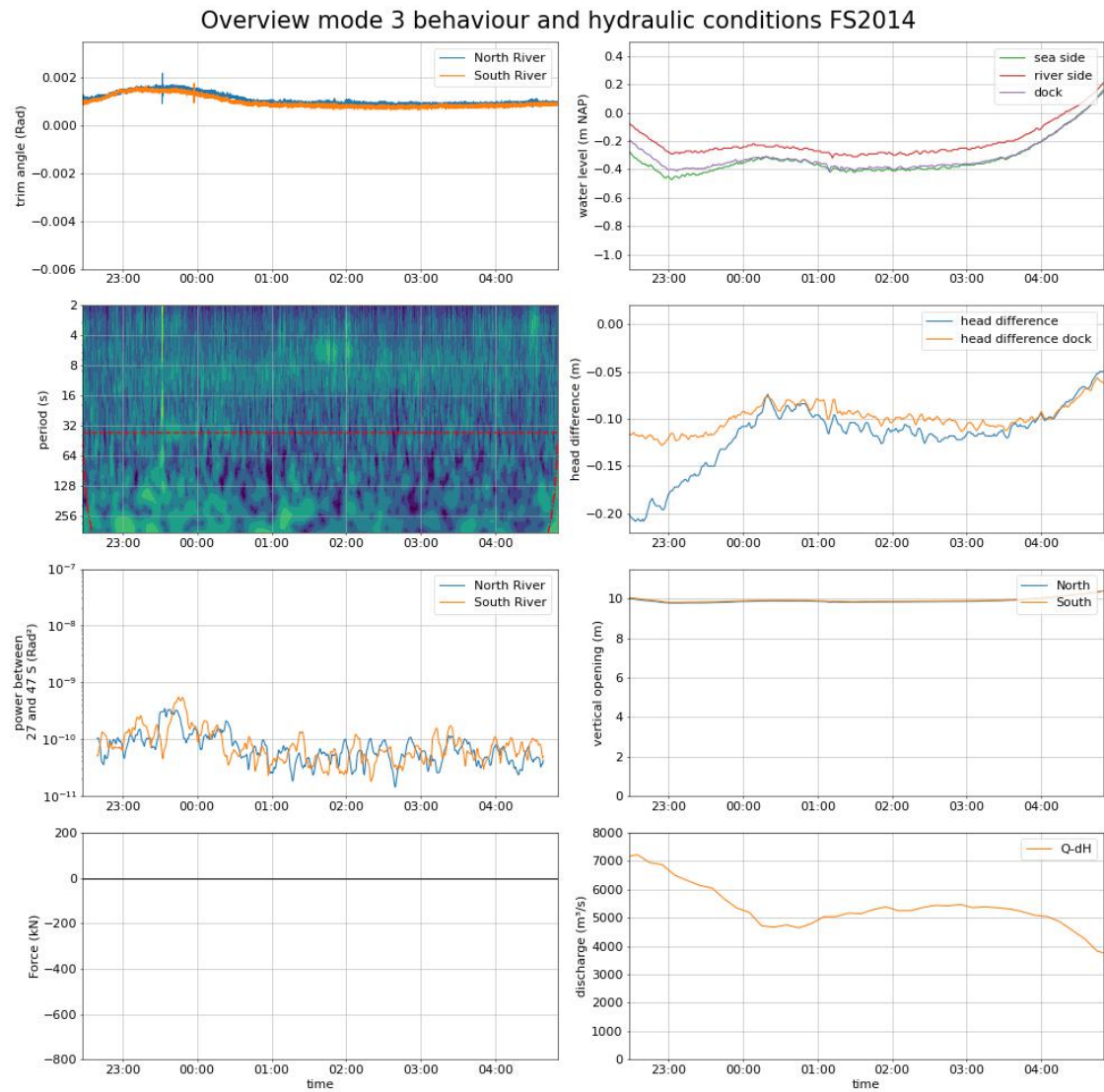


Figure D.8: Overview of mode 3 behaviour and flow conditions during the 2014 test closure

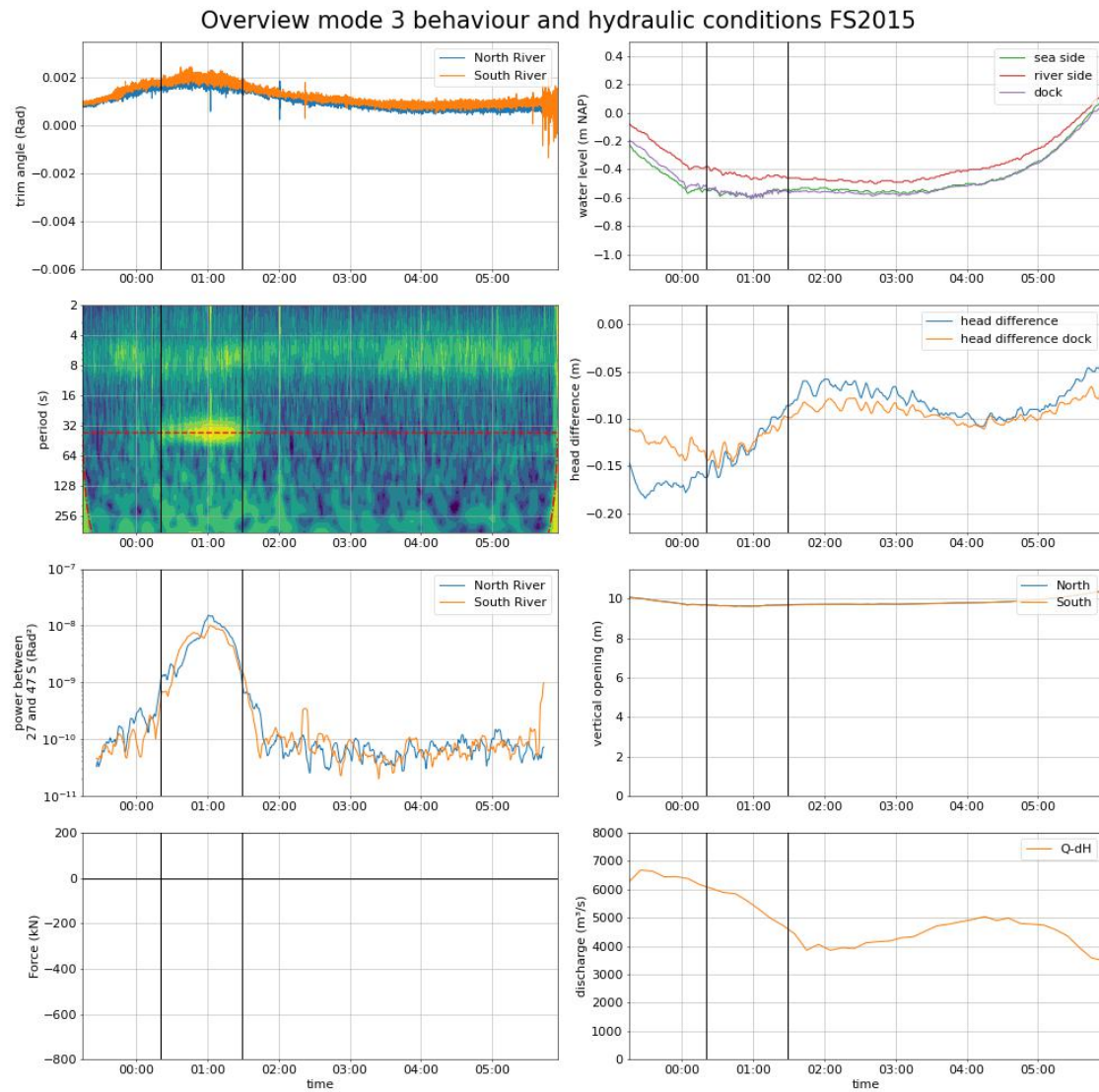


Figure D.9: Overview of mode 3 behaviour and flow conditions during the 2015 test closure

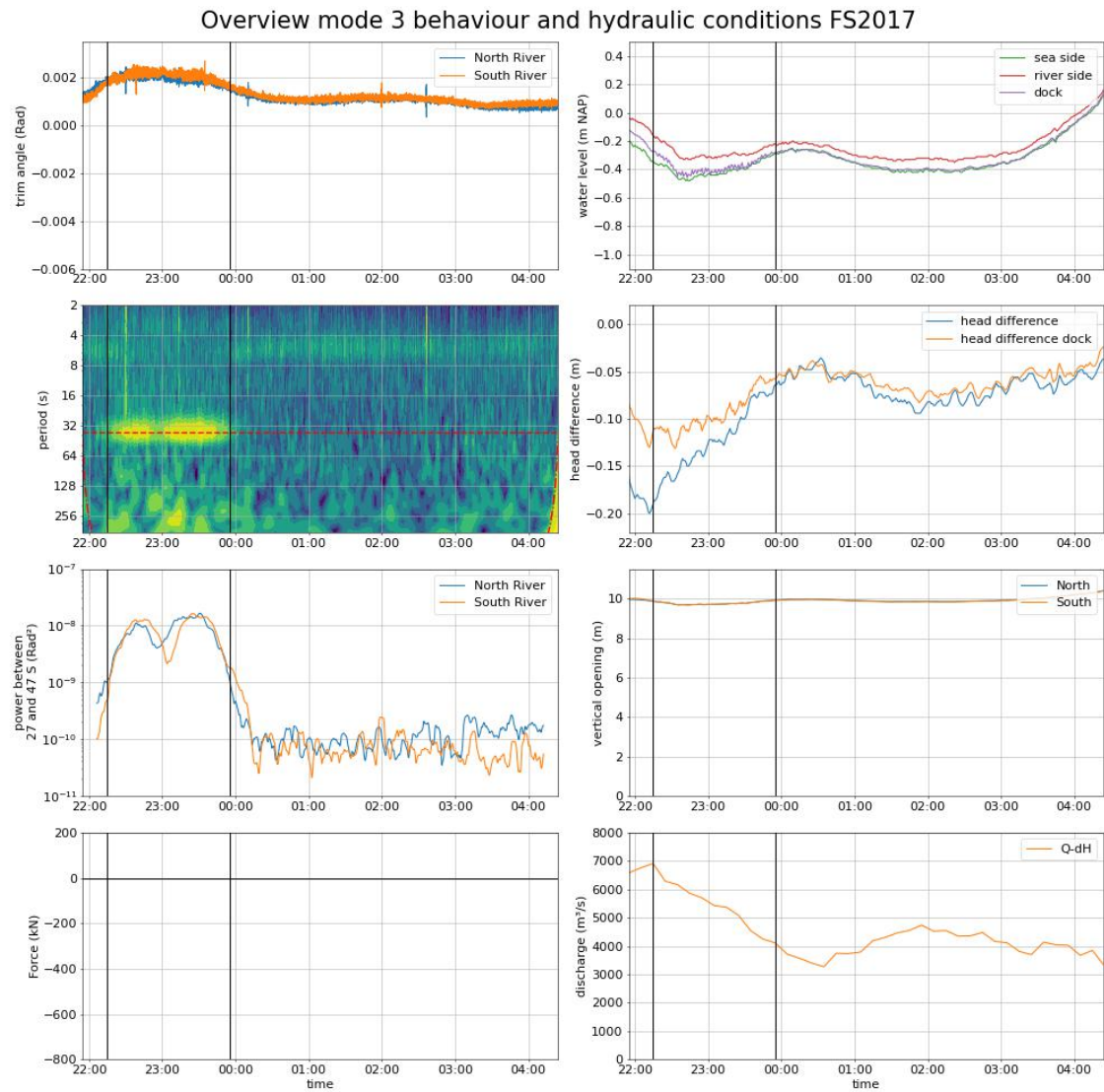


Figure D.10: Overview of mode 3 behaviour and flow conditions during the 2017 test closure

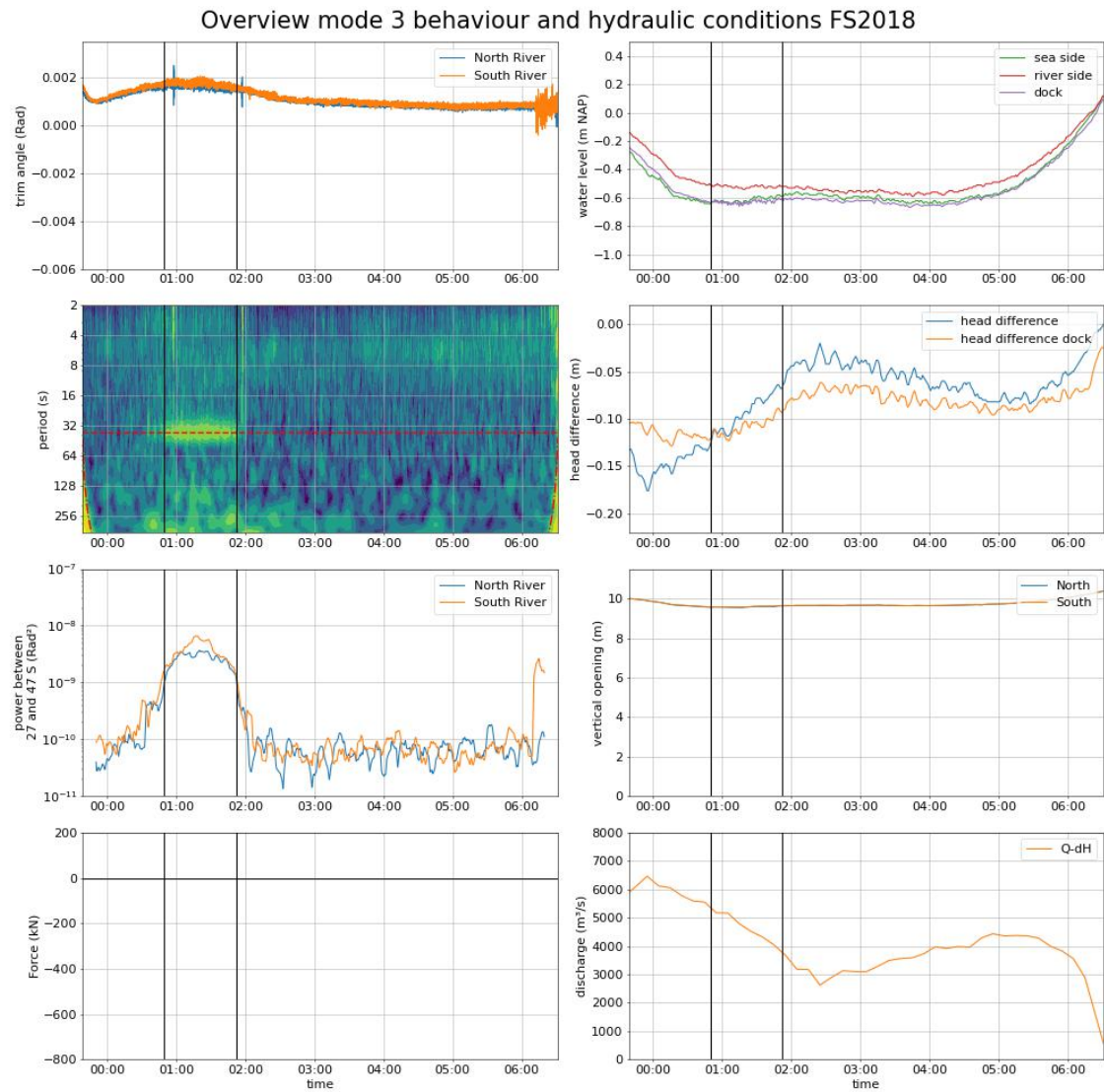


Figure D.11: Overview of mode 3 behaviour and flow conditions during the 2018 test closure

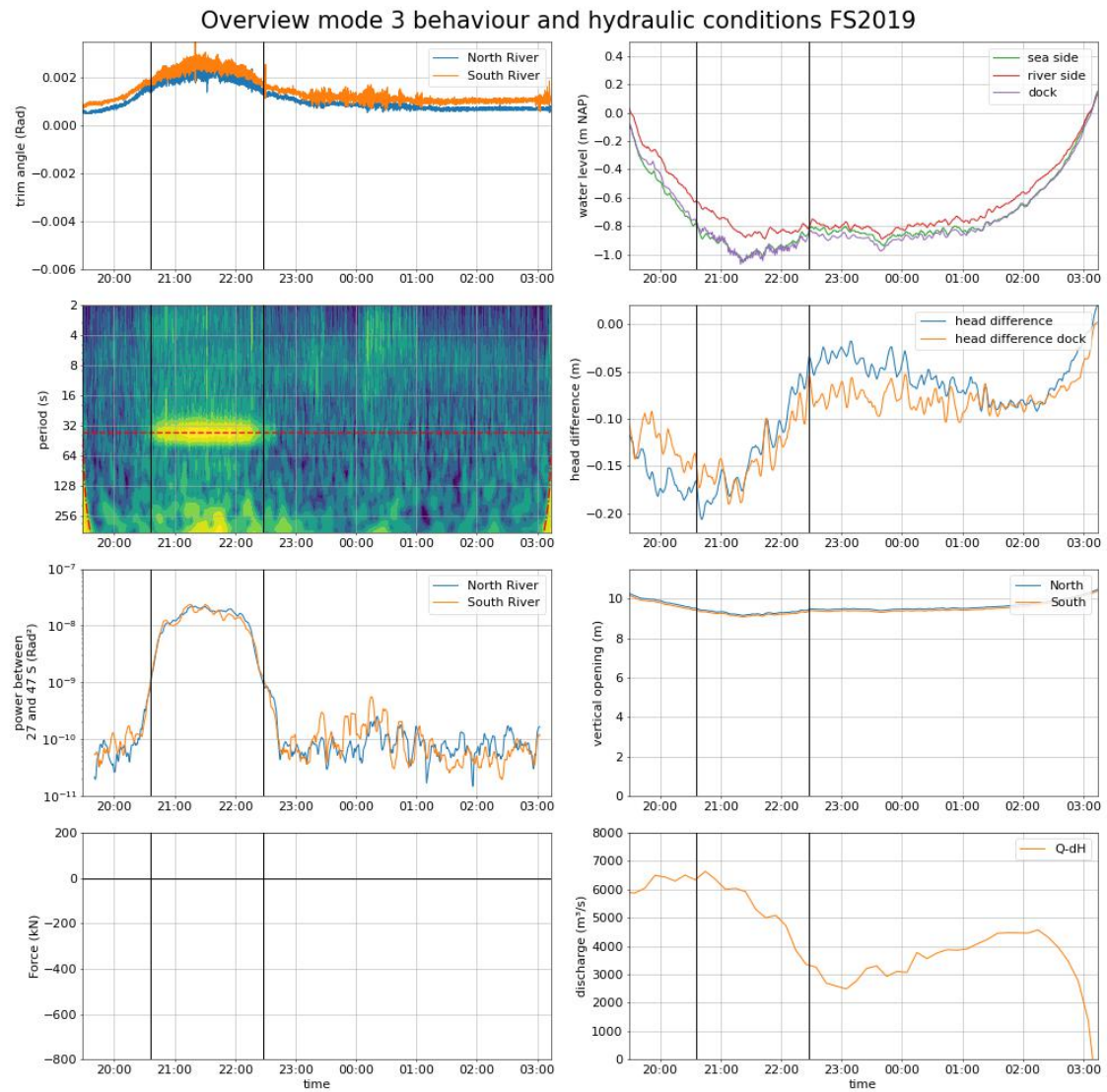


Figure D.12: Overview of mode 3 behaviour and flow conditions during the 2019 test closure

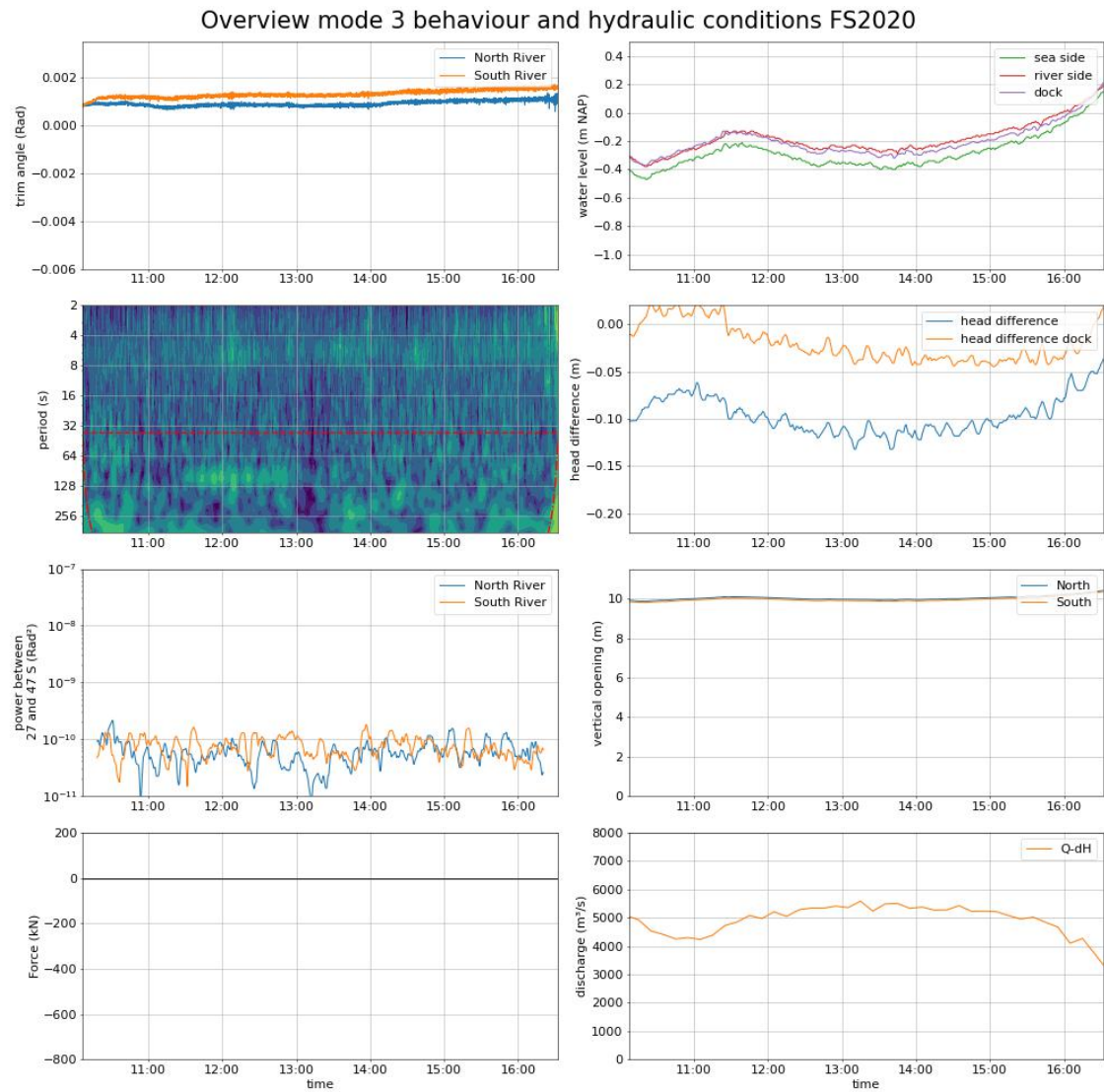


Figure D.13: Overview of mode 3 behaviour and flow conditions during the 2020 test closure

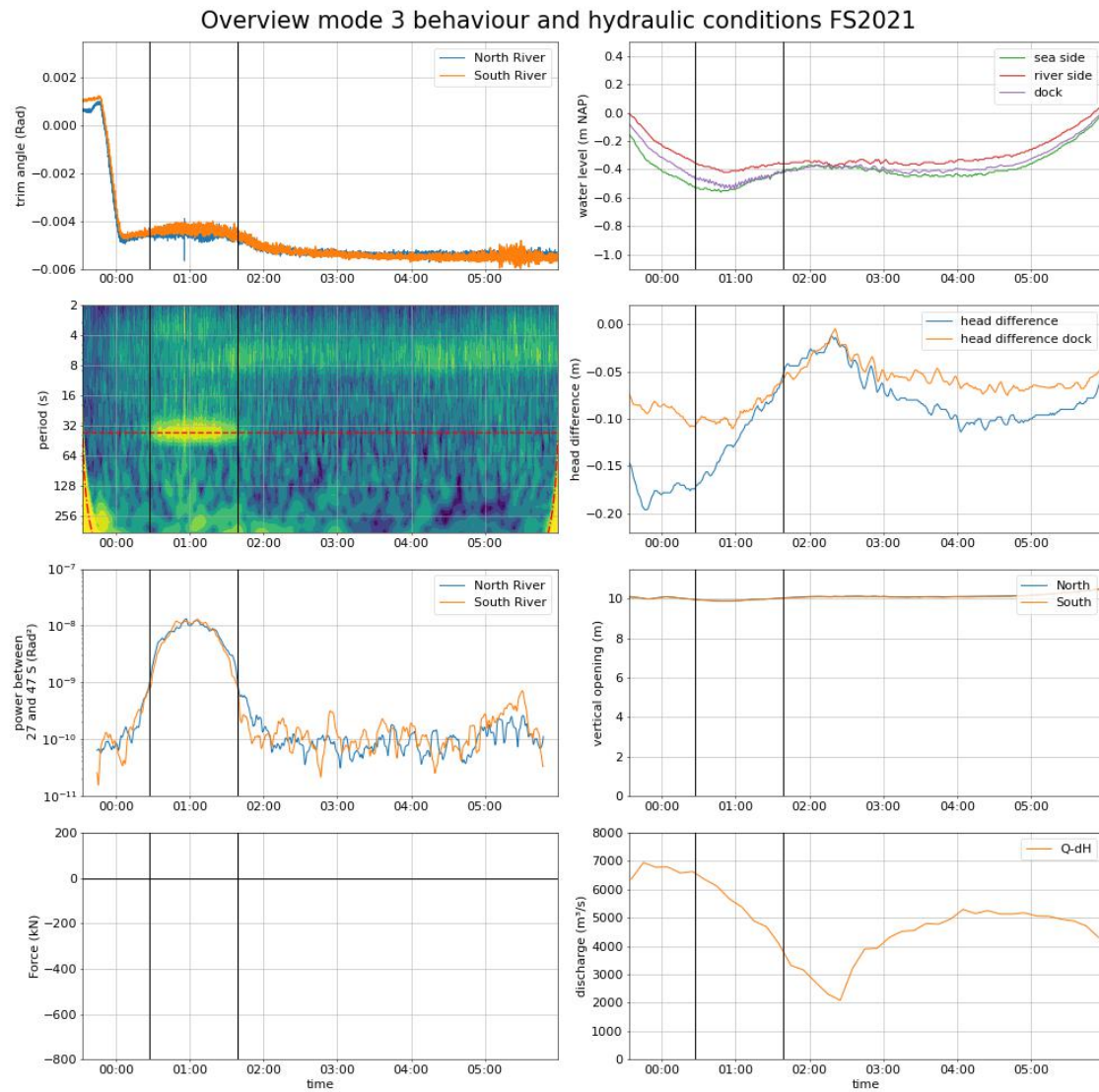


Figure D.14: Overview of mode 3 behaviour and flow conditions during the 2021 test closure



Correlation Matrix

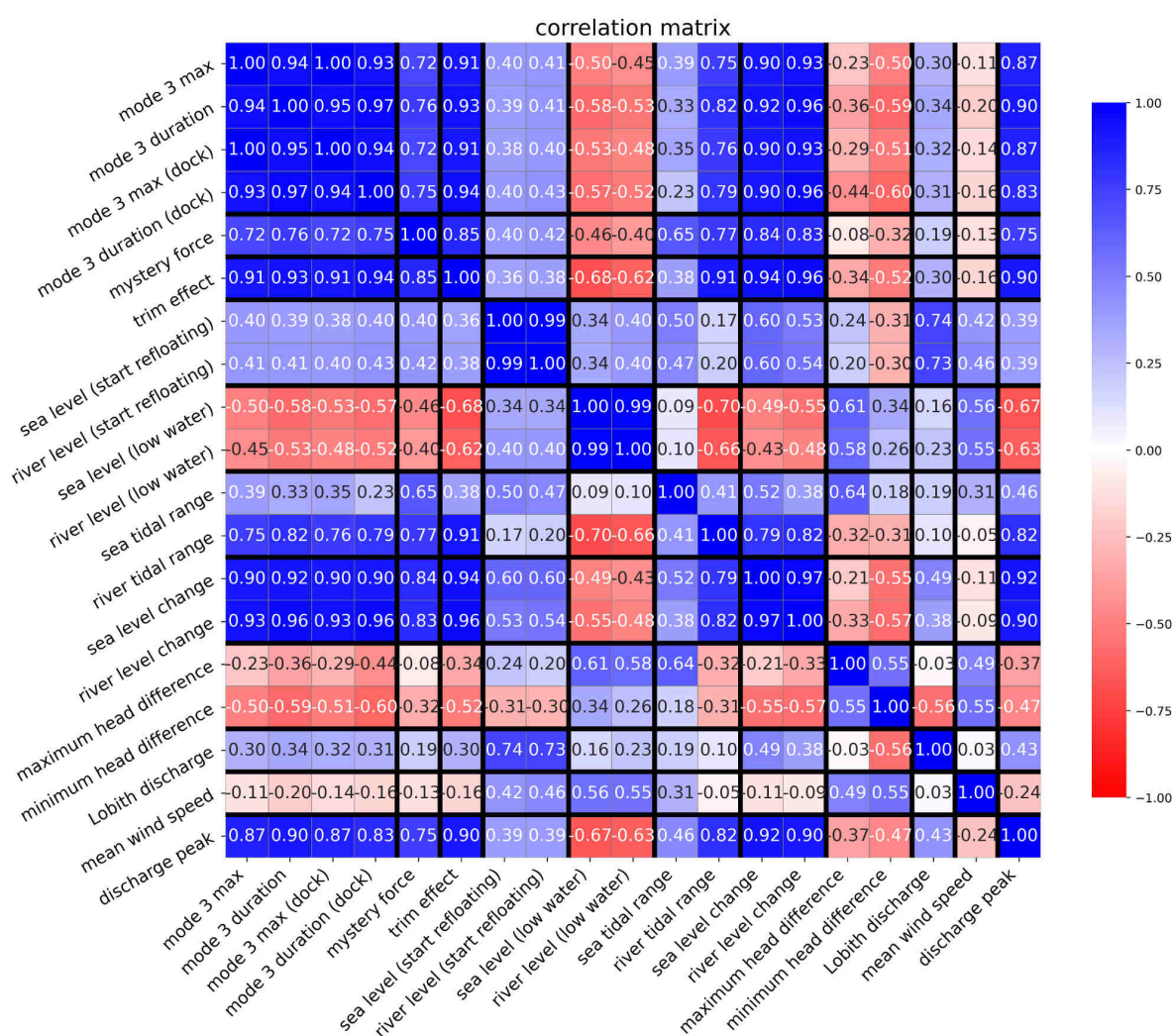


Figure E.1: Full correlation matrix



Empirical model parameters

F.1. Mystery Force

n	R^2	β_1	$\beta_{1,05}$	$\beta_{1,95}$
1	0.51	$6.9 \cdot 10^{-02}$	$1.6 \cdot 10^{-02}$	$1.2 \cdot 10^{-01}$
2	0.65	$1.1 \cdot 10^{-05}$	$6.6 \cdot 10^{-06}$	$1.6 \cdot 10^{-05}$
3	0.60	$1.7 \cdot 10^{-09}$	$1.2 \cdot 10^{-09}$	$2.2 \cdot 10^{-09}$

Table F.1: Fitted parameters empirical mystery force models without intercept

n	R^2	β_1	$\beta_{1,05}$	$\beta_{1,95}$	β_2
1	0.61	$1.2 \cdot 10^{-01}$	$6.3 \cdot 10^{-02}$	$1.7 \cdot 10^{-01}$	-285
2	0.65	$1.1 \cdot 10^{-05}$	$6.5 \cdot 10^{-06}$	$1.6 \cdot 10^{-05}$	3
3	0.68	$1.3 \cdot 10^{-09}$	$7.9 \cdot 10^{-10}$	$1.8 \cdot 10^{-09}$	109

Table F.2: Fitted parameters empirical mystery force models with intercept

F.2. Trim effect

n	R^2	β_1	$\beta_{1,05}$	$\beta_{1,95}$
1	0.61	$1.8 \cdot 10^{-04}$	$0.9 \cdot 10^{-04}$	$2.7 \cdot 10^{-04}$
2	0.82	$3.0 \cdot 10^{-08}$	$2.2 \cdot 10^{-08}$	$3.8 \cdot 10^{-08}$
3	0.77	$4.7 \cdot 10^{-12}$	$3.7 \cdot 10^{-12}$	$5.7 \cdot 10^{-12}$

Table F.3: Fitted parameters empirical trim effect models without intercept

n	R^2	β_1	$\beta_{1,05}$	$\beta_{1,95}$	β_2
1	0.83	$3.7 \cdot 10^{-04}$	$2.8 \cdot 10^{-04}$	$4.6 \cdot 10^{-04}$	-1.1
2	0.84	$3.4 \cdot 10^{-08}$	$2.6 \cdot 10^{-08}$	$4.2 \cdot 10^{-08}$	-0.2
3	0.81	$3.9 \cdot 10^{-12}$	$2.9 \cdot 10^{-12}$	$4.9 \cdot 10^{-12}$	0.2

Table F.4: Fitted parameters empirical trim effect models with intercept

F.3. Mode 3 effect

n	R^2	β_1	$\beta_{1,05}$	$\beta_{1,95}$
1	0.24	$2.0 \cdot 10^{-04}$	$-1.8 \cdot 10^{-04}$	$5.8 \cdot 10^{-04}$
2	0.42	$3.5 \cdot 10^{-08}$	$2.7 \cdot 10^{-09}$	$6.7 \cdot 10^{-08}$
3	0.55	$5.7 \cdot 10^{-12}$	$2.1 \cdot 10^{-12}$	$9.2 \cdot 10^{-12}$

Table F.5: Fitted parameters empirical mode 3 effect models without intercept

n	R^2	β_1	$\beta_{1,05}$	$\beta_{1,95}$	β_2
1	0.56	$8.0 \cdot 10^{-04}$	$4.2 \cdot 10^{-04}$	$1.2 \cdot 10^{-03}$	-3.6
2	0.63	$7.8 \cdot 10^{-08}$	$4.6 \cdot 10^{-08}$	$1.1 \cdot 10^{-07}$	-1.7
3	0.66	$9.2 \cdot 10^{-12}$	$5.7 \cdot 10^{-12}$	$1.3 \cdot 10^{-11}$	-0.9

Table F.6: Fitted parameters empirical mode 3 effect models with intercept

G

Mystery force inertia effects

In the tangential force balance, inertia effects may be expected. To consider the possible influence of inertial effects in the tangential force balance the gate is considered as a pendulum with two masses moving around the ball joint with the degree of freedom θ_{turn} , kept in place by a spring representing the pull/push rod, see Figure G.1. If the loading due to the mystery force effect happens slowly relative to the natural period of the system, these inertia effects can be neglected.

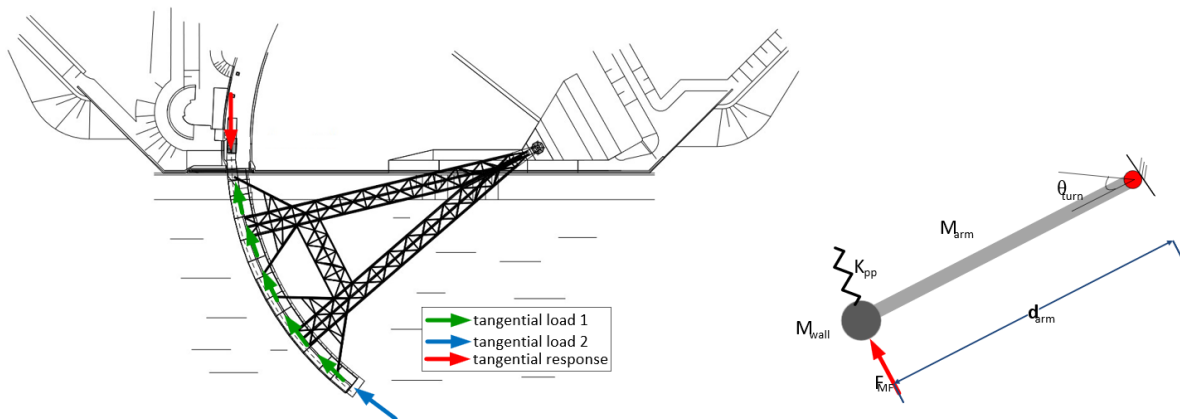


Figure G.1: Retaining wall modelled as pendulum Koninklijke PBNA, n.d.-a

The equation of motion belonging to the schematization in Figure G.1 is:

$$J\ddot{\theta}_{\text{turn}} + k_{\text{pp}}d_{\text{arm}}\theta_{\text{turn}} = d_{\text{arm}} \sum F_{r,i} \Rightarrow \frac{J}{d_{\text{arm}}}\ddot{\theta}_{\text{turn}} + k_{\text{pp}}\theta_{\text{turn}} = \sum F_{r,i} \quad (\text{G.1})$$

With parameters:

- $k_{\text{pp}} = 1.1 \cdot 10^8 \text{ N/m}$: spring stiffness of the pull/push rod (Koninklijke PBNA, n.d.-b)
- $d_{\text{arm}} = 240 \text{ m}$: distance from the retaining wall to the socket joint (Koninklijke PBNA, n.d.-c)
- $\sum F_{r,i} \text{ (N)}$: the net tangential load on the retaining wall

The inertia of the retaining wall is:

$$J = \frac{1}{3}M_{\text{arm}}d_{\text{arm}}^2 + M_{\text{wall}}d_{\text{arm}}^2 = \left(\frac{1}{3}M_{\text{arm}} + M_{\text{wall}}\right)d_{\text{arm}}^2 \quad (\text{G.2})$$

With:

- $M_{\text{arm}} = 6.0 \cdot 10^6$ kg: mass of the truss arm (Rijkswaterstaat, n.d.-a)
- $M_{\text{wall}} = 6.8 \cdot 10^6$ kg: mass of the retaining wall (Rijkswaterstaat, n.d.-a)

Damping is neglected, since only an indication of the natural period is desired. The effect of damping on the natural period is limited, as long as the damping is relatively small.

The resulting natural frequency and corresponding period are:

$$\omega = \sqrt{\frac{d_{\text{arm}} \cdot k_{pp}}{J}} = \sqrt{\frac{240 \cdot 1.1 \cdot 10^8}{\left(\frac{1}{3} \cdot 6.0 \cdot 10^6 + 6.8 \cdot 10^6\right) 240^2}} = 0.23 \text{ rad/s} \quad (\text{G.3})$$

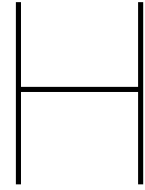
$$T = \frac{2\pi}{\omega} = 28 \text{ s}$$

The mystery force builds up over approximately one hour (see Appendix D), this is very slow compared to the found natural period of the system. Disregarding the inertia of the retaining wall therefore appears to be justified.

The fact that the retaining wall is partially submerged leads to added mass terms, however it can be seen that even an order of magnitude increase of the system inertia still results in low periods compared to the loading of the system:

$$\omega_1 = \sqrt{\frac{d_{\text{arm}} \cdot k_{pp}}{10 \cdot J}} = \sqrt{\frac{1}{10}} \omega \rightarrow T_1 = \sqrt{10} T = 87 \text{ s} \quad (\text{G.4})$$

The results from this analysis match with the observation in design documents that inertia effects play no big role regarding the horizontal loads on the movement mechanics (BMK, 1994).



Mystery force model definitions

H.1. Local head difference

The mystery force models rely on the head difference over the barrier. This local head difference is not a well established quantity, it has been estimated that with a contraction coefficient of 0.65 may be valid (Bakker, 2008).

The local head difference over the gate may be estimated from the discharge calculated by the numerical model and the vertical opening of the gate. Approximating the structure as a weir, it may be estimated from the following expression (Equation 2.1):

$$Q = \mu \cdot B \cdot d_0 \cdot \sqrt{2g\Delta h}$$

$$\Rightarrow \Delta h = \left(\frac{Q}{\mu \cdot B \cdot d_0} \right)^2 \cdot \frac{1}{2g} \quad (\text{H.1})$$

With:

- μ : assumed contraction coefficient of 0.65 (-)
- B : waterway width of 360 m
- d_0 : vertical flow gap under gate (m)
- g : gravitational constant 9.81 m/s²

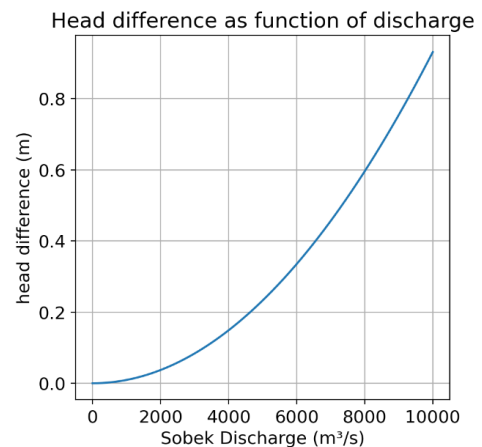


Figure H.1: Estimated head difference from local discharge

The contraction coefficient of 0.65 as appears in (Bakker, 2008) is also found in the properties of the discharge calculation model, the barrier width is taken directly from this model (Deltares, 2019). This width matches the width of the channel at the barrier, and not the total length of the rounded retaining walls, this parameter leaves room for interpretation. Assuming a constant vertical opening of 10 meters, leads to an estimated head difference as function of the discharge, as shown in Figure H.1.

H.2. (B1) Hydrostatic approach

This hypothesis implies a linear relationship between the local head difference and the force in the pull/push rod. The force on the push/pull rod caused by this load scales with the local head difference over the gate multiplied over the area of the short side of the retaining wall:

$$F = \rho g A_{\text{shortside}} \Delta h \quad (\text{H.2})$$

- ρ : water density 1012 kg/m³
- g : gravitational constant 9.81 m/s²
- $A_{\text{shortside}}$: retaining wall short side area earlier estimated at approximately 60 m² (Bakker, 2008)

- Δh local head difference (m)

It is analysed whether the assumption of the head difference acting over an area of 60 m² is a proper estimate. To this end, the cross-section of the retaining wall is divided into 3 areas, as shown in Figure H.2.

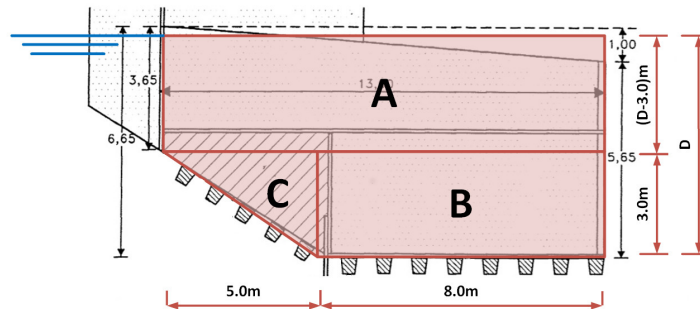


Figure H.2: schematization for determining hydrostatic load on short side, original cross-section in black from (WL|Delft Hydraulics, 1990b)

As can be seen in Figure H.2 part of the retaining wall is not accounted for by the marked areas (A, B, C), this is assumed to be the area on which the riverside water level cannot act, due to the presence of the labyrinth, which exists to close the horizontal opening between the north and south gate. This area is therefore disregarded when considering the load due to the head difference.

The total area and the hydrostatic load in Figure H.2 are a function of the draught of the retaining wall, D . Per segment, the area and hydrostatic load are given in Table H.1. The load is represented as the product of the segment surface area and the average hydrostatic pressure per segment.

	Surface Area	Total hydrostatic pressure
A	$(D - 3) \cdot 13 = (13D - 39)$	$\rho g \cdot (13D - 39) \cdot \frac{1}{2}(D - 3)$
B	$8 \cdot 3 = 24$	$\rho g \cdot 24 \cdot (D - 1.5)$
C	$\frac{1}{2} \cdot 5 \cdot 3 = 7.5$	$\rho g \cdot 7.5 \cdot (D - 1)$

Table H.1: short side hydrostatic area calculation

The hydrostatic pressure on the short sides of the retaining walls is determined for a draught, D . The draught at the dockside of the retaining wall can be given as D_0 , while in at the short side in the middle of the canal the local head difference is added: $D_0 + \Delta h$. Subtracting the load at the dockside from that in the middle of the river for each segment leads to the contribution to the tangential load given in Table H.2.

Note that a trim angle of the doors will also change the load on the short sides of the retaining walls, however this effect gives no net forcing as it gets compensated by opposite forces on the bottom of the retaining walls.

	Tangential load contribution
A	$\rho g \cdot [(13D - 39)\Delta h + 6.5\Delta h^2]$
B	$\rho g \cdot 24 \cdot \Delta h$
C	$\rho g \cdot 7.5 \cdot \Delta h$
Total	$\rho g \cdot [(13D - 7.5)\Delta h + 6.5\Delta h^2]$

Table H.2: short side hydrostatic load calculation

The total tangential load due to the head difference is the sum of a linear and quadratic term, of which only the linear term was present in the original estimate. From the linear term, the first estimate of the head difference times 60 m² is verified, by calculating the draught that would correspond to this estimate:

$$(13D - 7.5) = 60 \Rightarrow D = 5.2m \tag{H.3}$$

From the cross-section in Figure H.2 this seems very reasonable. However, from this model, it can also be seen that the tangential load due to this effect is also susceptible to a change in the overall draught. Uncertain is whether this draught varies between the different closures, changes in residual load in the retaining wall and flow conditions (through a suction force) may play a role. For now, the draught in this model is assumed constant at 5.2 meters, such that the estimate of 60 m² may be used.

To assess the effect of the second, quadratic term found in Table H.2, its size relative to the linear term is assessed:

$$\frac{6.5\Delta h^2}{60\Delta h} = 0.11\Delta h \tag{H.4}$$

Since the term is quadratic, its relative size scales with the head difference. For the considered range of head differences, the effect is small. For a head difference of 0.5 m the quadratic term increases the load by 5.5%, for a more extreme 1 m head difference the increase is 11%. Excluding this term won't have a big impact on the original estimation, however for completeness it is included in the model formulated in this section.

Under these assumptions, the contribution to the mystery force for this model is written as (with all terms as defined earlier):

$$F = \rho g \cdot [60\Delta h + 6.5\Delta h^2], \Delta h = \left(\frac{Q}{\mu \cdot B \cdot d_0}\right)^2 \cdot \frac{1}{2g} \tag{H.5}$$

To assess the magnitude of the mystery force associated with this mechanism, it is calculated for discharges ranging from 0 to 8,000 m³/s, assuming a constant vertical opening of 10 meters. The result is shown in Figure H.3.

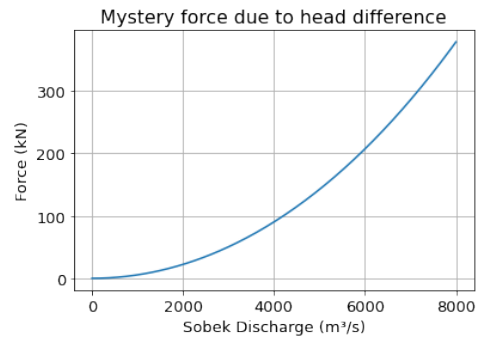


Figure H.3: Mystery force predicted based on head difference

H.3. (B2) Momentum balance approach

To construct a momentum balance the channel is schematized as rectangular, with a channel width, *B*, of 360 meters. The depth is assumed constant at the level of the sill, -17 m NAP. This schematization choice is illustrated with the bathymetry in Figure H.4. Away from the abutments of the barrier the channel widens, but in that widened area the depth is relatively shallow, and the flow is impeded by groins. Regarding the depth around the barrier, there are areas with a lower bed level, however these areas appear relatively small compared to the overall channel.

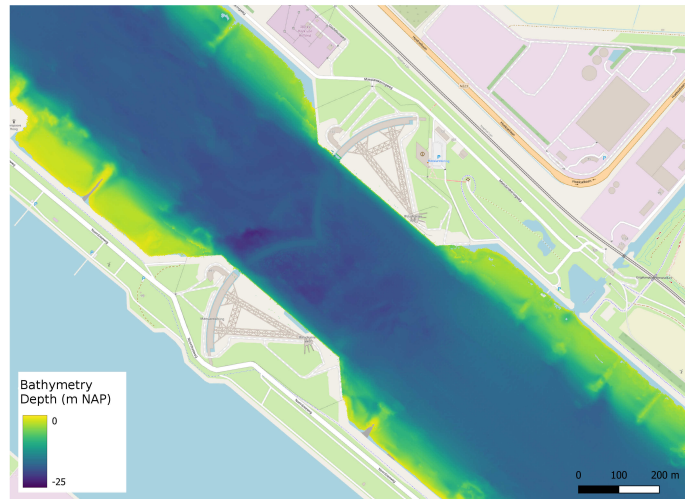


Figure H.4: Maeslant barrier bathymetry data from (Rijkswaterstaat, 2021), background map from (OpenStreetMap, 2022)

A longitudinal sketch of the considered control volume is shown in Figure H.5, with water levels and discharges presumed known in a cross-section upstream and downstream of the barrier (the borders of the control volume). The water levels are given in terms of the seaside water level and a local head difference. Assuming a stationary situation, the hydrostatic load on both sides of the control volume and the momentum flux may be used to determine the total load, F , on the gate (Elger et al., 2013).

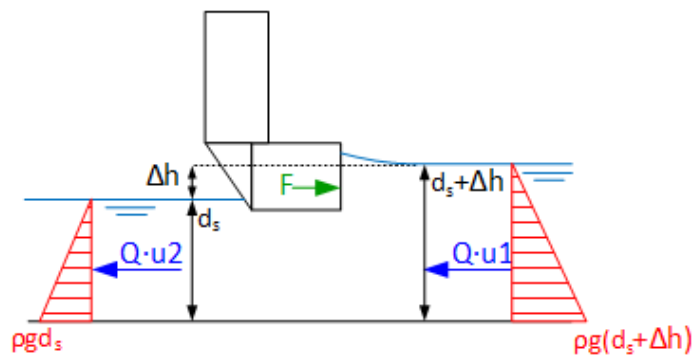


Figure H.5: Barrier momentum balance schematization, with hydrostatic loads in red, momentum associated with flow in blue and the force from the gate in green

A top view of the control volume is given in Figure H.6 where it can be seen that the derived load on the gate, F is a load parallel to the flow direction acting over the full length of the waterway

The total sum of forces acting parallel to the stream are equal to the change of momentum over the control volume, expressed with the change of flow velocity over the volume (in dark blue in Figure H.5):

$$\sum F_i = \rho Q(u_2 - u_1) \quad (H.6)$$

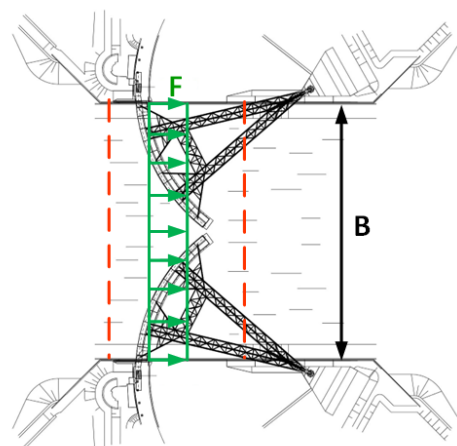


Figure H.6: Barrier momentum balance schematization top view, with location of boundaries in red, and the force on the barrier in green. Base image from Koninklijke PBNA, n.d.-a

With:

- $\sum F_i$: total force parallel to the flow on the control volume (N)
- ρ : water density 1012 kg/m³
- Q : discharge (m³/s)
- u_1, u_2 : flow velocity respectively up- and downstream of the retaining wall (m/s)

The forces acting on the control volume are the hydrostatic loads and the force from the retaining wall (in red and green in Figure H.5):

$$\begin{aligned} \frac{1}{2}\rho g B(d_s + \Delta h)^2 - \frac{1}{2}\rho g B d_s^2 - F &= \rho Q(u_2 - u_1) \\ \Rightarrow F &= \frac{1}{2}\rho g B(d_s + \Delta h)^2 - \frac{1}{2}\rho g B d_s^2 - \rho Q(u_2 - u_1) \end{aligned} \quad (\text{H.7})$$

With:

- g : gravitational constant 9.81 m/s²
- B : channel width 360 m
- d_s : seaside depth (m)
- Δh : local head difference (m)
- F : loading on retaining walls (N)

The average flow velocity has to be approximated from the discharge, the water level, and the waterway width:

$$u_i = \frac{Q}{B h_i} \quad (\text{H.8})$$

with:

- h_i : local depth (m)

Substitution for u_1 and u_2 yields:

$$F = \frac{1}{2}\rho g B(d_s + \Delta h)^2 - \frac{1}{2}\rho g B d_s^2 - \rho Q \left(\frac{Q}{B d_s} - \frac{Q}{B(d_s + \Delta h)} \right) \quad (\text{H.9})$$

Simplifying and rearranging the equation yields the equation for the total load on both retaining walls:

$$F = \frac{1}{2}\rho g B(\Delta h^2 + 2d_s \cdot \Delta h) - \rho Q^2 \left(\frac{\Delta h}{B \cdot d_s \cdot (d_s + \Delta h)} \right) \quad (\text{H.10})$$

Only part of this load acts as a tangential load on the retaining wall. It is assumed this tangential load can be found by taking part of the load that acts perpendicular on the short side of the retaining wall. From Figure H.2 the short sides are approximately 13 meters, when the gates are fully closed the short sides approximately make an angle of 40 degrees with the horizontal. This is illustrated in Figure H.7 and is determined from the geometry of the retaining wall.

The portion of the width of the waterway that one of the short sides of the retaining occupies is:

$$\cos(40^\circ) \cdot \frac{13}{B} = \cos(40^\circ) \cdot \frac{13}{360} \quad (\text{H.11})$$

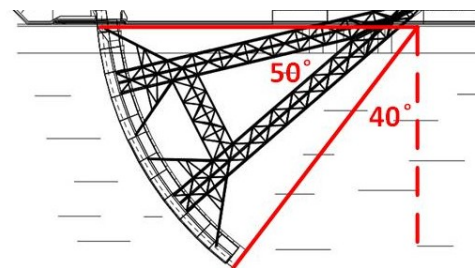


Figure H.7: Illustration of angle of short side relative to horizontal, not to scale. Base image from Koninklijke PBNA, n.d.-a

The force does not act perpendicular to the short side of the retaining wall, it is determined in the direction parallel to the channel direction (Figure H.6), to only consider the part of the load that acts perpendicular to the retaining wall a further correction of cosine 40 degrees is applied to find the contribution to the tangential load:

$$F_{mf} = \frac{\cos^2(40^\circ) \cdot 13}{360} \cdot F \approx 0.021F \quad (\text{H.12})$$

The expected tangential load is thus expected to be about 2% of the total loading on the gate, the remaining 98% of the load is assumed to be transferred to the ball joint as a radial load. By combining the equation for the force on the gate and the reduction factor based on the geometry of the structure, the modelled mystery force is written as:

$$F_{mf} = 0.021 \left[\frac{1}{2} \rho g B (\Delta h^2 + 2d_s \cdot \Delta h) - \rho Q^2 \left(\frac{\Delta h}{B \cdot d_s \cdot (d_s + \Delta h)} \right) \right], \Delta h = \left(\frac{Q}{\mu \cdot B \cdot d_o} \right)^2 \cdot \frac{1}{2g} \quad (\text{H.13})$$

With terms as defined in this subsection.

The equation for the force on the short side of the retaining wall can be filled in for the discharge range from 0 to 8,000 m³/s. The head difference is calculated using a vertical opening of 10 meters. The seaside water depth is, based on the bathymetry, assumed at 17 m. The resulting force is shown in Figure H.8, this force is higher than found for solely the head difference in Figure H.3.

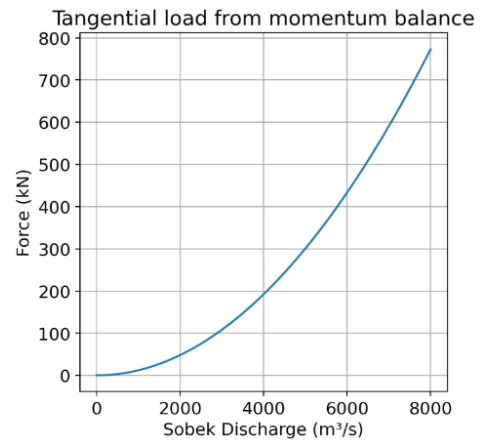


Figure H.8: Mystery force predicted based on head difference

H.4. (C1) Cross-sectional water level variation

For small trim angles, the force associated with this effect can be found by multiplying the weight of the retaining wall with the trim angle, using a small angle sine approximation:

$$F = -G \cdot \theta_{\text{eff}} \quad (\text{H.14})$$

In which θ_{eff} indicates part of the trim angle effect that is related to a water level variation, in radians. The weight of the retaining wall, G , including the truss arms, is approximately 126 MN (Rijkswaterstaat, n.d.-a).

To find the force the part of the trim angle related to a water level variation must be found, the trim angle may also be impacted by other effects, this does not lead to the effect described in this section.

The upper bound of the effect is the total trim effect from subsection 3.5.2, where the full trim effect is assumed to be due to a water level variation.

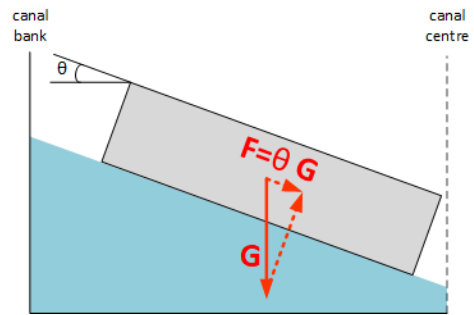


Figure H.9: Tangential force induced by water level variation

H.5. (C2) Suction force tangential contribution

The situation is again schematized as shown in Figure H.5. A formulation for the total head on the bottom of the retaining wall may be derived from applying Bernoulli's principle under the barrier and upstream of the barrier, and neglecting energy losses, which seems applicable because of the contracting flow:

$$\frac{u_0^2}{2g} + h + \Delta h = \frac{u^2}{2g} + h_{\text{barrier}} \quad (\text{H.15})$$

In which:

- u_0 : upstream flow velocity
- u : flow velocity under retaining wall
- $h_s + \Delta h$: upstream hydraulic head (free surface)
- h_{barrier} : barrier hydraulic head

the flow velocities can be expressed as function of the water levels and the local discharge:

$$u = \frac{Q}{\mu \cdot B \cdot d_0}, u_0 = \frac{Q}{B \cdot (h_s + \Delta h)} \quad (\text{H.16})$$

The head difference is earlier defined as:

$$\Delta h = \left(\frac{Q}{\mu \cdot B \cdot d_0} \right)^2 \cdot \frac{1}{2g} \quad (\text{H.17})$$

The energy balance can be rewritten to describe the hydraulic head under the barrier. As a first step, the head difference and velocity head under the barrier compensate each other, and are removed from the energy balance:

$$\frac{u_0^2}{2g} + h_s = h_{\text{barrier}} \quad (\text{H.18})$$

From this, the suction force is derived as the difference of the hydraulic head under the retaining wall h_{barrier} with the hydraulic head upstream of the retaining wall $h_s + \Delta h$:

$$h_{suction} = h_s + \Delta h - h_{barrier} = -\frac{u_0^2}{2g} + \Delta h \quad (\text{H.19})$$

This relation is not easily shown analytically, because of the structure of u_0 . Instead, $h_{suction}$ is determined as function of ΔH for a representative conditions:

- $d_0 = 10$ m
- $h_s = 17$ m
- $Q = 5000$ m³/s

With the other factors related to the barrier geometry as determined earlier, this gives:

$$h_{suction} \approx 0.85\Delta h \quad (\text{H.20})$$

The total suction force can be calculated from the head difference and the area on which it acts:

$$F_{suction} = \rho g \cdot A_{bottom} \cdot 0.85\Delta h \quad (\text{H.21})$$

With:

- $A_{bottom} = 13 \cdot 213 = 2763$ m²: bottom of retaining wall surface area (WL|Delft Hydraulics, 1990b)

To obtain the part of this force that can contribute to the mystery force, this force is multiplied with the peak trim angle, leading to the following model for this effect:

$$F = \theta_{peak} \cdot F_{suction} = \theta_{peak} \cdot \rho g \cdot A_{bottom} \cdot 0.85\Delta h \quad (\text{H.22})$$

Constant trim response model

I.1. Equation form

Using an analogy with a ship in pitch, the equation of motion for this system can be given. In the quasi-stationary approach, used for the constant trim angle effect, only the spring stiffness is considered, the system for the trim angle responses reduces to:

$$k_{hd}\theta = \sum M \quad (I.1)$$

To describe the trim angle effect θ the moment, M induced by the mystery force, and the spring stiffness k_{hd} are estimated in this appendix.

I.2. Spring stiffness

From this analogy, the restoring spring stiffness for the rotational degree of freedom is determined in the same way as for a pitching ship (Journée & Massie, 2001):

$$k_{hd} = \rho g \cdot \nabla \cdot \overline{GM} \quad (I.2)$$

With:

- $\rho = 1012 \text{ kg/m}^3$: water density
- $g = 9.81 \text{ m/s}^2$: gravitational constant
- $\nabla \text{ (m}^3\text{)}$: displaced water volume
- $\overline{GM} \text{ (m)}$: metacentric height

The displaced water volume, ∇ , can be estimated from the assumed geometry and draught to be (Appendix H, Figure 5.10):

$$\nabla = L \cdot b \cdot T = 180 \cdot 15 \cdot 5.2 = 14\,040 \text{ m}^3 \quad (I.3)$$

This estimation is checked against the known weight of the retaining wall and truss arms combined, by determining the mass of the displaced water:

$$\nabla \cdot \rho \cdot g = 14\,040 \cdot \text{m}^3 \cdot 1012 \text{ kg/m}^3 \cdot g = 142 \text{ MN} \quad (I.4)$$

The true displaced volume is unknown, but the estimated volume appears of a realistic magnitude. It is about 10% more than the combined mass of the retaining wall and arms, 126 MN (Rijkswaterstaat, n.d.-a). It's not unrealistic that is slightly higher, suction forces and residual water in the ballast tanks can increase the vertical load.

To calculate the spring stiffness of the retaining wall in pitch, its geometry must be considered to find the metacentric height, \overline{GM} . the metacentric height is the distance between the metacentre, M , and the centre of gravity, G , as indicated in Figure I.1 (Journée & Massie, 2001). For small angles, this value may be seen as a constant (Journée & Massie, 2001).

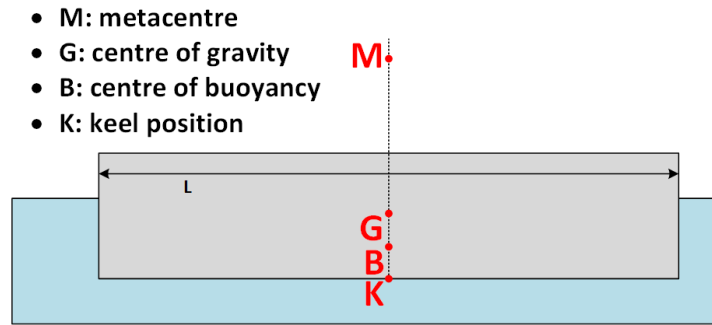


Figure I.1: Vertical positions used to determine \overline{GM}

\overline{GM} can be determined using the position of the centre of buoyancy relative to the keel position and the position of the metacentre relative to the centre of buoyancy (Journée & Massie, 2001):

$$\begin{aligned}\overline{GM} &= \overline{KB} + \overline{BM} - \overline{KG}, \\ \overline{BM} &= \frac{1}{12} \cdot b \cdot L^3 / \nabla\end{aligned}\quad (I.5)$$

It can be deduced that \overline{BM} is much greater for the considered case than \overline{KB} and \overline{KG} . since the centre of gravity and the centre of buoyancy can be expected to be within the retaining wall. \overline{BM} does not, which can be shown by completing the equation for \overline{BM} :

$$\overline{BM} = \frac{\frac{1}{12} \cdot b \cdot L^3}{\nabla} = \frac{\frac{1}{12} \cdot 15 \cdot 180^3}{14\,040} = 519 \text{ m} \quad (I.6)$$

Because of the magnitude of \overline{BM} compared to the expected magnitude of \overline{KB} and \overline{KG} , \overline{GM} is estimated based on only \overline{BM} :

$$\overline{GM} \approx 500 \text{ m} \quad (I.7)$$

The corresponding spring stiffness now follows from Equation I.2:

$$k_{nd} = \rho g \cdot \nabla \cdot \overline{GM} = 1012 \text{ kg/m}^3 \cdot 9.81 \text{ m/s}^2 \cdot 14\,040 \text{ m}^3 \cdot 500 \text{ m} = 7.0 \cdot 10^{10} \text{ Nm/rad} \quad (I.8)$$

I.3. Tangential force induced moment

The arm describing the moment due to the mystery force is derived based on the following assumptions:

1. The tangential force is parallel to the x -axis
2. Changes of θ do not influence the tangential force magnitude.

The first condition follows from the connection to the guiding tower, which does not allow the transfer of vertical forces. The second condition is assumed because the mystery force models do not include any effects due to a trim, θ .

The retaining wall is schematized in Figure I.2 indicating the position of the load and the response in the pull/push rod. The first order moment on the retaining wall is equal to the sum of the two arms d_1 , and d_2 , multiplied with the force F .

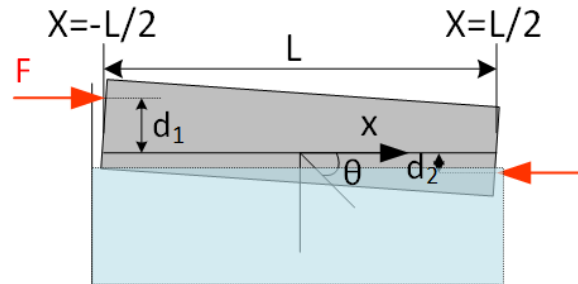


Figure I.2: Moment contribution due to load F

The force from the pull-push rod is assumed to act on top of the retaining wall. The vertical location of the tangential load at the riverside is determined from the hydrostatic pressure distribution on the short side of the retaining wall. From the triangular pressure distribution, the resulting force is assumed to act one third of the draught from the bottom of the retaining wall. The assumed draught of 5.2 m (Appendix H), is used for the calculation:

$$\frac{1}{3} \cdot 5.2 \text{ m} = 1.7 \text{ m} \quad (I.9)$$

From the total retaining wall height, approximately 22 m (Rijkswaterstaat, n.d.-a), the arm, e , becomes:

$$e = d_1 + d_2 = 22 \text{ m} - 1.7 \text{ m} \approx 20 \text{ m} \quad (I.10)$$

A second order moment of $180 \cdot \theta \cdot F$, may be expected (an increasing arm due to θ , Figure I.2), but for small angles this is small compared to the first order moment. This is illustrated for a mystery force of 400 kN and a trim effect of 1.5 milliradians (similar to the values found in Appendix C):

$$\begin{aligned} M_{\text{first order}} &= e \cdot F = 20 \cdot 400 = 8000 \text{ kNm} \\ M_{\text{second order}} &= 180 \cdot 1.5 \cdot 10^{-3} \cdot 400 = 108 \text{ kNm} \approx 0.01 \cdot M_{\text{first order}} \end{aligned} \quad (I.11)$$



Mode 3 model

The inertia and damping terms in this governing equation are considered in this appendix:

- $J + J_{hd}$: inertia term
- c_{hd} : damping term

J.1. Retaining wall inertia

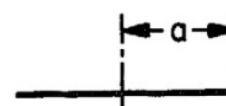
The moment of inertia of the retaining wall itself, J , is estimated from the geometry of the retaining wall and its known mass, $1.28 \cdot 10^7$ kg (Rijkswaterstaat, n.d.-a). The calculation is done by taking the retaining wall as a one-dimensional bar with its mass evenly distributed:

$$J = \frac{1}{12} \cdot M \cdot L^2 = \frac{1}{12} \cdot 1.28 \cdot 10^7 \cdot 180^2 = 3.5 \cdot 10^{10} \text{ kg} \cdot \text{m}^2 \quad (\text{J.1})$$

J.2. Retaining wall added mass

The hydrodynamic components of the inertia and of the damping terms of the Maeslant barrier are unknown. For this reason, an estimation needs to be made. Because finding a system that gives the exact response of the Maeslant barrier is not part of this model, merely explaining the type of motion is the goal, only some indications for these parameters is given.

The added mass is computed by assuming the retaining wall can be modelled as a 1D-plate, the added mass components for that schematization is given as m_{66} in Figure J.1 (Newman, 2018), which below is given multiplied with the retaining wall breadth:



m_{11} :	0
m_{22} :	$\pi \rho a^2$
m_{66} :	$\frac{1}{8} \pi \rho a^4$

$$J_{hd} = \frac{1}{8} \cdot \pi \cdot \rho \cdot (L/2)^4 \cdot b = \frac{1}{8} \cdot \pi \cdot 1012 \cdot 90^4 \cdot 15 = 3.9 \cdot 10^{11} \text{ kg} \cdot \text{m}^2 \quad (\text{J.2})$$

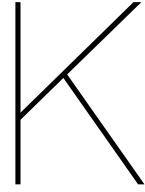
Figure J.1: 1D plate added mass components, image from Newman, 2018

J.3. Retaining wall damping

The damping is uncertain, for barges and container ships in rolling motion damping ratios in the order of magnitude of 5% are found (Chakrabarti, 2001). This 5% value will be used as estimate in this report:

$$\begin{aligned} \zeta = 0.05 &\Rightarrow c = \zeta \cdot 2 \cdot \sqrt{k_{est} \cdot (J + J_{hd})} \\ &\Rightarrow 0.1 \cdot \sqrt{7.25 \cdot 10^9 \cdot (3.5 \cdot 10^{10} + 3.9 \cdot 10^{11})} = 5.6 \cdot 10^9 \text{ kg} \cdot \text{m}/(\text{s} \cdot \text{rad}) \end{aligned} \quad (\text{J.3})$$

This can only be seen as a rough estimate, some tests from the physical model test suggest higher damping ratios ($\approx 10\text{-}20\%$ (WL|Delft Hydraulics, 1990b), but their applicability to the high-floating situation is unclear)



Mode 3 model solution

To assess the properties of the mode 3 system a solution form is assumed of which the parameters are numerically calculated, the solution form is presented in Equation 6.10, and repeated below:

$$\begin{bmatrix} \theta(t) \\ h_1(t) \end{bmatrix} = \begin{bmatrix} 1 \\ r \end{bmatrix} \cdot \begin{bmatrix} \exp([\alpha + i\omega]t) \\ \exp([\alpha + i\omega]t + i\phi) \end{bmatrix} \quad (\text{K.1})$$

With:

- ω (rad/s): angular frequency
- $[1, r]$: Eigenvector describing magnitude of h_1 (meters) relative to θ (rad)
- α (-): exponential growth factor
- ϕ (rad): phase shift between of h_1 relative to θ

For a chosen solution form to satisfy a homogeneous system, substitution of the general solution into the governing differential equations should yield a system that is solvable. To support the chosen solution, its substitution in the following system is considered (which is a simplified system compared to the derived mode 3 system, without diagonal terms in the mass and damping matrix):

$$\begin{bmatrix} M_{11} & 0 \\ 0 & M_{22} \end{bmatrix} \begin{bmatrix} \ddot{x}_1 \\ \ddot{x}_2 \end{bmatrix} + \begin{bmatrix} C_{11} & 0 \\ 0 & C_{22} \end{bmatrix} \begin{bmatrix} \dot{x}_1 \\ \dot{x}_2 \end{bmatrix} + \begin{bmatrix} K_{11} & K_{12} \\ K_{22} & K_{22} \end{bmatrix} \begin{bmatrix} x_1 \\ x_2 \end{bmatrix} = \begin{bmatrix} 0 \\ 0 \end{bmatrix} \quad (\text{K.2})$$

The full mode 3 system follows the same reasoning as presented below, but for clarity the simplified system is considered. Substitution of the solution form, Equation K.1, yields the following system of two equations:

$$\begin{cases} K_{21}re^{i\phi} + M_{11}\alpha^2 + (2iM_{11}\omega + C_{11})\alpha + iC_{11}\omega - M_{11}\omega^2 + K_{11} = 0 \\ (M_{22}\alpha^2 + (2iM_{22}\omega + C_{22})\alpha + iC_{22}\omega - M_{22}\omega^2 + K_{22})re^{i\phi} + K_{21} = 0 \end{cases} \quad (\text{K.3})$$

It can be seen that both equations have real and imaginary terms, both of which need to equal 0 for the chosen solution to be applicable. An assumed solution without phase shift ($\phi = 0$) yields the following imaginary terms of the two equations (since: $\phi = 0 \Rightarrow \exp(i\phi) = 1$):

$$\begin{cases} 2M_{11}\alpha + C_{11} = 0 \\ 2M_{22}\alpha + C_{22} = 0 \end{cases} \quad (\text{K.4})$$

These equations are only applicable in the specific case where: $C_{11}/M_{11} = C_{22}/M_{22}$. Thus, a general solution where $\phi = 0$ does not exist for the damped system except for very specific system configurations, a phase shift may thus be expected in the general solution.

The system that can numerically be solved to find the properties of the solutions to the system is found by separating the real and imaginary terms in Equation K.3. In order to do this, Euler's formula is applied on the exponent of the phase shift:

$$e^{i\phi} = \cos(\phi) + i \sin(\phi) \quad (\text{K.5})$$

This yields the following set of four equations:

$$\left\{ \begin{array}{l} K_{21} r \cos(\phi) + M_{11} \alpha^2 + C_{11} \alpha - M_{11} \omega^2 + K_{11} = 0 \\ K_{21} r \sin(\phi) + 2M_{11} \alpha \omega + C_{11} \omega = 0 \\ (M_{22} \alpha^2 - M_{22} \omega^2 + C_{22} \alpha + K_{22}) r \cos(\phi) - (2M_{22} \alpha \omega + C_{22} \omega) r \sin(\phi) + K_{21} = 0 \\ (2M_{22} \alpha \omega + C_{22} \omega) r \cos(\phi) + (M_{22} \alpha^2 - M_{22} \omega^2 + C_{22} \alpha + K_{22}) r \sin(\phi) = 0 \end{array} \right. \quad (\text{K.6})$$

This set of four equations, with four unknowns, is a system that can numerically solved. The system solved for the mode 3 system is of a similar shape, but with extra terms due to the diagonal entries in the matrices.



Jackknife resample

The considered mystery force models are re-estimated, but now using a Jackknife approach, to give a second estimate of the parameters and their uncertainty. A description of the jackknife resampling method is given in subsection 6.3.4. The results are compared to the earlier results, which are referred to as the simple regression solution, because they are based on only the least squares solution to the full dataset.

Q² empirical model

The discharge squared model has the form (Table 4.1):

$$F = \beta_1 \cdot Q^2 \tag{L.1}$$

In which β_1 is a fitted slope parameter.

The resulting fits using the jackknife approach for this empirical model are shown in Figure L.1a, superimposed on the previous results. All fits are within the 90% interval from the original simple regression approach. The 95% upper bound as follows from Equation 6.13 is also given in Figure L.1a.

This similarity with the simple regression is reflected in the distribution of the fitted parameter a , shown in Figure L.1b (based on the relevant t -distribution and the standard error). It can be seen that the estimated parameter, a , for the jackknife resample is very similar to the result from the simple regression. It can be seen that the jackknife resample gives a slightly wider distribution for the parameter a .

The 95% upper bound for the jackknife estimate is 12% above the original 95% upper bound.

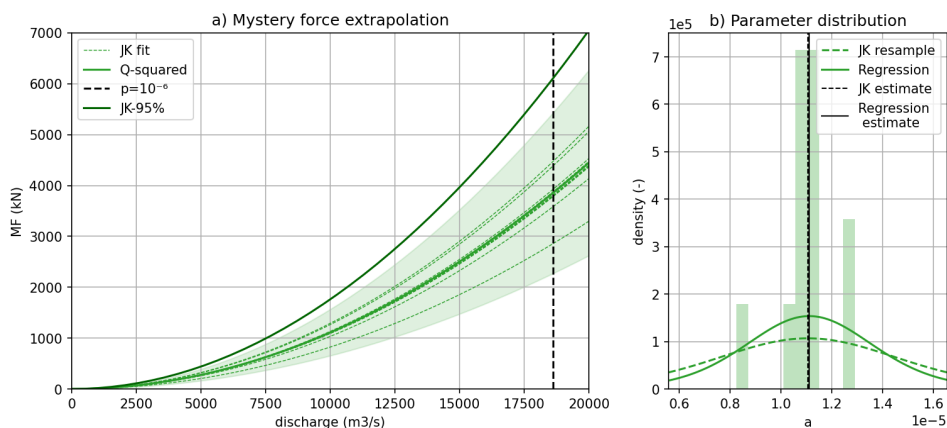


Figure L.1: a) Jackknife estimates compared to simple regression model b) comparison of slope parameter distribution from simple regression and jackknife resample

momentum balance model

The jackknife resample is applied to the momentum balance (summarized in Table 5.1). As a fitted parameter, the discharge coefficient μ is considered, as in Table 6.1.

The results of the fits in are presented in Figure L.2a for the scenario with the water level at +0 m NAP. The differences between the fits are smaller than for the empirical model resample.

From Figure L.2b it follows that both approaches yield similar values for μ . The distribution for μ that follows the jackknife resample is almost identical, this possibly indicates that the confidence interval resulting from the curve fit has also been determined with the jackknife resample, or a similar bootstrapping approach.

Based on this, the 95% upper bound from the jackknife resample is not considered separately in Figure L.2a. The used resampling technique does not impact the mystery force that follows from the momentum balance model.

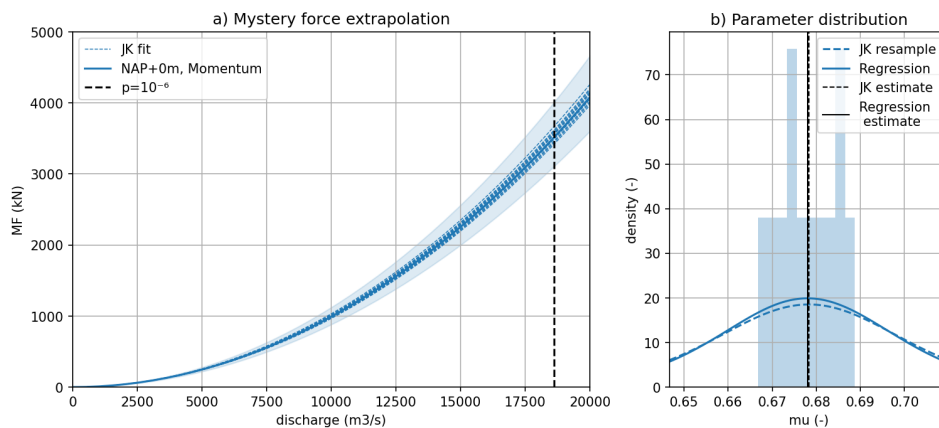


Figure L.2: a) Jackknife estimates compared to simple regression model b) comparison of slope parameter distribution from simple regression and jackknife resample